

ABSTRACT

Title of dissertation: ANALYTICAL MICROSCOPY APPLICATIONS TO
WIDE-BANDGAP SEMICONDUCTORS AND
NANOCARBON-METAL COMPOSITE MATERIALS

Christopher J. Klingshirn
Doctor of Philosophy, 2020

Dissertation directed by: Professor Lourdes Salamanca-Riba
Department of Materials Science and Engineering

Understanding the atomic structure of materials lies at the heart of materials science. Electron microscopy offers myriad techniques to both probe processing-structure-property relationships in materials, and to manipulate those relationships directly. In this thesis, analytical transmission electron microscopy (TEM) was used to investigate two distinct material systems with applications to energy-efficient technologies: wide-bandgap semiconductors and nanocarbon-metal composites.

In the first project, TEM and electron energy loss spectroscopy were used to investigate the structure, composition and bonding of metal-oxide-semiconductor devices based on silicon carbide (SiC) and gallium oxide (Ga_2O_3). The performance of SiC falls short of ideal due to electrically active interfacial defect states. This work confirms that boron doping at the SiC/SiO₂ interface is feasible and improves the device channel mobility likely through a stress-relaxation mechanism. Separately, no adverse structural effects were found after antimony ion implantation into the SiC substrate, which independently raises mobility via a counter-doping mechanism.

Few atomic-scale studies on Ga_2O_3 have been reported to date; this thesis aims to bridge the knowledge gap by investigating gate oxide materials and process conditions from a structural perspective. Elevated annealing temperatures reduced interface quality for both SiO_2 and Al_2O_3 gate oxides. Separately, amorphous Al_2O_3 layers were crystallized under moderate electron irradiation in TEM. One-fourth the dose was required for crystallization with 100-keV electrons compared to 200 keV, indicating an ionization-induced atomic rearrangement mechanism. This unexpected phenomenon will have implications for devices operating in extreme environments.

The second project investigated structure-property relationships in novel nano-carbon metal-matrix composites called covetics, which exploit the superior mechanical and electrical properties of carbon nanostructures such as graphene. Aluminum covetics were characterized using TEM and various spectroscopy techniques; complementary quantum-mechanical and effective-medium models were used to predict the performance of covetics with a range of structures. The models suggest that an electrical conductivity enhancement of $\approx 10\%$ is feasible with a 5 vol.% carbon loading, but oxides and poor Al/C contact often diminish the performance of real covetics.

ANALYTICAL MICROSCOPY APPLICATIONS TO
WIDE-BANDGAP SEMICONDUCTORS AND
NANOCARBON-METAL COMPOSITE MATERIALS

by

Christopher J. Klingshirn

Dissertation submitted to the Faculty of the Graduate School of the
University of Maryland, College Park in partial fulfillment
of the requirements for the degree of
Doctor of Philosophy
2020

Advisory Committee:

Professor Lourdes G. Salamanca-Riba, *Chair/Advisor*

Professor John Cumings

Professor Neil Goldsman, *Dean's Representative*

Professor Manfred Wuttig

Dr. Tsvetanka S. Zheleva

© Copyright by
Christopher J. Klingshirn
2020

Acknowledgments

I am grateful to everyone who has made this work possible.

First I would like to thank my advisor, Professor Lourdes Salamanca-Riba, for the opportunity to work and study among such a great group of people. She and my fellow group members never hesitated to support my work in whatever way they could—especially by sharing ideas, which is the best part of doing research. Thank you for so many hours of valuable and interesting discussion.

Thanks are due to my thesis committee members, Profs. John Cumings and Manfred Wuttig of the Materials Science department, Prof. Neil Goldsman of Electrical Engineering, and Dr. Tsvetanka Zheleva of the U.S. Army Research Laboratory for their time, advice and support. I would also like to thank my internship supervisor, Dr. Philipp Müller of BASF Ludwigshafen’s TEM lab, for showing me what it’s like to conduct research in German industry. The experience of working in a different environment taught me new ways to make research both productive and fun, and certainly expanded my career horizons.

I would like to acknowledge funding support for this work from several sources¹: The U.S. Army Research Laboratory, for their support of the wide-bandgap semiconductor research; the U.S. Department of Energy, for sponsoring the work on nanocarbon-metal composites; and the U.S. Department of Education’s Graduate Assistance in Areas of National Need (GAANN) Fellowship for supporting my professional development during my final year.

¹Army Research Laboratory Contract No. W911NF1420110, and Department of Energy, Office of Energy Efficiency and Renewable Energy, Award No. DE-EE0008313.

No one person can know and do everything required for such a wide-ranging thesis. I will always appreciate the support of my fellow research group members during my time at UMD: Xiaoxiao Ge and Madeline Morales for their expertise in covetics fabrication and characterization; Josh Taillon, for guiding me through the steep learning curve of the FIB/SEM and introducing me to EELS and hyper-spectral decomposition; and Romaine Isaacs for valuable discussion about covetics and Raman spectroscopy. Thanks to Prof. Sarit Dhar and his group at Auburn University for providing gallium oxide samples and frequently helping me put my TEM findings in a broader context. To the UMD NanoCenter microscopists Dr. Jiancun Rao and Dr. Sz-Chian Liou, thanks for your help and support through the many hours I spent using the FIB and TEM. I would also like to acknowledge the dedication of all the staff members in the department business office, who made sure we got our packages and funding on-time. And thanks to my friends in the department, especially Naila Al Hasan, Zoey Warecki, Joy Chao, and all the members of the TEM users' group meeting at UMD, who were there when I needed someone to challenge, distract, and encourage me.

Table of Contents

Table of Contents	iv
List of Tables	vii
List of Figures	viii
List of Abbreviations	xi
1 Introduction	1
1.1 SiC and Ga ₂ O ₃ wide-bandgap semiconductors	2
1.1.1 Silicon carbide	3
1.1.1.1 Processing techniques and challenges	4
1.1.2 Gallium oxide	6
1.1.3 Goals of this research	7
1.2 Nanocarbon-metal composites (NCMCs)	8
1.2.1 Unique properties of graphene	8
1.2.1.1 Electrical conductivity	9
1.2.2 Established NCMC production strategies	12
1.2.3 Novel fabrication method: Electrocharging assisted process	13
1.2.4 Goals of this research	14
2 Methodology	16
2.1 Analytical transmission electron microscopy	16
2.1.1 Conventional and scanning TEM modes	17
2.1.2 Electron energy loss spectroscopy (EELS)	18
2.1.2.1 Energy-filtered TEM (EFTEM)	22
2.1.2.2 Multivariate analysis of EELS data	23
2.2 Focused ion beam sample preparation	27
2.3 Raman spectroscopy	30
2.4 Effective medium model for bulk properties of composites	33
3 Characterization of wide-bandgap MOS interfaces	37
3.1 SiC: Passivation of electrically active defects with chemical treatments beyond NO annealing	38
3.1.1 Boron interdiffusion and incorporation into SiO ₂	38
3.1.1.1 Methods	39

3.1.1.2	Results and discussion	40
3.1.2	Sb ion implantation in conjunction with NO annealing	47
3.1.3	Summary and future research directions	53
3.2	Ga ₂ O ₃ with deposited SiO ₂ and Al ₂ O ₃ gate oxides	54
3.2.1	Post-deposition annealing effects on the Ga ₂ O ₃ /gate oxide interface structure	54
3.2.1.1	Experimental methods	55
3.2.1.2	Results and discussion	57
3.2.2	Electron beam-induced crystallization of Al ₂ O ₃ gate oxides	68
3.2.2.1	Experimental methods	69
3.2.2.2	Quantification of the crystalline transformation	71
3.2.2.3	Factors contributing to crystallization of the Al ₂ O ₃ gate layer	74
3.2.2.4	Device performance implications and recommendations for future work	81
4	Modeling and characterization of nanocarbon-metal composites	83
4.1	Analysis of C distribution and structure by Raman spectroscopy	84
4.1.1	Distribution of the nano-graphite crystallite size, L_a	84
4.1.1.1	Characteristic long-tailed distribution of L_a after conversion	86
4.1.2	Estimating the thickness of embedded GNRs	90
4.2	TEM investigation of metal-carbon interface structures	93
4.2.1	Specimen preparation and experimental approach	93
4.2.2	Large-scale graphitic carbon structures in Al covetics	95
4.2.3	Well-integrated carbon nanostructures in Al covetics: Analytical TEM-EELS	108
4.2.4	Dislocation structure, microstructure, and mechanical properties of covetics	113
4.3	Effective medium model of electrical conductivity	119
4.3.1	The need for a new model	120
4.3.2	Structural inputs to the model	122
4.3.3	Electronic inputs to the model	125
4.3.3.1	Charge transfer at the metal-graphene interface	125
4.3.3.2	Width dependence of GNR conductivity due to quantum confinement	127
4.3.4	The effective conductivity of a composite with randomly-oriented inclusions	135
4.3.5	Results	137
4.3.6	Discussion	141
4.4	Summary	146
5	Conclusions	148
5.1	Summary of research	148
5.1.1	Wide-bandgap MOS interfaces	148

5.1.2	Nanocarbon-metal composites (Covetics)	150
5.2	Recommendations for future work	152
5.2.1	Wide-bandgap MOS interfaces	152
5.2.2	Nanocarbon-metal composites	153
A	Measurement of electron-beam currents in the field-emission TEM	155
A.1	Approach	155
A.2	Estimating the electron dose rate on the specimen	159
B	Publications and presentations related to this work	161
	Bibliography	165

List of Tables

1.1	Physical properties of Si, SiC, and Ga ₂ O ₃ semiconductors	4
3.1	Material and deposition parameters for gate oxide films on Ga ₂ O ₃ MOS devices	56
3.2	Electron beam conditions (accelerating voltage and current density) and resulting crystallization effects on the Al ₂ O ₃ gate oxide layer . . .	71

List of Figures

1.1	Figure of merit for selected wide-bandgap semiconductors	3
2.1	Schematic of TEM	19
2.2	Schematic of EEL spectrometer	20
2.3	Reference EELS spectrum for Si	21
2.4	Example “scree plot” ordering of principal components by relative significance	26
2.5	Schematic of FIB/SEM	28
2.6	TEM lamella extraction process using the FIB/SEM	29
2.7	Raman reference spectrum of defective graphite	31
2.8	Example Lorentzian fit to a Raman spectrum in a C-rich region of an Al covetic	32
2.9	Examples of the graphitic crystallite size (L_a) distribution	34
2.10	Illustration of a composite with an unknown property to be modeled	34
2.11	Example composite geometries with varying degrees of ordering	35
3.1	HR-TEM of abrupt SiC/BSG interface	40
3.2	Boron pile-up at the interface between SiC/BSG layers revealed by STEM-EELS mapping	42
3.3	Uniform O- K EELS intensity across the SiC/BSG interface	44
3.4	MCR-LLM decomposition of the BSG interface	45
3.5	High-resolution TEM of the Sb-doped SiC/SiO ₂ interface	49
3.6	Si- $L_{2,3}$ EELS edges after Sb+NO annealing	50
3.7	Elemental O- K and Sb- $M_{4,5}$ EELS edges	51
3.8	MCR-LLM decomposition of SiC Sb+NO-annealed EELS spectrum image	52
3.9	HRTEM of Ga ₂ O ₃ /SiO ₂ interface roughness following post-deposition annealing	57
3.10	EELS spectrum image of Ga ₂ O ₃ /SiO ₂ interface	59
3.11	O- K EELS map showing roughness of Ga ₂ O ₃ /SiO ₂ interface following 1000 °C PDA	60
3.12	Ga ₂ O ₃ /Al ₂ O ₃ interface before and after crystallization of the gate oxide under electron irradiation	62

3.13	NMF decomposition of EELS at the Ga ₂ O ₃ /ALD Al ₂ O ₃ interface . . .	64
3.14	NMF decomposition of EELS at the Ga ₂ O ₃ /ALD Al ₂ O ₃ interface after 500 °C PDA	65
3.15	MCR-LLM decomposition of EELS data showing asymmetric diffu- sion following PDA	66
3.16	Lower-magnification TEM of the crystallized Al ₂ O ₃ layer	70
3.17	Average inelastic energy loss from the Al ₂ O ₃ gate oxide as determined by the EELS spectrum	75
3.18	Finite element model of beam-induced heating in Ga ₂ O ₃ /Al ₂ O ₃ TEM lamella	76
3.19	Electron diffraction pattern of the fully crystallized Al ₂ O ₃ layer . . .	77
3.20	Oxygen sub-lattices of the ($\bar{2}01$) β -Ga ₂ O ₃ and (111) γ -Al ₂ O ₃ planes .	78
3.21	Raw EELS data from bulk β -Ga ₂ O ₃ and γ -Al ₂ O ₃ layers with and without PDA	80
3.22	Line profile of the relative Ga- $M_{2,3}$ EELS edge in samples subjected to 500 °C PDA	81
4.1	Distribution of the nano-graphite crystallite size, L_a , in activated C source material	85
4.2	Asymmetric L_a distributions following covetics conversion	87
4.3	The fraction of C converted increased monotonically with reaction residence time	89
4.4	Linear increase in mean L_a with residence time	90
4.5	11 Raman spectra from covetic sample cv20190408 with clearly de- fined 2D bands	92
4.6	Optical imaging and Raman spectra of a polished covetic cross-section	94
4.7	EDS mapping of a graphitic C feature prior to lamella extraction . .	95
4.8	SEM and TEM survey images of covetic lamella cv20190408	96
4.9	Higher-resolution TEM imaging of the graphitic C bulk	97
4.10	EFTEM composition imaging of a graphitic cluster in a covetic lamella	99
4.11	EFTEM of the graphitic carbon/Al interface	100
4.12	Color-enhanced EFTEM images from the C/Al interface	100
4.13	Survey of cv20190408-IM TEM specimen prepared by ion milling . .	101
4.14	STEM-EDS of the Al/C interface structure after ion milling	102
4.15	MCR-LLM decomposition of EDS spectra at the Al/C interface . . .	103
4.16	Cross-sectional TEM lamella of cv20190502	105
4.17	Diffraction- and high-resolution imaging of 2 graphitic regions in cv20190502	106
4.18	EDS line scan across Al/C interface in cv20190502	107
4.19	HRTEM inspection of Al structure near interface with C	108
4.20	TEM-EELS of rod-like graphitic structures in electropolished Al 6061 covetic	110
4.21	TEM imaging of aligned GNRs along a $\langle 111 \rangle$ zone axis	112
4.22	Characterization of a covetic sample subjected to nano-indentation .	114
4.23	Dislocation density estimate under the nanoindented covetic surface .	116

4.24	Trends in covetics' electrical and mechanical performance as functions of charge applied during fabrication	118
4.25	Optical micrographs indicating typical grain sizes of Al 1350 covetic and control	119
4.26	Projected conductivity of nanocarbon-metal composites following the rule of mixtures	121
4.27	Schematic illustrating the orientation of GNRs in a polycrystalline metal matrix	124
4.28	Structure of the Al-GNR-Al interface modeled via DFT	126
4.29	Width dependence of the electron mean free path in GNRs	129
4.30	Effects of W and E_F on the quantum conductance of GNRs	130
4.31	Band bending at the Al-GNR interface	132
4.32	The conceptual finite potential well	133
4.33	Graphical solution for electrons confined to a GNR with a finite potential barrier	134
4.34	Detailed schematic of the interaction between metal matrix and embedded few-layer graphene	137
4.35	Projected effective conductivity of Al-matrix covetics with randomly aligned GNRs based on c-AFM measurements	139
4.36	Effective-medium model based on the GNR ideal quantum conductance	142
A.1	Equipment used for measuring beam currents in TEM	156
A.2	TEM beam current measurements using the EELS drift tube	157
A.3	TEM beam current density measurements using the phosphorescent screen	158
A.4	Estimate of beam diameter via Al_2O_3 gate oxide thickness	160

List of Abbreviations

AFM	Atomic force microscopy
ALD	Atomic layer deposition
BF	Bright field
CLA	Condenser lens aperture
CVD	Chemical vapor deposition
DF	Dark field
DFT	Density-functional theory
DOS	Density of states
EDS	Energy-dispersive X-ray spectroscopy
EAP	Electrocharging assisted process
EELS	Electron energy loss spectroscopy
EFTEM	Energy-filtered TEM
ELNES	Energy loss near-edge structure
EMA	Effective medium approximation
FFT	Fast Fourier transform
FIB	Focused ion beam
FWHM	Full-width at half-maximum
GIF	Gatan image filter
GNR	Graphene nanoribbon
HAADF	High-angle annular dark field
HRTEM	High-resolution transmission electron microscopy
MCR-LLM	Multivariate curve resolution by log-likelihood maximization
MOS	Metal-oxide-semiconductor
MOSFET	Metal-oxide-semiconductor field-effect transistor
MSA	Multivariate statistical analysis
NCMC	Nano-carbon metal composite
NMF	Non-negative matrix factorization
PCA	Principal component analysis
PDA	Post-deposition anneal
POA	Post-oxidation anneal
SEM	Scanning electron microscopy
SI	Spectrum image
SIMS	Secondary-ion mass spectrometry
STEM	Scanning transmission electron microscopy
TEM	Transmission electron microscopy
WBG	Wide-bandgap
XPS	X-ray photoelectron spectroscopy
XRD	X-ray diffraction
ZLP	Zero-loss peak

Chapter 1: Introduction

Microscopy offers powerful techniques for the observation, measurement and alteration of material systems in many fields. In recent decades electron and ion microscopes have enabled in-situ modification of materials, atomic-resolution imaging, and sub-nanometer resolution measurement of chemical composition and bonding. In this work, dual focused ion beam (FIB)/SEM and transmission electron microscopy (TEM) are utilized to illuminate the processing-structure-property relationships of two distinct material systems: wide-bandgap semiconductors and nanocarbon-metal composites. Each of these systems presents significant potential to enhance power transmission and conversion efficiency on large scales, and is therefore of significant societal as well and scientific interest.

In the first half of this thesis, two wide-bandgap semiconductor material systems, silicon carbide (SiC) and gallium oxide (Ga_2O_3), were investigated using analytical electron microscopy methods to identify features of semiconductor/gate-oxide interfaces that affect the performance of microelectronic devices based on these systems. The latter portion of this work is focused on understanding the processing-structure-property relationship of novel nano-carbon metal composites (NCMCs), known as “covetics,” which aim to exploit the superior mechanical and electrical

properties of graphitic nanostructures such as carbon nanotubes and graphene to enhance the bulk properties of alloys based on aluminum and copper. Intended applications for covetics range from microelectronic interconnects to grid-scale power transmission lines as well as structural alloys.

1.1 SiC and Ga₂O₃ wide-bandgap semiconductors

Scientific understanding of semiconductor materials and processes has revolutionized numerous technologies during the 20th century, enabling rapid development of small, efficient computers and power electronics. However, these mainly silicon-based devices are limited to moderate operating temperatures and voltages due to the intrinsic properties of Si, such as its bandgap and thermal conductivity. Wide-bandgap (WBG) semiconductors such as silicon carbide, gallium nitride and gallium oxide have therefore attracted significant interest in recent years. Such materials' wide bandgaps allow devices to operate at higher temperatures and voltages than conventional semiconductors. In addition to greatly extending the range of possible high-temperature and high-voltage applications, wide-bandgap power electronics are anticipated to cut AC-DC- and voltage-conversion losses in consumer electronics, electric vehicle charging, and grid-scale applications by 50–90 % [1].

Inspection of Baliga's figure of merit (BFOM), a metric of semiconductor performance for switching applications defined by breakdown voltage V_{BR} and specific on-resistance R_{ON} further illustrates the potential of wide-gap materials, as depicted in Fig. 1.1 [2]. Furthermore, reductions in the size and weight of power conversion

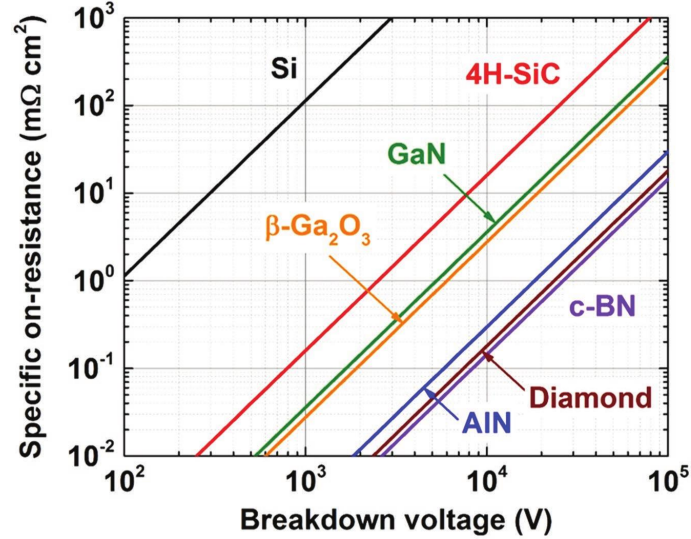


Figure 1.1: Log-log plot showing contours of Baliga’s figure of merit (BFOM) for Si and selected WBG semiconductors. Performance for low-frequency switching devices increases toward the lower-right. Adapted from [2].

equipment will lead to energy savings in the transportation sector, presently one of the most energy-intensive human activities. However, each material system presents its own set of scientific and engineering challenges, exposing gaps in our understanding that will need to be filled in order to unlock their full potential.

1.1.1 Silicon carbide

Silicon carbide (SiC) is an ideal wide-bandgap (WBG) semiconductor for devices operating in high-temperature, high-voltage, high-power and high-radiation environments. Major advantages of SiC relative to Si are presented in Table 1.1; these include high thermal conductivity, large electric field breakdown strength, high bulk mobility, and the ability to form a native thermally-grown SiO₂ oxide [3]. Over 200 polytypes of SiC exist in cubic (C), hexagonal (H), and rhombohedral (R) configurations; hexagonal 4H-SiC is often preferred due to its relatively larger bandgap

Property	Si	4H-SiC	Ga ₂ O ₃
Bandgap E_g [eV]	1.12	3.25	4.85
Dielectric constant ϵ	11.8	9.7	10
Breakdown field E_c [MV/cm]	0.3	2.5	8
Electron mobility μ [cm ² /V s]	1500	1000	300
Thermal conductivity λ [W/cm K]	1.5	4.9	0.23
Baliga's figure of merit = $\epsilon\mu E_c^3$	1	317	3214

Table 1.1: Comparison of the properties of the WBG semiconductors SiC and Ga₂O₃ relative to Si. Adapted from Ref. [8].

and higher intrinsic mobility and breakdown voltage [4]. Devices based on SiC have the potential to substantially improve the performance and efficiency of electric vehicles, aerospace and defense systems, and the electric grid itself [5]. Doping of SiC is only possible via ion implantation, as the diffusion coefficients of the common n -type dopants N or P, and the p -type dopants Al or B, are too low to make diffusion doping practical [6]. Growth and processing technology have matured to the point where SiC-based metal oxide semiconductor (MOS) devices are now commercially available. However, their performance and reliability are far from ideal due to the presence of electrically active defects at the SiC/SiO₂ interface, which reduce the channel mobility and cause threshold voltage instability in SiC MOS field-effect transistors (FETs), especially at high operating temperatures and under thermal cycling [7].

1.1.1.1 Processing techniques and challenges

Greater than 2 orders of magnitude separated the electron mobility of bulk SiC (1000 cm²/Vs) and the mobility in the active region of early experimental SiC-based

devices (less than $10 \text{ cm}^2/\text{Vs}$ [9]). Improvement of the channel mobility has therefore been a major focus of SiC device research. Li et al. found in 1997 that annealing in a nitrous oxide (NO) atmosphere could reduce the interface trap density D_{it} in a SiC MOS capacitor [10]. This discovery was followed in 2001 by the demonstration of an NO-annealed SiC MOSFET with an order of magnitude reduction in D_{it} , which corresponded to a five-fold increase in channel mobility, up to $30\text{--}35 \text{ cm}^2/\text{Vs}$ [9]. Nitrogen is believed to passivate electrically active interfacial defects which may include, for example, Si interstitials contributing to near interface traps (NITs) [11].

Recent experimental treatments based on phosphorus [12] and boron [13] converts the SiO_2 layer into a phosphosilicate or borosilicate glass (PSG or BSG, respectively) and improves carrier mobility upon NO passivation by a factor of 3, to over $100 \text{ cm}^2/\text{Vs}$ in the case of either P [14] or B passivation [13]. Doping the SiO_2 layer with B appears to be the more suitable treatment for device applications, as it avoids the problem of threshold voltage instabilities generated by the polar nature of the PSG material [15, 16]. Antimony (Sb) ion implantation of the SiC channel region in conjunction with NO post-oxidation annealing has also been shown to produce channel mobilities greater than $100 \text{ cm}^2/\text{Vs}$ [17]. Furthermore, combinations of these techniques have been shown to produce even higher channel mobilities, for instance Sb + BSG ($180 \text{ cm}^2/\text{Vs}$, [18]) or an N_2O anneal in conjunction with B doping and additional deposited SiO_2 layer ($170 \text{ cm}^2/\text{Vs}$, [19]). Each of these techniques contribute to improved field-effect mobility μ_{FE} through different mechanisms and present different drawbacks, which require further structural investigation.

1.1.2 Gallium oxide

Despite being among the newest and least mature of the ultra-wide-bandgap (UWBG) semiconductors, gallium oxide (Ga_2O_3) has notable advantages over SiC for certain applications, including the ability to grow wafers economically from the melt [2]. Its bandgap of ~ 4.9 eV gives rise to a breakdown strength of ~ 9 MV/cm, making Ga_2O_3 especially well suited to very high-power applications (above 1 kV), for example in defense and wireless communications [8, 20]. In addition, the large bandgap opens up possibilities for deep UV sensing in a truly solar-blind configuration [21]. Its inherent stability as an oxide will be useful for electronics intended for harsh or high-temperature environments [8]. However, significant challenges remain, including low thermal conductivity, difficulty of p-type doping, and an incomplete understanding of the role played by interfacial defects in limiting device performance [8]. Charge trapping at the interface adversely affects channel mobility and threshold voltage stability, an ongoing challenge in the SiC/SiO₂ system which persists in Ga_2O_3 [2].

Additionally, the choice of gate oxide material (typically SiO₂ or Al₂O₃), deposition method, and process conditions will have significant implications for device performance and reliability that require further investigation [22]. Recent work by Jayawardena et al. [23] indicates that SiO₂ may be the better choice among the gate dielectrics SiO₂, HfO₂, and Al₂O₃ in terms of lower gate leakage and higher breakdown field, consistent with its larger band offset on Ga_2O_3 . Despite these advantages, the density of electrically active defect states at the interface (D_{it}) was

higher with SiO₂ gate dielectric as compared to interfaces with Al₂O₃, suggesting that there is room for improvement.

1.1.3 Goals of this research

Wide-bandgap MOS technology based on SiC has been well validated in recent years and has been rapidly expanding in the market, largely owing to the success of NO post-oxidation annealing [24]. Nevertheless, there is still significant room for improvement before approaching the bulk mobility of SiC, and the mechanisms of recently developed passivation treatments are not yet well understood. This work provides nanoscale structural characterization via (HR)TEM and STEM-EELS of previously little-known phenomena such as boron doping and antimony ion implantation of 4H-SiC.

Gallium oxide MOS technology is significantly less mature, with the first field-effect transistor only reported in 2012 [25]. Consequently, many aspects of the structure-property relationships governing Ga₂O₃ device performance remain poorly understood. This work aims to address open questions regarding the semiconductor/gate oxide interface structures responsible for recently observed degradation in devices' electrical characteristics depending on the choice of gate oxide, its deposition parameters and post-deposition annealing conditions.

1.2 Nanocarbon-metal composites (NCMCs)

The addition of carbon to metals is an ancient technique for improving desirable properties, such as tensile strength, resistance to oxidation and wear resistance, of metals such as iron. Unlike steel, the solubility of C in common alloys based on Al and Cu is generally limited to a few parts per million [26]. Thus, traditional metallurgy techniques cannot be used to enhance the desired properties of these metals, primarily strength and electrical and thermal conductivity, which are significant for applications in electricity transmission from the smallest integrated circuit (IC) interconnects to the largest grid-scale transmission lines. Since Al and Cu are ubiquitous in these applications, and nanostructured forms of C such as graphene [27] and carbon nanotubes (CNTs) [28] have exceptionally high tensile strength and charge carrier mobility with demonstrated commercial applications in polymer-nanocarbon composites [29], it stands to reason that significant industrial gains may be realized through the incorporation of nanostructured carbon in metals.

1.2.1 Unique properties of graphene

Graphene, the first readily available two-dimensional (2D) atomic crystal, exhibits exceptional properties that may enable a range of new technologies encompassing energy transfer and storage, sensors, electronics, and structural applications [30, 31]. Its properties have been predicted theoretically since the 1940s [32], but the stability of free single layers of graphene was not demonstrated experimentally until 2004, by Novoselov, Geim and co-workers using the “Scotch tape method”

to reproducibly isolate single atomic layers from bulk graphite [27]. Within 10 years scientific interest in graphene had grown exponentially into the thousands of publications [31].

1.2.1.1 Electrical conductivity

The electrical conductivity of graphene is affected by a number of factors. It is instructive to consider the conductivity σ as a function of the carrier concentrations and mobilities:

$$\sigma = e(n\mu_e + p\mu_h) \quad (1.1)$$

where e is the elementary charge of the electron, n and p are the electron and hole number densities, and μ_e and μ_h are their respective mobilities. All of these variables are affected by extrinsic factors, including the choice of substrate (or lack thereof) and associated impurities [33, 34], adsorbates on the surface [35], external potential [36], temperature [37, 38], as well as the defects inherent in the graphene itself, such as edges [39].

Factors affecting carrier density in graphene

The band structure of ideal graphene is semimetallic, with zero band gap and approximately linear density of states as a result of its 2D structure [32, 35]:

$$D_{2D}(E) = \frac{2|E|}{\pi\hbar^2\nu_F^2} \quad (1.2)$$

Mobile charge carriers (electrons or holes) are induced by an applied gate voltage V_g , with linear dependence demonstrated experimentally: $n = \alpha V_g$, where $\alpha = 7.3 \times 10^{10} \text{ cm}^{-2} \text{ V}^{-1}$, in good agreement with theory ($\alpha = 7.2 \times 10^{10} \text{ cm}^{-2} \text{ V}^{-1}$), which implies that all of the induced carriers are mobile [36]. Many fundamental studies have been undertaken to study unusual phenomena at low carrier densities, for example Ref. [33]. The development of specialized structures such as ionic-liquid gates has also enabled the exploration of high carrier-density regimes where $n > 10^{14} \text{ cm}^{-2}$ [40]. In that work it was shown that bi- and tri-layer graphene are capable of sustaining large conductivities, beyond the point at which the conductivity of single-layer graphene would saturate, due to the availability of additional energy bands.

The carrier density of graphene is also controllable via doping. This may be done through surface transfer (electron exchange between graphene and adsorbates or surfaces in close proximity), or by substitution of species into the graphene lattice, such as B or N for p - and n -type doping, respectively, as with conventional semiconductor technology [41]. Some degree of doping is inevitable in real systems, whether from the substrate, residual chemical species used in processing, or the ambient atmosphere. Graphene is also doped by adsorption on to a metal surface. First-principles calculations at the level of density-functional theory (DFT) show that graphene is weakly adsorbed on metals including Cu, Al, and Ag, where it is doped with electrons depending on the difference in work function between the metal and graphene [42, 43]. The transfer of electrons was greatest on the Al(111) surface, followed by Ag and Cu [43]. (111) metal surfaces were chosen in that work

to minimize lattice mismatch with the graphene sheet, which was 0.8–3.8% depending on the metal. Further DFT studies have predicted electron densities on the order of 10^{14} cm^{-2} in bilayer graphene trapped between Cu [44] and Al [45].

Factors affecting carrier mobility in graphene

The mobility of carriers in graphene is substantially influenced by the substrate. The highest mobilities have been reported for suspended graphene, on the order of $2 \times 10^5 \text{ cm}^2/\text{Vs}$, but only after removal of impurities adsorbed on the surface, which are responsible for significant (extrinsic) scattering [34]. On ideal substrates such as hexagonal boron nitride (h-BN), which is atomically smooth with relatively few charged impurities, graphene can exhibit carrier density-independent mobilities of around $60,000 \text{ cm}^2/\text{Vs}$, three times larger than for graphene on SiO_2 [46].

In addition to the extrinsic scattering of carriers due to charged impurities, there are intrinsic scattering mechanisms such as electron-phonon interactions, which cannot be eliminated from a system in a real device. Fortunately, these have been shown theoretically to be quite small [37, 47], such that the intrinsic mobility μ_{in} can exceed $300,000 \text{ cm}^2/\text{Vs}$ for bilayer graphene at 300 K, even greater than in single-layer graphene, with a corresponding mean free path on the scale of microns [47]. Unlike the extrinsic mobility, the intrinsic mobility depends on the carrier density as $\mu_{in} \propto 1/n$ [37, 38, 48]. Ballistic transport with path lengths in excess of $10 \mu\text{m}$ has been observed experimentally in graphene nanoribbons grown on SiC substrates, corresponding to a sheet resistance on the order of $1 \Omega/\text{sq}$. [49].

1.2.2 Established NCMC production strategies

The first major Al-CNT composites prepared by powder metallurgy and ball milling have shown increasing yield strength with volume fraction of multiwall carbon nanotubes (MWNTs); however, the mechanism of strengthening could not be determined by TEM imaging [50]. Al-CNT composites have also been prepared using a chemical vapor deposition (CVD) technique in order to address the problems of CNT agglomeration and damage caused by traditional metal-matrix-composite preparation techniques, nearly doubling the tensile strength compared with the traditionally-prepared composite [51]. Al-0.3 wt.% graphene nanosheet composites prepared by flake powder metallurgy have resulted in 62% improvement in tensile strength [52]. However, a similar Al-graphene composite prepared by ball milling exhibited diminished strength and hardness, likely due to the formation of aluminum carbide (Al_4C_3) at the defect sites of graphene, such as the edges of nanosheets [53].

Much variation exists in the nanostructured C distribution, effect of carbide formation and performance of Al-CNT and Al-graphene composites produced using the above mechanical methods. It is therefore desirable to investigate alternative methods to produce nanocarbon-metal composites with fewer processing steps and greater retention of the sp^2 carbon network responsible for the composite's enhanced structural and electrical properties. Model systems indicating the potential gains of such improvements have recently been modeled and fabricated. Mu Cao and co-workers embedded graphene within Cu by growing monolayer graphene on Cu foils via a chemical vapor deposition (CVD) process, followed by stacking and hot

pressing [44]. Bulk improvement in electrical conductivity attributed to the presence of graphene was reported to be 5.2% with as little as 0.008% volume fraction of C, with local conductivity up to 3 orders of magnitude greater than the Cu matrix at the Cu/Graphene interface. Extending the technique to Al foil was possible but required that the graphene be grown apart from the foil and transferred externally, as Al is not a suitable substrate for CVD of graphene [45]. A further drawback of the fabrication technique used here is the limited sample size, which were under 2 cm \times 2 cm, precluding economies of scale.

1.2.3 Novel fabrication method: Electrocharging assisted process

A fabrication process amenable to efficient scale-up will be important for commercialization of nanocarbon-metal composite materials. One such technique is the electrocharging assisted process (EAP), developed by Third Millennium Materials, LLC in 2010 [54]. By applying a large direct current to a metal melt containing on the order of 1 wt.% C (powdered activated carbon), it is possible to incorporate carbon into a matrix of various metals including Au, Ag, Al, Cu and other metals. The resulting high-carbon composites are known as *covetics*. Carbon structures in covetics remain incorporated even after subsequent re-melting, indicating the presence of carbon-metal bonding. Electron-beam and pulsed laser deposition of Cu covetics made by EAP have been demonstrated with potential applications in transparent conducting electrodes [55]. Additionally, Al covetics made with commercially available Al 6061 alloy and 3 wt.% C have been shown to contain primarily sp^2 -bonded

C [56] and to exhibit up to 30% greater tensile strength and up to 43% greater electrical conductivity than a typical Al 6061 alloy [57].

The ability of electric current to induce ordering in amorphous carbon (a-C) has been demonstrated in well-controlled fundamental studies. A transition from amorphous to graphitic C was observed in an investigation of flash sintering of electronic conductors, which applied current densities of up to 175 A/mm² to fibers of a-C over periods of several minutes [58]. The graphitic transformation was confirmed by Raman spectroscopy and X-ray diffraction (XRD), which both indicated the narrowing of characteristic peaks. Transformation of a-C to graphene was also observed in real time on a suspended graphene substrate via in-situ TEM experiments [59]. C was naturally present in the form of hydrocarbon contamination in the TEM column or adsorbed on the sample holder, and a-C was deposited through the assistance of the electron beam, which caused decomposition of the contamination. Crystallization of a-C into graphene was subsequently facilitated by current-induced heating to 2000 °C or greater via electrical contacts integrated in the holder.

1.2.4 Goals of this research

Covetics may ultimately lead to commercially available alloys that have greater mechanical strength, wear resistance, and electrical and thermal conductivities suitable for many applications. To reach this point, several outstanding challenges must be understood and resolved. These include ensuring complete sp^2 conversion of the

carbon precursor material, ordering into graphitic structures with superior electrical transport properties, and ensuring uniform distribution of incorporated carbon. Furthermore, structural features of the metal matrix such as grain size, distribution of secondary phases, and dislocation density continue to be relevant in governing the electrical and mechanical properties. Even the magnitude of potential enhancements to electrical and thermal conductivity and mechanical strength in coveotics have not yet been quantitatively estimated.

Fundamental characterization studies such as those facilitated by electron microscopy provide much needed structural information that can be correlated to properties and ultimately used to improve the processing techniques, leading to commercially viable coveotics with uniformly enhanced properties. The goal of this work is to build understanding of processing-structure-property relationships in coveotics via microscopy studies of coveotics fabricated and post-processed under a range of conditions. Additionally, the effective properties of the bulk coveotic composites are predicted using numerical models and properties of metal-carbon systems measured from characterization studies. Modeling is an important complement to experimental fabrication and characterization of coveotics, which often exhibit non-uniform or non-ideal structures (e.g. due to imperfect mixing of C particles in the melt). A theoretical approach will serve to demonstrate the full potential of coveotics with different compositions and structures, thus providing a roadmap for future research and development within this class of materials.

Chapter 2: Methodology

2.1 Analytical transmission electron microscopy

The transmission electron microscope (TEM) is a versatile instrument for many types of high-resolution imaging and spectroscopy. The basic design of a TEM is similar to that of an optical microscope, except using a beam of electrons instead of visible light to obtain much greater resolution—down to the level of the atomic lattice. Electron energies in TEMs typically range from about 80–200 keV, but can be greater than 1 MeV in the highest-energy implementations. The advantage of electrons over visible light is approximately illustrated by the Abbe diffraction limit, representing the theoretical smallest resolvable feature (d) in an optical system illuminated by a wavelength λ :

$$d = \frac{\lambda}{2n \sin \theta} \quad (2.1)$$

where n is the refractive index of the medium and θ the half-angle of convergence. For the highest energy visible light, $d \approx 200$ nm. In contrast, 80–300 keV

electrons travel at relativistic speeds, with a de Broglie wavelength λ given by

$$\lambda = \frac{h}{p} = \frac{h}{\sqrt{2m_0eV \left(1 + \frac{eV}{2m_0c^2}\right)}} \quad (2.2)$$

where h is Planck's constant, m_0 is the rest mass of the electron, e is the elementary charge of the electron, p is the momentum of the electron, V is the accelerating voltage of the electron beam, and c is the speed of light.

Analytical electron microscopy refers to the capability for identifying specific chemical composition and bonding configurations within the specimen, e.g. from inelastic scattering of the electrons with characteristic energy transitions. This principle is commonly implemented in electron microscopy via energy-dispersive X-ray spectroscopy (EDX or EDS), which makes use of characteristic X-rays emitted due to incident electrons causing excitations within the specimen's inner-shell electrons. Another technique specific to TEM is electron energy loss spectroscopy (EELS), which is capable of providing extremely high spatial- and energy-resolution chemical information from the specimen and is obtained from the energy lost by incident electrons after interaction with the sample.

2.1.1 Conventional and scanning TEM modes

The primary instrument used in this work is the JEOL JEM 2100F field-emission TEM at the University of Maryland Advanced Imaging and Microscopy Laboratory (UMD AIMLab). It is capable of 0.19 nm point-to-point resolution in conventional TEM mode and a spot size as small as 0.2 nm in STEM mode. Fig. 2.1

illustrates a typical TEM operating in conventional mode, where a broad parallel electron beam illuminates the sample. This mode is used for high-resolution (HR) TEM and selected area diffraction (SAD). It is also possible to focus the beam to a point in the specimen plane using scanning TEM (STEM) mode, which is particularly useful for high spatial-resolution analytical techniques such as EDS or EELS. STEM enables imaging and spectroscopy utilizing the electrons transmitted through the specimen at a particular point, but with a much smaller excitation volume than from a thick sample as in scanning electron microscopy (SEM); therefore, the spatial resolution of analytical techniques such as EDS is vastly improved over SEM. In order to make full use of the scanning probe's spatial resolution, sample drift and vibrations must be minimized.

2.1.2 Electron energy loss spectroscopy (EELS)

Electron energy loss spectroscopy (EELS) is a highly sensitive material characterization technique that is capable of sub-nanometer spatial resolution when performed in STEM mode. In EELS, the energy lost by electrons' interactions with the sample is recorded by a spectrometer below the TEM column, which separates and counts electrons by their energy remaining after passing through the specimen using a magnetic prism and CCD detector. A schematic illustration of an EEL spectrometer similar to the instrument used in this work, the Gatan Image Filter (GIF), is shown in Fig. 2.2 [61]. The energy loss for each scattering event is simply the reduction from the known initial value (e.g., typically 200 keV in this work).

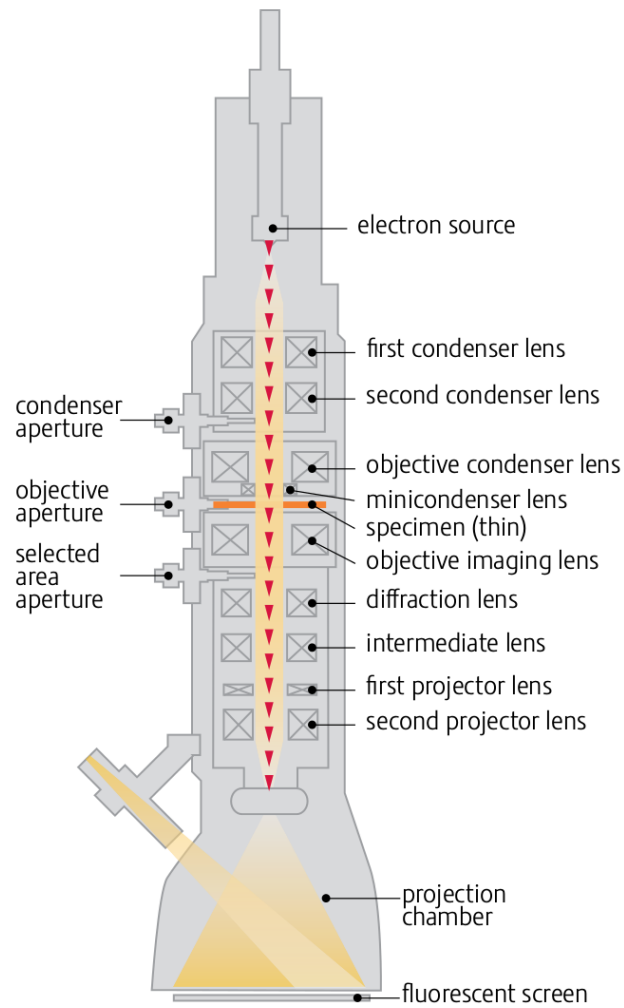


Figure 2.1: A typical TEM operating in conventional TEM mode, with a parallel electron beam (formed by the condenser lenses) illuminating the sample. The image is projected by the intermediate and projector lenses on to a fluorescent screen or captured on a CCD located below the screen. Apertures are used to reduce the beam intensity or to select certain regions of the sample or diffraction pattern for analysis. Adapted from FEI [60].

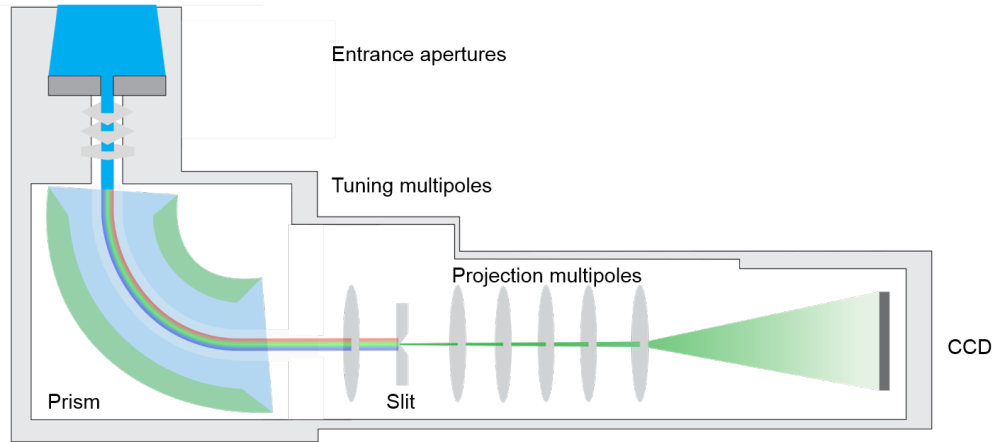


Figure 2.2: Schematic of an EEL spectrometer similar to that employed for this work. After passing through an entrance aperture suitable for the chosen measurement (imaging or spectroscopy), the beam is split by energy through the magnetic prism and projected on to the CCD for counting (in spectroscopy) or constructing an image (as in energy-filtered (EF)TEM). The slit inserted after the prism is used to select signals within a chosen energy range for EFTEM imaging. Adapted from eels.info (Gatan, Inc.)

The magnitude of energy loss is characteristic of the elemental composition of the sample as well as the specific physical phenomena involved in the scattering event. If the specimen thickness is on the order of or greater than the electron mean free path for the material and electron excitation voltage in question, a substantial fraction of incident electrons may be scattered multiple times, resulting in energy loss counts that represent the sum of all the interactions; for this reason it is essential that TEM specimens be thinner than 100–150 nm for EELS analysis [62].

A related challenge is the build-up of hydrocarbon contamination under the STEM probe which interferes with STEM-EELS spectrum imaging. Adsorbed contaminants can diffuse along the specimen surface toward the probe, building up a thick layer that obscures the specimen. This effect makes it particularly challenging to acquire large maps or weak EELS edges that require longer exposure times. A simple preventive measure is the “beam shower,” in which the sample is illuminated

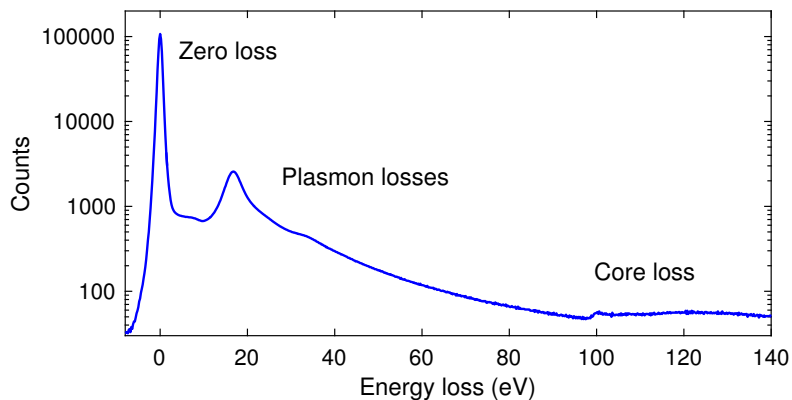


Figure 2.3: A reference EEL spectrum for elemental Si plotted on a logarithmic scale, showing typical features from the strong zero-loss peak through the first Si core-level excitation. Adapted from the Gatan EELS Atlas [64].

with a broad beam in conventional mode for a few tens of minutes, which serves to polymerize and immobilize contaminants on the surface [63].

Since most electrons pass through the sample without measurable energy loss—by passing through undeflected or scattering elastically—the strongest peak of the EEL spectrum is the *zero-loss peak*, centered at 0 eV by definition. The width of the peak (typically reported as full-width at half-maximum, or FWHM) is also used to determine the resolution of the spectrometer. In this work the zero-loss peak FWHM ranged from 0.9–1.1 eV.

Peaks between about 4–40 eV are due to inelastic scattering via excitations of outer shell electrons, primarily plasmon oscillations within the lamella. This region is known as the low-loss region of the spectrum [62]. At higher energies, excitations from the core-shell comprise the core-loss region, which for example in Si (the Si- $L_{2,3}$ edge) is visible at 99 eV in Fig. 2.3. This value corresponds to the approximate binding energy of the $2p$ electrons in Si, and is therefore the minimum energy or

ionization threshold required to excite a core-shell electron in Si into the conduction band. This mechanism explains the asymmetrical edge shape of many core-shell EELS excitations; some core-shell electrons are excited to above the conduction band edge, giving the EELS signal some intensity at energies above the edge—the *fine structure*—which typically exhibits small variations in intensity within a few tens of eV beyond the edge onset [62]. When viewed at sufficiently high energy resolution, the fine structure of EELS edges provides information about the energy band structure and chemical bonding configuration of the corresponding element in the specimen [62]. The fine structure can be used to distinguish between different forms of an element or compound, such as the Si- $L_{2,3}$ shift distinguishing between Si in SiC vs. SiO₂ [65] or the valence state of an ion. Thus, insight may be gained into the relationship between physical and electronic structure and properties of materials such as at the semiconductor/oxide interface of SiC and Ga₂O₃ MOS devices.

2.1.2.1 Energy-filtered TEM (EFTEM)

In addition to spectroscopy, the magnetic prism of the EEL spectrometer is capable of filtering the transmitted electrons in conventional TEM mode, to produce an image using only a selected range of transmitted electron energies. This technique is known as energy-filtered TEM (EFTEM) and can be used to enhance contrast of phases with energy-loss signals at the selected energies. With its ability to image a large spatial area at low energy resolution, EFTEM may be considered

complementary to STEM-EELS. An application of EFTEM to an Al-C composite system is presented in Sec. 4.2.2.

2.1.2.2 Multivariate analysis of EELS data

Challenges in EELS data analysis

Several factors complicate the analysis of EELS data in comparison to other types of spectroscopy. The first is simply the large volume of data collected from each sample. In EEL spectrum imaging, the scanning TEM probe is rastered across the region of interest to collect a spectrum at each point in an array of up to several hundred pixels per side. A single experiment can easily produce over one gigabyte of raw data, rendering any less-than-fully-automated signal processing impractical. Specific to EELS, the signal intensity can vary by several orders of magnitude across the range of energies observed, as in the semi-log plot in Fig. 2.3. Some aspects of the fine structure are weak relative to the background, especially at high energies, and the long tails of core-loss edges can overlap strongly with each other. Furthermore, the regions of greatest interest are often interfaces or inclusions occupying only a small part of the total area in the spectrum image, and whose EELS signature is not independently known.

One traditional method to interpret EELS spectra includes multiple linear least squares (MLLS) fitting [66]. The spectra collected are assumed to be linear combinations of chosen reference spectra, and the fitting algorithm computes each component's weight and the overall residual. Large residual indicates the need

for one or more additional components; however it does not suggest what these components may look like. The MLLS technique is additionally subject to the bias inherent in manually choosing reference spectra.

Algorithms for multivariate statistical analysis

Multivariate statistical analysis (MSA) is a broad class of techniques that offer an approach for dealing with data in multiple dimensions. They are well suited to datasets that are large and contain multiple variables (*i.e.* physical contributions to the EEL spectra) or subtle correlations between variables [67]. MSA began to attract attention within the EELS community several decades ago [68–70] and has been demonstrated as a tool for describing localized interface-specific phenomena since around that time [70]. Essentially, an EELS spectrum image, with spatial dimensions (x, y) and spectral data E , may be considered as a matrix $\mathbf{D}_{(x,y),E}$ [71,72]. Using the *Principal Component Analysis* (PCA) approach, \mathbf{D} may be decomposed into a product of

$$\mathbf{D}_{(x,y),E} = \mathbf{S}_{(x,y),n} \times \mathbf{L}^{\mathbf{T}}_{(E,n)} \quad (2.3)$$

where the rows of the *loading* matrix $\mathbf{L}^{\mathbf{T}}_{(E,n)}$ represent the eigenvalues (independent, orthogonal component spectra), and the columns of $\mathbf{S}_{(x,y),n}$, the *score* matrix, represent their spatially varying intensities. The eigenvectors of $\mathbf{L}^{\mathbf{T}}$ comprise a new set of basis vectors for the dataset which are oriented along the directions of maximum variance. Sorting the components by relative intensity, one can estimate which are physically significant and which are simply noise. PCA is not ideally suited to EELS,

however, as its primary constraint—orthogonality between principal components—rarely applies to EEL spectra, which share background and elemental features in common within a dataset.

The application of physically relevant constraints makes multivariate statistical analysis more meaningful. *Non-negative matrix factorization* (NMF) is well suited to EELS data for this reason. Like PCA, NMF seeks to identify components which maximize variance within the dataset—subject to the requirement that all elements in \mathbf{S} and \mathbf{L} be greater than or equal to zero, as in real physical spectra. NMF is always an additive process for this reason, leading to a “parts-based representation” of the dataset [73]. This technique is applicable to a wide range of problems in the computer science community, such as image recognition, and interest is growing quickly among material scientists and microscopists; the number of Google Scholar results for the relevant terms taken together (“transmission electron microscopy,” “EELS,” and “non-negative matrix factorization”) increased from only 10 articles in June 2016 [72] to 135 by November 2020.

Beyond NMF, the microscopy community continues to innovate in the area of multivariate statistical analysis. *Multivariate curve resolution* (MCR) is a subclass of NMF which applies additional physically meaningful constraints including that components’ intensities always sum to unity. This algorithm was successfully applied to a challenging 7-phase, low-intensity EELS dataset by Braidy and co-workers in 2019 using a Poisson log-likelihood maximization (MCR-LLM) [74]. In low-signal datasets MCR-LLM was demonstrated to outperform other multivariate signal decomposition approaches including NMF. Due to rapid evolution at the

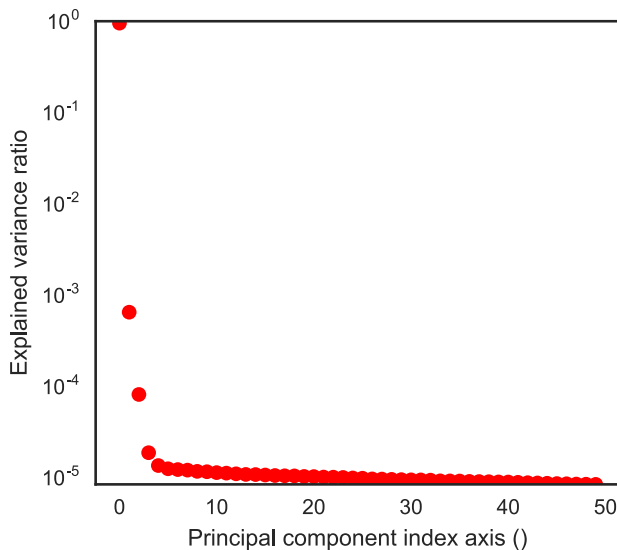


Figure 2.4: Example of a scree plot generated by PCA of a B-doped SiC/SiO₂ interface (discussed in Sec. 3.1.1). Each orthogonal component is presented in descending order of significance as indicated by the fraction of overall variance it represents. A qualitative guideline to distinguish physically meaningful components from noise is that the components above the elbow are significant; in this case, 3 or plausibly 4.

intersection of multivariate statistical analysis and its applications to microscopy, an additional goal of this work is to explore and document the use of novel techniques, such as MCR-LLM, to draw meaningful conclusions from weak-signal EELS data.

Software and approach for applying multivariate statistical analysis to EELS SIs

Thanks to recent interest in “big data,” machine learning, and related areas, open-source software packages implementing PCA and NMF algorithms are freely available. The HyperSpy software package [75] is a powerful Python package for analysis of EELS, EDS and other spectral data and was used extensively in this work. In general, the approach is to estimate the number of physically meaningful components by inspection of a scree plot (a ranking of orthogonal components in

descending order of significance) generated by PCA, as depicted in Fig. 2.4. The number of components above the elbow provides a reasonable initial guess of how many are physically meaningful, as opposed to random noise. Subsequently, the dataset is analyzed by NMF using the number of components suggested by the scree plot, plus or minus one, and the resulting factorizations are compared to identify the most reasonable explanation of the EELS data. A similar approach was taken to apply the MCR-LLM algorithm via a publicly available Python code provided by the algorithm's authors [74]. Applications of this technique to wide-bandgap semiconductor interfaces are discussed in Chapter 3.

2.2 Focused ion beam sample preparation

The focused ion beam (FIB) is a microscope in its own right, with a principle of operation similar to that of an SEM, except with a beam formed by ions, e.g. Ga^+ , instead of electrons. When accelerated to energies of 2–30 keV, the beam of massive ions is capable of localized sputtering of the sample surface; thus the FIB/SEM is a powerful tool for material modification and analysis. A typical dual-beam FIB/SEM is illustrated in Fig. 2.5. The combination of both beams in one system with a single vacuum chamber allows for near-simultaneous imaging and specimen modification. A gas injection system (GIS) is used in conjunction with the ion beam to selectively deposit materials such as W or Pt via organometallic precursor gases; the metal is selectively deposited only where the gas is impacted and decomposed by the ion beam. This functionality allows protective capping layers to be laid down prior to

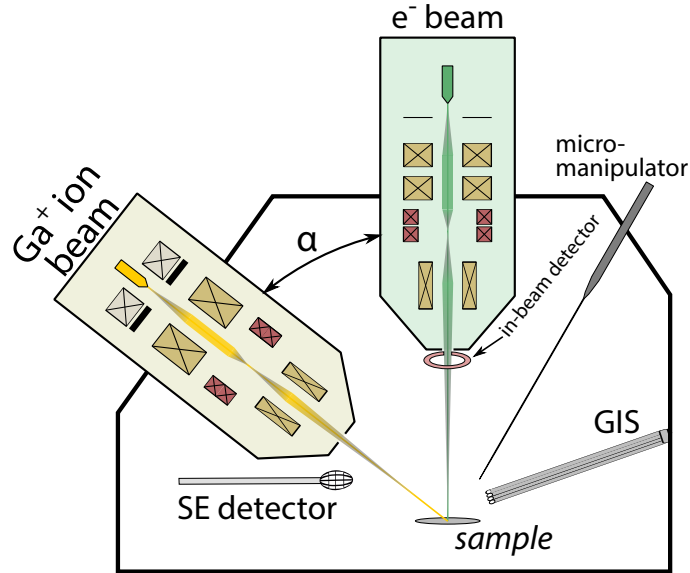


Figure 2.5: Dual FIB/SEM schematic showing the 2 primary beams separated by the angle α (55° for the tools used in this work). The ion beam is used to mill around the region of interest and to thin the final TEM lamella. A W micromanipulator probe is used to transfer the lamella from the bulk material to the grid, and the gas injection system (GIS) is used to deposit protective Pt or W capping layers and to attach the lamella to the probe and the grid. Figure adapted from [72] and [76].

milling in order to protect shallow features from ion implantation damage, or to adhere objects together, as when attaching the specimen to a specialized TEM grid (e.g. Fig. 2.6 at left).

Cross-sectional transmission electron microscopy (TEM) specimens in this work were prepared using the Tescan GAIA (Ga⁺) dual FIB/SEM at the UMD AIMLab. The GAIA FIB was also equipped with a W micromanipulator probe to extract sample cross-sections (TEM lamellas) and mount them to Cu TEM grids. It was therefore possible to precisely select a region of interest on a device, extract the specimen, and thin the lamella to electron transparency (typically < 100 nm) completely inside the FIB/SEM chamber. Analytical instruments commonly present in SEMs were also available in the GAIA and other FIBs, such as Energy Dispersive X-

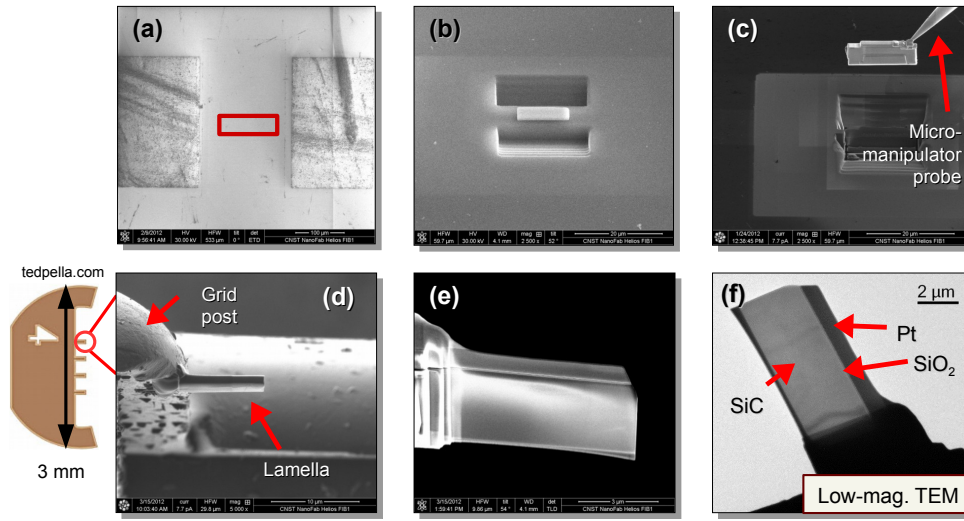


Figure 2.6: Process of TEM lamella preparation in the dual FIB/SEM. (a–b) Selection of the region of interest, deposition of protective Pt layer, and milling of trenches; (c) Lift-out using W micromanipulator probe and (d) attachment to Cu TEM grid; (e) SEM image of the final thinning result at low beam energy and current; (f) Low-magnification TEM image showing the electron-transparent lamella. Adapted from Ref. [72].

ray Spectroscopy (EDS) and Electron Backscatter Diffraction (EBSD), which make the FIB/SEM a uniquely powerful microscopy tool.

Fig. 2.6 outlines the process of TEM lamella preparation in the FIB. After selecting the area of interest, a 2–3 μm thick W or Pt protective cap is deposited using the GIS to prevent amorphous damage from the ion beam from reaching the interface during later stages of the process (Fig. 2.6(a–b)). The depth of damage is beam voltage- and material-dependent, but can be 35 nm or more for a 50 keV Ga beam on Si [77]. After rough milling at 30 kV and cutting under the lamella with the ion beam, a W nanomanipulator probe is used to transfer the lamella to a Cu TEM grid as shown in Fig. 2.6(c–d). Finally, the specimen is thinned at low

ion beam current and low voltage (first 5 kV, then 2 kV) to reduce the sample thickness to 50–90 nm while minimizing surface amorphization damage from the ion beam. The finished lamella (Fig. 2.6(e), in SEM) is electron-transparent in the TEM (Fig. 2.6(f)).

2.3 Raman spectroscopy

Raman spectroscopy is a versatile way to identify molecules and bonding configurations. It is an optical technique whereby a small fraction of incident photons (on the order of 1 in 10^7) are inelastically scattered due to interaction with vibrational modes of the molecules under illumination [78]. The energy shift is equal to the energy lost to (or gained from) the vibrational mode, which is specific to the atomic configuration. Raman spectroscopy is effective for preliminary non-destructive characterization of bulk samples.

Characterization of carbon materials by Raman is well established in the literature. Graphite exhibits 3 distinct Raman signatures: a first order “graphitic” or G peak around 1582 cm^{-1} , a disorder or D peak near 1350 cm^{-1} , and second order G’ peak at 2700 cm^{-1} (also known as the 2D peak since its energy shift is about twice the magnitude of the D peak at 1350 cm^{-1}) [79, 80]. These features are illustrated in Fig. 2.7. Defects contributing to the D peak include the edges of graphene nanoribbons where the symmetry of the structure is broken. For the case of more disordered or amorphous carbon (e.g. activated C), the D band appears

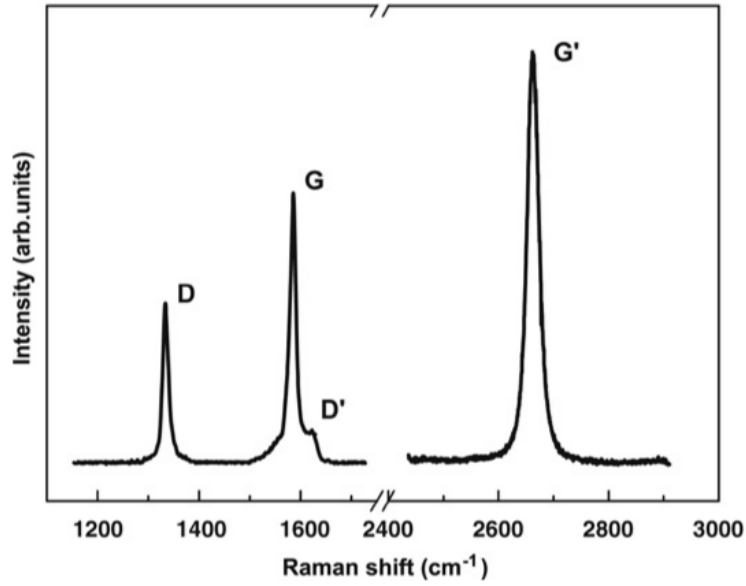


Figure 2.7: Raman spectrum of a graphite sample with defects. The G and G' peaks arise from sp^2 bonding of carbon, while the D and D' are due to broken symmetry such as at the edges of graphene nanoribbons. Adapted from [80].

stronger relative to the G band than in more ordered C, and both the D and G bands are broader; and the 2D band is substantially weaker or absent [81].

Raman spectra in this work were obtained using a Horiba LabRAM ARAMIS confocal Raman system with a 532 nm laser excitation source. Using the highest available optical magnification (100x) produced a laser spot size slightly smaller than $1\ \mu\text{m}$ in diameter. To capture the spatial variability of C distributions in covetics and to increase the volume of data available for statistical analysis, Raman spectrum images (maps) of $11 \times 11\ 1\text{-}\mu\text{m}$ square pixels were typically collected at each region of interest.

Graphitic peak information was extracted from Raman data via non-linear iterative curve fitting routines implemented in Matlab [82]. Lorentzian peaks were fit to the D, G, and 2D bands, at 1350 , 1580 , and $2700\ \text{cm}^{-1}$, respectively, with initial

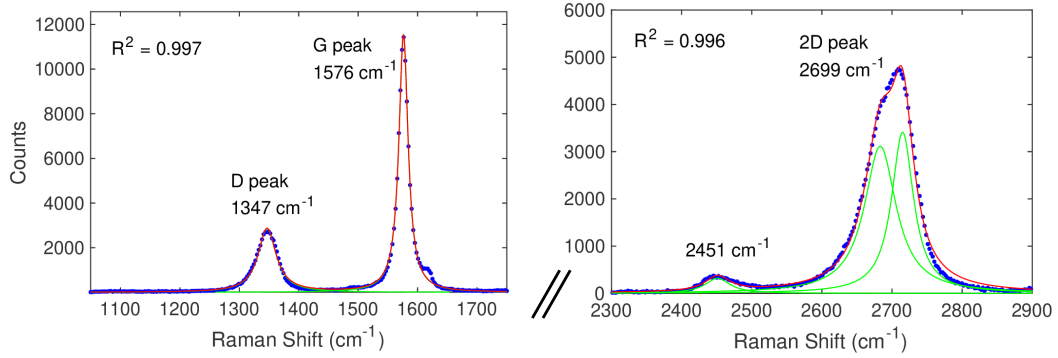


Figure 2.8: Example of Lorentzian fits (green curves) to the D, G, and 2D features of a single-point Raman spectrum (blue data points) in a C-rich region of an Al covetic. The strong G and 2D peaks are indicative of a high degree of graphitic ordering. Note the break in scale.

positions given by the literature [79, 83]. The best of three iterations was chosen for each fit. Example fits from a single graphitic Raman spectrum in an Al6061 covetic alloy are displayed in Fig. 2.8. Customized Matlab scripts written for this work were used to compile statistics of Raman data relevant to graphitic carbon and to covetics. These scripts applied the curve-fitting routines from Ref. [82] to each spectrum in a dataset which typically consisted of a collection of several spectrum images taken from representative points on a cross-section of the sample. To obtain accurate statistics it was necessary to filter out artifacts in the Raman spectra, such as poor background fits or spurious Raman signals from adsorbed hydrocarbons and other contaminants. These were excluded from the subsequent analyses by removing poor fits with $r^2 < 0.9$ or where any peak was shifted by greater than 50 cm^{-1} away from its initial position, which would be likely to have a non-physical origin.

A commonly used metric of disorder in graphitic carbon is the ratio of the D peak intensity, $I(D)$, to the G peak intensity $I(G)$, first introduced by Tuinstra and

Koenig [79]. The domain of validity of this relationship extends to nano-crystallites as small as ≈ 2 nm [81]. It has been demonstrated that the $I(D)/I(G)$ ratio is inversely related to the width of the graphitic crystallites, L_a , by a constant which depends on the excitation laser energy following Eq. 2.4 [84, 85]:

$$L_a = \frac{560}{E_l^4} \left(\frac{I_D}{I_G} \right)^{-1} \quad (2.4)$$

where E_l is the excitation laser energy in eV (in this work, 2.33 eV, equivalent to 532 nm) and 560 is an empirically determined constant. This relationship was validated by comparison with scanning tunneling microscopy (STM) and X-ray diffraction (XRD) measurements [84]. Ultimately, Eq. 2.4 made it possible to compute the nano-graphite crystallite size corresponding to every spectrum in each Raman map, and therefore to both identify the locations of ordered graphitic carbon produced in the covetics process (for further localized characterization) and to build a statistical distribution of crystallite sizes representative of the sample in question overall. An example of the reduced Raman spectrum image showing the spatial distribution of L_a and the corresponding histogram is shown in Fig. 2.9. Applications of this approach to the characterization of covetic materials are presented in Sec. 4.1.

2.4 Effective medium model for bulk properties of composites

TEM, EELS, and Raman spectroscopy are critical techniques for identifying the structure of NCMCs, which can then be related to properties including tensile strength and electrical and thermal conductivity. However, it is also desirable to

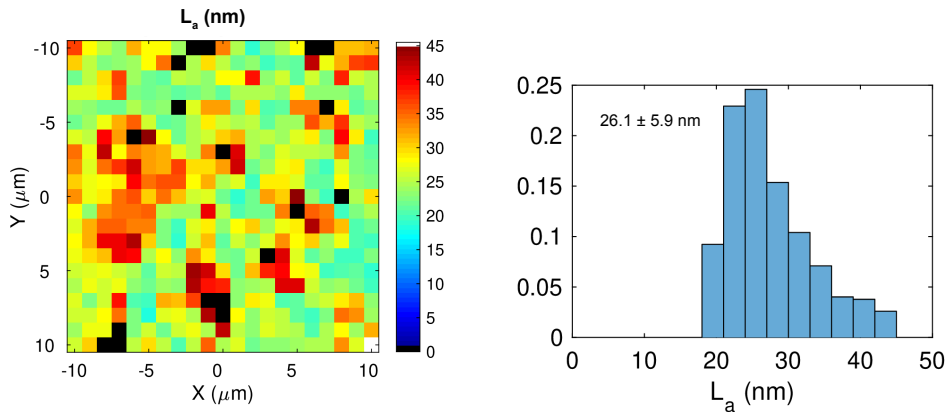


Figure 2.9: Left: Spatial distribution of the nano-graphite crystallite size L_a in a $21 \times 21\text{-}\mu\text{m}$ Raman spectrum image. Black pixels were excluded from the subsequent analysis due to poor fit quality. Right: the distribution of L_a in the spectrum image.

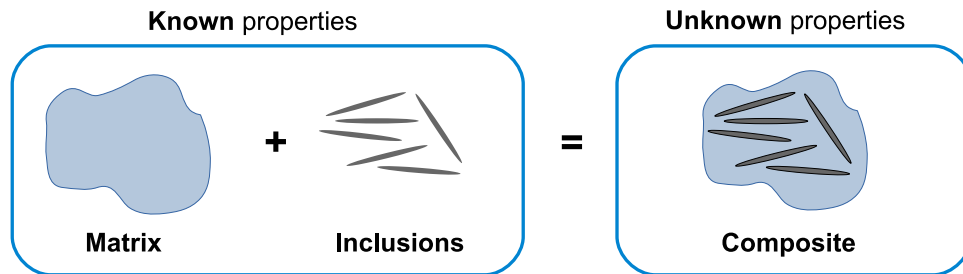


Figure 2.10: The macroscopic properties of a composite depend on many variables in addition to the bulk properties of the constituents (matrix and inclusions), for instance the inclusion orientation, dimensions, and interfacial interactions. There is no general closed-form solution to predict the properties of composites.

predict the properties of composites with certain graphitic structures in order to fully understand their potential to offer enhanced properties, and to provide a reference against which to gauge progress in their development.

The essence of this problem is illustrated by the schematic in Fig. 2.10. Various attempts have been made since the time of Maxwell to calculate the bulk properties of a composite, which is by definition locally inhomogeneous [86, 87]. Several additional variables become relevant for the properties of composites in addition to the bulk properties of the matrix and inclusions. The volume fraction of inclusions,

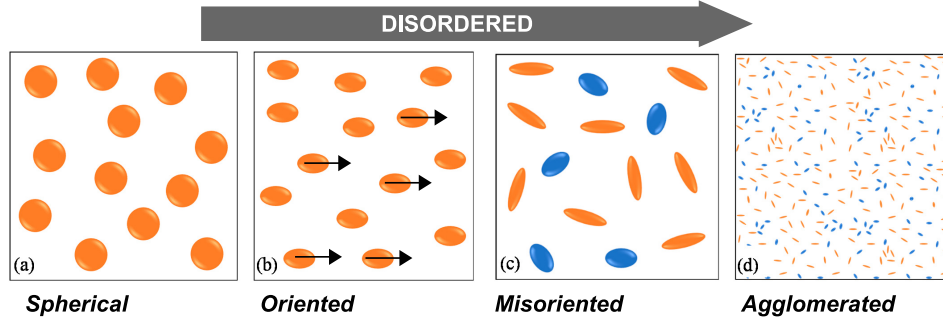


Figure 2.11: Example configurations of composite inclusions with increasing complexity. Adapted from Ref. [88].

as well as the inclusion geometry (shape and aspect ratio) and distribution within the matrix (orientation and agglomeration) are generally significant. Fig. 2.11 gives examples of the many possible configurations of inclusion geometries and distributions with varying degrees of ordering [88]. The relationship between anisotropy in the inclusions' property to be simulated and the anisotropy of their distribution within the matrix, if any, is relevant to composites which comprise graphitic inclusions, such as carbon nanotubes or graphene sheets, whose electrical and mechanical properties are highly anisotropic.

Interactions at interfaces between the matrix and inclusions can be significant, but difficult to predict theoretically. Nan and co-workers effectively modified an effective medium model for thermal conductivity to include the interfacial thermal resistance following Kapitza and Maxwell [89]. Deng [90] used this model to predict thermal conductivities of CNTs embedded in insulating media, but did not extend the interfacial-resistance calculations to electrical conductivity [91]. Fabrication of model systems and/or nanoscale characterization are desirable to understand these phenomena and to validate predictions. Finally, for certain inclusion geometries

above a critical volume fraction, the potential arises for long-range interaction (*percolation effects*) between series of adjacent inclusions. Predicting percolation effects is mathematically complex and they are often safely neglected in dilute systems [86].

Several methods to model the properties of composites fall under the umbrella of effective medium theory, or effective medium approximation (EMA), first developed by Bruggeman and Landauer [92]. Following this approach, a fraction of the matrix with a given property (for the sake of this example, the electrical conductivity σ_1) is replaced by a dilute, random dispersion of inclusions with a different property (ex. σ_2). For each inclusion it is assumed that, rather than being surrounded by some combination of matrix and other inclusions (the exact configuration of which could not be known), the inclusion is surrounded by the *effective medium* with the property σ_e of the bulk composite. Applications of the effective medium approximation to predict electrical conductivity enhancement in composites are discussed in Sec. 4.3.

Chapter 3: Characterization of wide-bandgap MOS interfaces

Recent developments in wide-bandgap semiconductor processing have enabled commercialization of silicon carbide-based devices. Nevertheless, fundamental questions remain regarding the SiC/SiO₂ interface which prevent SiC-based electronics from reaching their full potential in terms of performance and reliability. In addition, several new wide-gap semiconductor technologies such as gallium oxide have emerged within the last decade that may eventually surpass SiC in performance under very high voltage conditions as their technology matures. Various TEM investigations were conducted to gain insight into the semiconductor-insulator interface of these systems. Sec. 3.1 presents results of two experimental post-oxidation annealing treatments in SiC based devices, respectively based on B and Sb doping, while Sec. 3.2 explores the interface structure of two deposited gate oxide materials, SiO₂ and Al₂O₃ on β -Ga₂O₃ devices processed under various conditions.

3.1 SiC: Passivation of electrically active defects with chemical treatments beyond NO annealing

3.1.1 Boron interdiffusion and incorporation into SiO₂

Nitridation annealing of the SiC/SiO₂ system has dramatically improved the channel mobility and enabled the first commercially successful SiC MOS devices. Nevertheless, the resulting channel mobilities of 35–50 cm²/Vs [9, 93] fall far short of the bulk field effect mobility in SiC. Within the past 10 years, efforts have been underway to identify new chemical treatments that are able to enhance the performance and/or reliability of the SiC/SiO₂ system better than NO. Several electrical characterization experiments have identified the dopants phosphorus [14–16, 94, 95] and boron [13, 96, 97] as promising ways to passivate electrically active defects and increase the field-effect mobility, μ_{FE} . In both cases, doping is performed as a post-oxidation anneal (POA) step which converts the thermally grown SiO₂ oxide into a phosphosilicate glass (PSG) or borosilicate glass (BSG), whose structure and chemistry lower the interface trap density D_{it} and lead to enhanced μ_{FE} : up to 75–105 cm²/Vs in the case of PSG [16] and approximately 100 cm²/Vs in the case of BSG [13, 98], about 2–3 times greater than NO POA alone. Furthermore, nitridation in combination with boron incorporation into a deposited oxide layer can lead to μ_{FE} of up to 170 cm²/Vs [97].

Few structural studies have been conducted to date of the PSG and BSG oxide layers on SiC. Analytical electron microscopy is especially important to understand-

ing the mechanisms by which P and B incorporation lead to enhanced mobility, in order to optimize the potential for engineering devices with superior performance. Prior to this work, one specimen each of PSG and BSG gate oxide was studied using TEM-EELS by Joshua Taillon, a former member of the research group of Prof. Salamanca-Riba, whose results are reported in his 2016 PhD dissertation [72]. This section of the present work details the confirmation of Dr. Taillon’s TEM work on BSG-gated SiC and extends it using a larger dataset and new analytical tools. This work is collectively published in Ref. [99].

3.1.1.1 Methods

The BSG sample was prepared by collaborators in the research group of Prof. Sarit Dhar of Auburn University Department of Physics. In order to validate the previous results in Ref. [72], the sample was prepared under the same conditions. A 5 mm × 5 mm piece was diced from a 4°-miscut, *n*-type doped (10^{16} cm⁻³) 4H-SiC wafer. After standard RCA cleaning (Radio Corp. of America [100]), the SiO₂ oxide was thermally grown at 1150 °C to a target thickness of 75 nm. Subsequently, the BSG layer was formed by annealing the sample in the presence of a planar B₂O₃ diffusion source at 950 °C for 30 min., followed by a 2 hour drive-in anneal without the B₂O₃ plate at the same temperature in Ar atmosphere. Electrical measurements for this sample are detailed in Ref. [18]

Cross-sectional TEM specimens were prepared using the standard techniques described in Sec. 2.2. The sample thickness was ultimately reduced to 50–60 nm

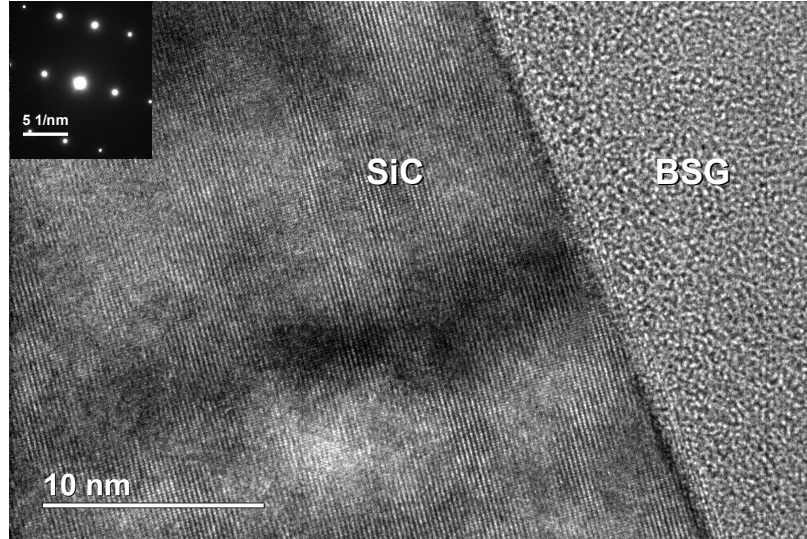


Figure 3.1: High-resolution TEM image of the SiC/BSG interface, which was abrupt and smooth except for the steps resulting from the 4° substrate miscut.

using a 2 keV Ga^+ ion beam in order to minimize the depth of amorphization damage. High-resolution TEM imaging, HAADF-STEM, and EELS were performed to characterize the structural and chemical composition of the SiC/BSG interface. Analysis of the EELS data was performed by non-negative matrix factorization (NMF). For this work the analysis was also performed using multivariate curve resolution by log-likelihood maximization (MCR-LLM), a subclass of NMF that is better suited to weak and/or low signal-to-noise ratio data by applying additional constraints [74].

3.1.1.2 Results and discussion

High resolution TEM imaging revealed a flat and abrupt interface similar in quality to those produced by the established NO anneal, as shown in Fig. 3.1. The

interface was abrupt, the only roughness being atomic steps arising from the 4° miscut of the wafer.

HAADF imaging and EELS mapping were also performed in STEM mode to probe the elemental composition and bonding of the interfacial region. Two physically significant components were identified for the NMF decomposition. These results are presented in Fig. 3.2 for a 23 nm × 50 nm region along the interface. The first component, called silicon background in Fig. 3.2, was stronger in the SiC substrate (left side of the map) but also weakly present in the BSG layer. It can be attributed to background signal from the extended fine structure of the Si- L_1 EELS edge. The spectrum of this component is shown in blue in Fig. 3.2(a). The second component (green) matches the shape and energy of the B- K EELS edge and thus confirms the presence of boron within the BSG layer. The corresponding intensity map (“Boron,” top center) shows how the boron is homogeneously distributed throughout the bulk of the BSG layer, and concentrated in a narrow band at the interface.

Linear profiles of relative intensity as a function of position across and perpendicular to the interface were constructed by summing each intensity map in the vertical axis (parallel to the interface) and normalized relative to its maximum (Fig. 3.2(b)). The B- K signal exhibits a maximum about 1 nm away from the interface, as it is defined by the inflection point of the Si- L signal. At its maximum the B- K signal is 2 times its intensity in the bulk of the BSG layer. The width (FWHM) of the interfacial B accumulation was 2.8 ± 0.4 nm, with the uncertainty

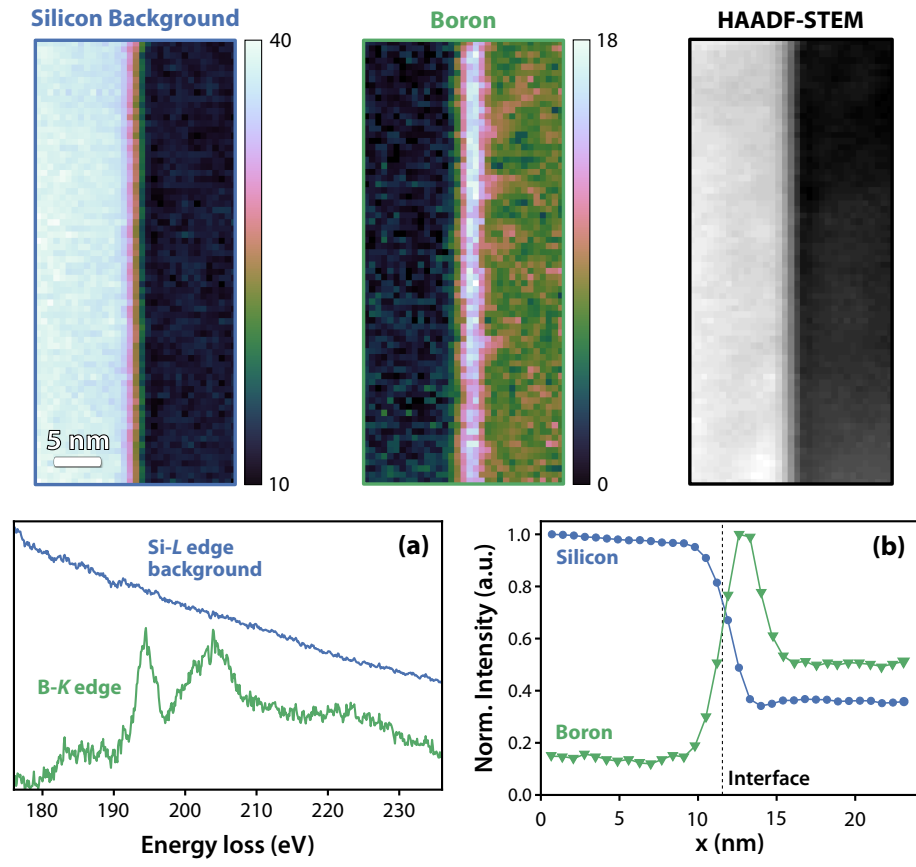


Figure 3.2: Relative EELS intensity maps and simultaneously collected HAADF-STEM image of the SiC/BSG interface (top). The HAADF-STEM image shows a ≈ 2.1 -nm wide dark band at the interface, most visible at the bottom of the image, which corresponds to a lower- Z element such as B. Intensity maps reflect the relative abundance of the two components identified by NMF decomposition, shown in (a): the residual background from the Si- L edge, and the B- K edge. (b) Normalized line profiles of each component's intensity as a function of displacement across the interface. The B- K signal has a well-defined peak at the interface, with a width (FWHM) of 2.8 nm and peak B concentration roughly twice that of the bulk BSG.

estimated to be half the step size of the EEL spectrum image, equal to the STEM probe size of 0.7 nm.

As shown in Fig. 3.2(a), the primary peak of the B-*K* edge has an energy of 193.8 ± 0.7 eV, which corresponds to the π^* antibonding orbital of boron in an sp^2 -hybridized state such as in B_2O_3 or trigonally-coordinated BO_3 units [101–103]. Uncertainty in the edge-onset energy was estimated as the standard deviation of 7 B-*K* edge positions extracted from NMF decompositions of EELS maps from different areas along the interface. The evidence of trigonally-coordinated boron provided by EELS lends support to the predicted mechanism of D_{it} reduction in B-doped SiC, which suggests that the relief of interfacial stress is the cause [13, 98]. The presence of B in the glassy SiO_2 layer contributes to a higher concentration of non-bonding O atoms, making the BSG layer—and the interfacial part of it in particular—more fluid [104], and less prone to large interfacial stresses that give rise to electrically active defects. Elemental B did not appear to be present, as its B-*K* edge shape is much different than that for B_2O_3 [103]. This observation is consistent with the O-*K* EELS edge profile (Fig. 3.3) across the interface, which indicated that the stoichiometry of oxygen within the oxide layer was uniform with depth, in spite of the peak in B-*K* intensity profile.

The presence of the weak, but well-defined B-*K* edge and its uniform distribution along the interface meant that this dataset was well suited to additional MSA algorithms beyond NMF, both to confirm the results produced by NMF and to identify promising algorithms for use with other material systems elsewhere in this thesis. Multivariate curve resolution by log-likelihood maximization (MCR-LLM)

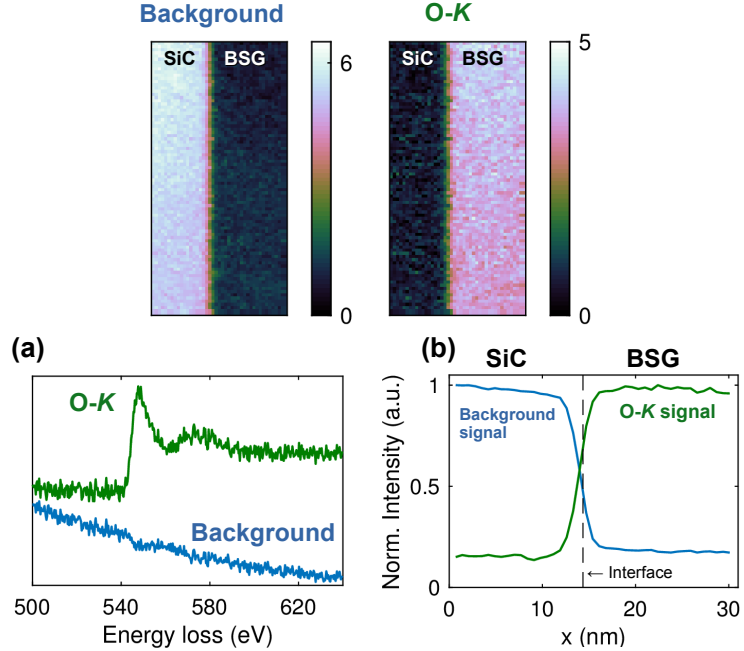


Figure 3.3: STEM-EELS spectrum imaging at the energy-loss range of the O- K edge from the SiC/BSG interface, near the region shown in Fig. 3.2. (a) A well-defined O- K edge component was identified by NMF and localized to the gate oxide (BSG) layer. (b) The line profile of O- K intensity did not indicate an interfacial peak of O concentration, unlike with B.

is one such algorithm first published in 2019 [74] and introduced in Sec. 2.1.2.2. It is particularly well-suited to low signal-to-noise ratio datasets. The MCR-LLM decomposition results of the BSG sample are presented in Fig. 3.4. No background subtraction was performed prior to decomposition. The 2 spatial dimensions of the spectrum image were reduced to 1 prior to the analysis by summing each column parallel to the interface, as required by the MCR-LLM Python code (available from the repository indicated in Ref. [74]).

Three significant components were identified by MCR-LLM, as shown in Fig. 3.4(b). This is one more component than NMF was able to clearly resolve, as in Fig. 3.2. The difference appears to arise from the additional constraints applied by MCR-LLM. Specifically, the requirement that relative intensities (termed “abun-

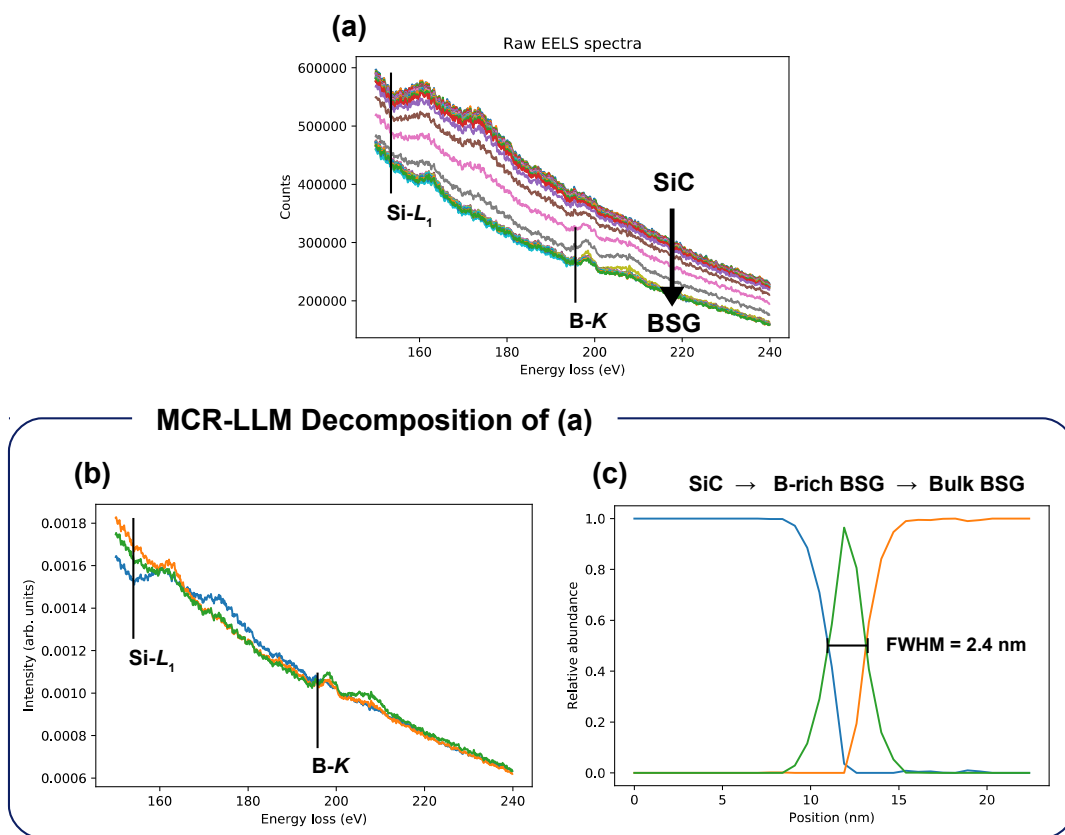


Figure 3.4: (a) Raw EELS data in the range 150–240 eV, from the same spectrum image analyzed in Fig. 3.2. Each spectrum is one 50-nm long \times 0.7-nm wide line scan running parallel to the interface. The spectra are separated by their raw intensities such that the progression from SiC across the interface to BSG can be seen, as marked by the thick arrow. (b) MCR-LLM components for each of 3 phases identified and (c) corresponding abundance profiles. The interfacial phase (green curve) in (c) displayed the most prominent B-K edge in (b), followed by the BSG phase (orange). The SiC phase (blue) of the decomposition contained no discernible B-K signal.

dances” for the purpose of this algorithm) always sum to one led to the separation of the BSG signal into two phases, one interfacial and one bulk, on the basis that the B-*K* edge was stronger at the interface. Despite making this distinction, MCR-LLM did not suggest that there was a chemical difference between the interface and bulk BSG components, as they both exhibited the same fine-structure, albeit with different intensities (Fig. 3.4(b)).

It is important to note that MCR-LLM has different criteria for distinguishing between phases as a result of its constraints. The requirement for closure in particular seems to create a tendency to resolve intensity differences into distinct phases, in addition to distinguishing between chemical differences in the EELS fine structure, whereas NMF relies more exclusively on the shape of the fine structure. Aside from this distinction in the two algorithms’ approaches, the results of NMF and MCR-LLM decomposition are qualitatively similar. For instance, the width of the interfacial boron pile-up in MCR-LLM was 2.4 nm, compared to 2.8 nm for NMF; these values are within the margin of error, estimated to be 0.4 nm. These results show that MCR-LLM is a viable way to apply multivariate statistical techniques to EELS data, and support the qualitative results of NMF.

In summary, the SiC/BSG MOS interface was analyzed using analytical TEM-EELS in combination with multivariate statistical analysis techniques in order to validate and expand on previous findings, which indicated a uniform band of B-rich SiO₂ located at the interface. The present work supports that conclusion with considerably more data. NMF decomposition reveals a 2.8-nm wide band of boron accumulated at the interface, roughly twice the intensity as in the bulk oxide layer.

The fine structure of the B-*K* edge indicates sp^2 hybridization, which is expected to relieve interfacial stresses in the device and therefore presents a plausible mechanism for the reduction in D_{it} observed in B-doped SiC MOS devices.

3.1.2 Sb ion implantation in conjunction with NO annealing

Another technique to improve channel mobility in SiC MOS devices is to implant ions directly into the substrate prior to the formation of the gate oxide layer. This approach has been utilized to help elucidate the mechanisms by which NO and PSG annealing improve channel mobility. By implanting antimony ions into the surface channel (Sb counter-doping), the effects of n-type doping could be distinguished from the passivation of interface traps. N, P, and Sb are all n-type dopants in SiC, but Sb was not expected to have a passivating effect due to its large atomic size [17]. The use of Sb counter-doping in conjunction with previously demonstrated passivating treatments suggest that the effects are additive, with each treatment acting independently to improve mobility. This has been the case with Sb+NO (peak $\mu_{FE} = 110 \text{ cm}^2/\text{Vs}$, compared with $32 \text{ cm}^2/\text{Vs}$ for NO and $80 \text{ cm}^2/\text{Vs}$ for Sb alone) [17] and BSG+NO (peak $\mu_{FE} = 180 \text{ cm}^2/\text{Vs}$ vs. $135 \text{ cm}^2/\text{Vs}$ for BSG alone) [18].

The interface structure of Sb counter-doped SiC MOS systems have primarily been probed by electrical methods [105] or composition-analysis techniques with resolution limitations, such as secondary ion mass spectrometry (SIMS) [18]. As such, even preliminary results from TEM and EELS will be of interest to the SiC

device community. This subsection presents a case-study of TEM-EELS investigations performed on one sample subjected to the Sb+NO process by collaborators at Auburn University as described in Ref. [18]. In brief, a 5 mm \times 5 mm piece of a 4° off-axis, p-type ($\approx 10^{16}$ cm $^{-3}$) 4H-SiC wafer was implanted with a dose of 2.5×10^{13} cm $^{-2}$ Sb ions at an energy of 80 keV. After a 1650 °C post-implantation activation anneal, the gate oxide layer was thermally grown to a target thickness of 75 nm and an NO post-oxidation anneal was performed for 30 min. The cross-sectional TEM specimen was prepared by FIB using the approach presented in Sec. 2.2 and ultimately thinned to a thickness of ≈ 50 nm using a 2 keV Ga $^{+}$ beam.

TEM-EELS results from the cross-sectional TEM lamella are presented in this section. High-resolution imaging of the interface region (Fig. 3.5) does not suggest any significant deviation from a device prepared with only the NO anneal. The interface was abrupt and smooth, with few steps, mostly corresponding to the substrate miscut.

The objectives of STEM-EELS spectrum imaging of this sample was to determine whether the Sb could be detected and if so, to observe how it was spatially distributed in the device. Contamination and drift were particular challenges during spectrum imaging of this sample. Performing a “beam shower” [63] and allowing the specimen position to stabilize over a few minutes prior to STEM imaging and EELS helped to mitigate these problems. 6 spectrum images were collected to encompass the Si-*L*, C-*K*, Sb-*M*_{4,5}, and O-*K* edges, using a probe step size of 0.7 nm and an energy channel width of 0.3 eV.

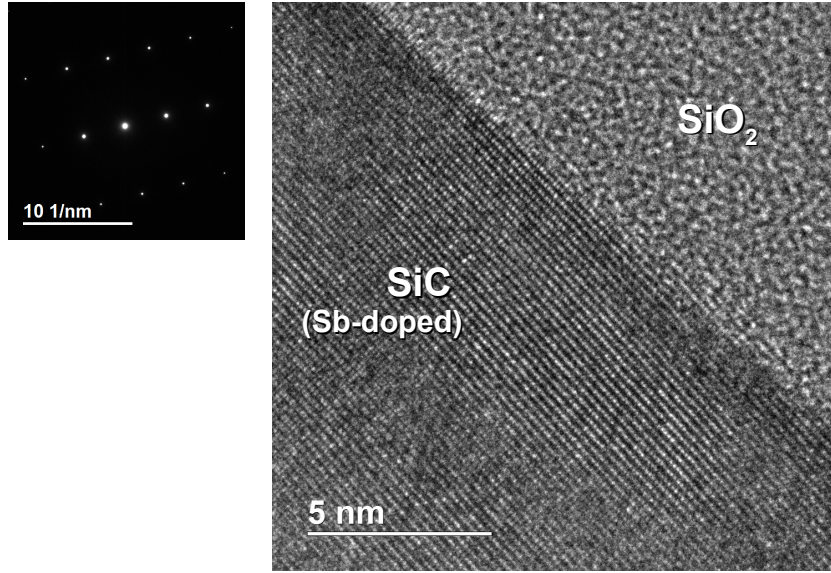


Figure 3.5: High-resolution TEM image and associated diffraction pattern of the Sb-doped SiC/SiO₂ interface.

There is an indication that the SiC/SiO₂ transition region was narrower after the Sb+NO treatment than in a comparable device treated only with NO. Fig. 3.6(a) shows the progression of the chemical shift of the Si- $L_{2,3}$ edge from 99 eV in SiC to \approx 105 eV in SiO₂, as the STEM probe moved across the interface. This shift occurred within 5 ± 1 adjacent spectra, so the transition width w_{TL} was therefore $0.7 \text{ nm} \times (5 \pm 1) = 3.5 \pm 0.7 \text{ nm}$. This is smaller than transition widths previously reported for NO annealing alone, where a 30-minute post-oxidation anneal process led to a w_{TL} of about $7 \pm 1 \text{ nm}$ [93]. Sb ion implantation does not, however, appear to have affected the Si- $L_{2,3}$ edge in SiC, which is not distinguishable from that in an un-doped SiC substrate (Fig. 3.6(b)) from a device treated with NO only.

Higher-energy signals were also collected using longer dwell times. The energy range around the Sb- $M_{4,5}$ edge at 528 eV and the O- K edge at 532 eV were of par-

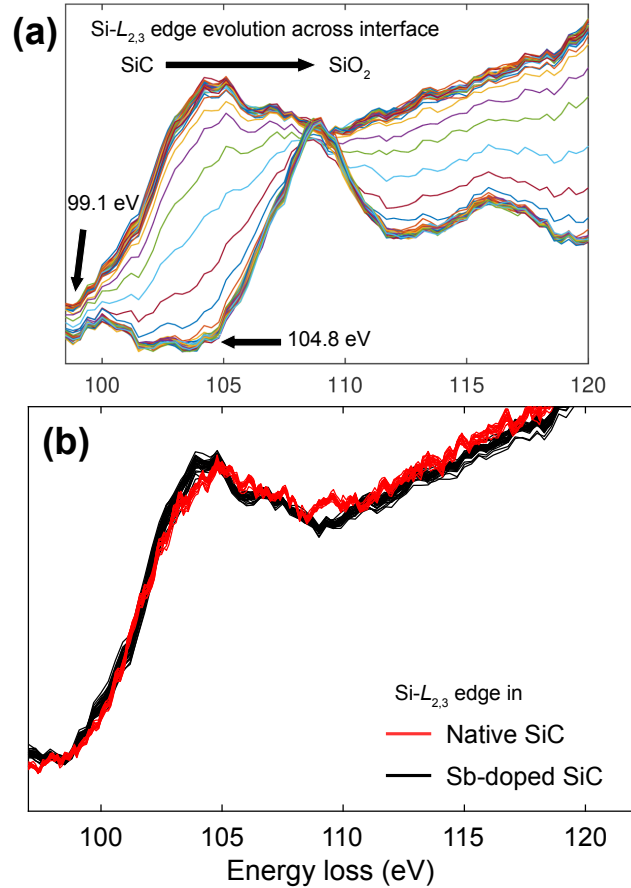


Figure 3.6: (a) Si- $L_{2,3}$ EELS edge evolution after Sb+NO annealing. Each curve represents the sum parallel to the interface of one 60-nm long column in the spectrum image array. The edge onset energy shifts from 99 eV in SiC to ≈ 105 eV in SiO₂ across 4–6 steps with intermediate onset energies, indicating that the transition width was about 3.5 nm. This is narrower than the equivalent process utilizing NO annealing only. (b) No shift in the Si- $L_{2,3}$ onset energy was identified between the Sb-implanted SiC in this sample and a reference SiC wafer from the NO-only process without ion implantation.

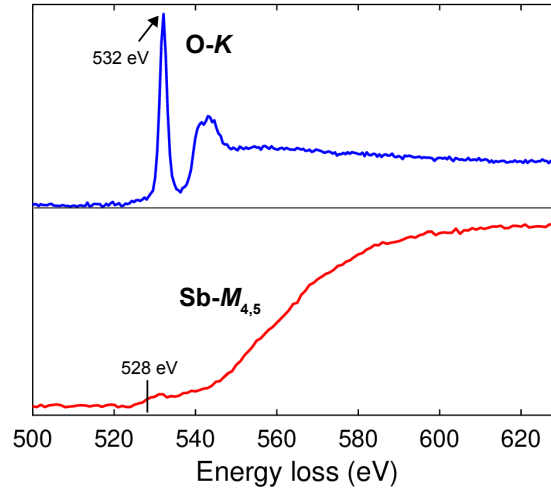


Figure 3.7: Normalized reference spectra for elemental O- K and Sb- $M_{4,5}$ edges. Source: Gatan, Inc. / eels.info

ticular interest. These edges exhibit different fine structures (Fig. 3.7) and it should in principle be possible to distinguish the two by multivariate analysis methods. The NMF algorithm was able to resolve clear C- K and O- K edges in SiC and SiO₂, respectively, as with similar devices not doped with Sb. However, NMF was not able to identify a clear Sb EELS signal. This was most likely due to a combination of the lack of an abrupt onset or well-defined peak in the Sb- $M_{4,5}$ edge, and the relatively low concentration of Sb dopants (nominally $2.5 \times 10^{13} \text{ cm}^{-2}$, but with up to 85% of the Sb being lost during the fabrication process [17, 18]). The 2019 publication and release of the MCR-LLM algorithm [74] provided a new analytical tool to search for this signal. The 2D spectrum image was converted into a 1D line-scan with one spectrum for each column of the original dataset prior to being resolved into 2 principal components by the MCR-LLM algorithm, one for Sb-doped SiC and one for the SiO₂ oxide. These components are shown in Fig. 3.8(a). The corresponding

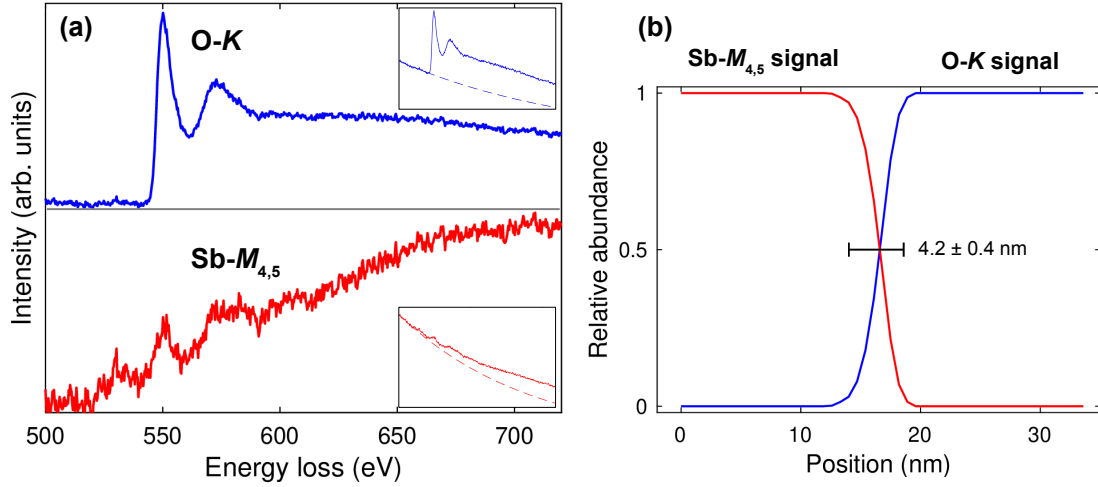


Figure 3.8: MCR-LLM decomposition of EELS spectrum image in the energy range capturing the O- K and Sb- $M_{4,5}$ edges. (a) The two principal components resolved by the MCR-LLM algorithm corresponded to the O- K (blue) and Sb- $M_{4,5}$ (red) edges. The fine structures match the published references in Fig. 3.7 after decaying-exponential background subtraction from the raw components (as displayed in the insets with the same energy-loss range). (b) Relative abundance profile of the two components across the SiC/SiO₂ interface, with a 5–95% intensity transition width of 4.2 ± 0.4 nm.

line-profile transition width in Fig. 3.8(b) between the Sb- $M_{4,5}$ and O- K edges was 4.2 ± 0.4 nm, which is within the range estimated using the Si- $L_{2,3}$ edge. MCR-LLM is not capable of identifying absolute intensities, however the more prominent noise in the Sb signal indicates that it is probably much weaker than the simultaneously collected O signal.

The results from a single device do not represent the complete picture of the interface structure, composition and bonding changes that result from the Sb+NO processing technique. Nevertheless, the TEM-EELS analysis presented in this work illustrates a promising path forward. HRTEM and spectrum imaging of the Si- $L_{2,3}$ EELS edge indicate that the interface is at least as abrupt and smooth as in comparable devices treated with an NO post-oxidation anneal only, and possibly with

a smaller w_{TL} . Higher-energy spectrum imaging interpreted using the MCR-LLM multivariate statistical method indicates that Sb is present throughout the substrate at relatively low concentrations. Previously reported SIMS depth profiles of Sb concentrations in a similarly prepared device suggest that the Sb accumulates in a Gaussian intensity profile which peaks ≈ 10 nm below the SiC/SiO₂ interface [17]. The presence of this feature could not be confirmed by the MCR-LLM decomposition due to the absence of a third EELS edge, for instance Si-*L* or C-*K*, that could serve as a reference to show intensity variations of the Sb signal with depth into the substrate. A deeper EELS line profile over a sufficiently wide energy range to capture an EELS edge unique to the substrate would help to confirm this report.

3.1.3 Summary and future research directions

In this section, new methods to improve the performance and reliability of SiC MOS devices have been explored. Although SiC is now a commercially available technology, its performance still falls short of the theoretically expected mobilities, largely due to electrically active interfacial defects at the substrate/gate oxide interface which are traditionally passivated using a NO post-oxidation anneal. Experimental treatments based on boron and antimony doping each serve to increase channel mobility in SiC devices through different mechanisms. In Sec. 3.1.1, HAADF-STEM and EELS spectrum imaging are used to confirm the link between the spatial distribution of B in the B-doped SiO₂ layer, the sp^2 -hybridized nature of the chemical bonding and the relaxation of interfacial stress known to inhibit car-

rier mobility. The B - K spectrum image also presented an opportunity to validate the recently published MCR-LLM multivariate analysis algorithm for wide-bandgap heterostructures. This technique became relevant for Sec. 3.1.2, where it was used to identify a weak Sb- $M_{4,5}$ EELS edge that could not be found with NMF. The relatively smaller w_{TL} in this device and overall abrupt, stable structure is also cause for encouragement regarding Sb counter-doping as a method to improve channel mobility.

Novel SiC processing techniques are often only characterized by electrical methods, with an eye towards processing-performance relationships. Analytical electron microscopy techniques provide the physical and chemical structure information to build a complete picture of the processing-structure-property relationships in SiC MOS devices, which will ultimately inform the design of more efficient and robust devices.

3.2 Ga₂O₃ with deposited SiO₂ and Al₂O₃ gate oxides

3.2.1 Post-deposition annealing effects on the Ga₂O₃/gate oxide interface structure

As described in Sec. 1.1.2, gallium oxide-based MOS technology is not yet mature. One of the principal challenges is the selection of appropriate gate oxide material and growth parameters to produce a device with a suitable interface structure to obtain the desired electrical properties. This section describes a series of comparative TEM investigations conducted to investigate the Ga₂O₃ interface with

deposited SiO_2 and Al_2O_3 gate oxides, with the goal of developing structure-based understanding of electrical behavior previously observed on the same set of samples by Jayawardena et al. [23].

3.2.1.1 Experimental methods

A set of six samples were provided for this work by collaborators in the research group of Prof. Sarit Dhar at Auburn University. A summary of the sample preparation conditions is presented in Table 3.1. Ga_2O_3 MOS capacitors were prepared by chemical vapor deposition (CVD) of the gate oxide layer on unintentionally Si-doped, $(\bar{2}01)$ -oriented $\beta\text{-Ga}_2\text{O}_3$ substrates obtained from Tamura Corporation [106]. The substrate surfaces were treated with a chemical-mechanical polishing (CMP) process during manufacture, leading to initial surface roughness of 0.21 nm as-received [23]. After 5 mm \times 5 mm pieces were diced from the wafer and cleaned, a Piranha etch step was performed for 15 min. (1:1 $\text{H}_2\text{SO}_4\text{:H}_2\text{O}_2$).

The SiO_2 layer was deposited on one sample by low pressure CVD (LPCVD) at 650 °C for 35 min., followed by densification in N_2 at 850 °C for 2 h. For the second SiO_2 gate, a low-temperature oxide (“LTO”) was grown by CVD at 400 °C followed by annealing in Ar at 1000 °C for 60 sec. Four Al_2O_3 gate oxide samples were prepared by atomic layer deposition (ALD) at 250 °C using a trimethylaluminum (TMA) precursor gas. Two of the samples were later annealed at 500 °C, one in forming gas (FG; 95% N_2 : 5% H_2) and one in pure H_2 . The others were not subjected to post-deposition annealing (PDA). Al gate contact pads were thermally

Sample #	Process	Material	Dep. T ($^{\circ}\text{C}$)	PDA T ($^{\circ}\text{C}$)	PDA Time
531	LPCVD	SiO_2	650	850	2 hrs.
324	LTO	SiO_2	400	1000	60 sec.
454	ALD	Al_2O_3	250	–	–
24	ALD	Al_2O_3	250	–	–
25	ALD	Al_2O_3	250	500 (in FG)	2 min.
26	ALD	Al_2O_3	250	500 (in H_2)	2 min.

Table 3.1: Gate-oxide materials and CVD deposition parameters of the studied Ga_2O_3 MOS devices. FG = Forming Gas (mixture of N_2 and H_2).

evaporated on to the devices in order to perform electrical characterization prior to TEM; the details of these measurements are published in Ref. [23].

Cross-sectional TEM specimens were prepared by focused ion beam using the techniques described in Sec. 2.2. Lamellas were cut parallel to the cleaved edges of the $(\bar{2}01)$ -oriented Ga_2O_3 wafers, i.e. $[010]$ or $[102]$, such that the TEM zone axis was ultimately one of these two directions. Final FIB polishing used a 2 kV Ga^+ beam to reduce the thickness of FIB-related damage (amorphization and Ga^+ ion implantation) and resulted in lamellas ranging between 50–100 nm in overall thickness. High-resolution (HR) TEM imaging, high angle annular dark field scanning TEM (HAADF-STEM) and electron energy loss spectroscopy (EELS) were performed on the JEOL JEM 2100F TEM/STEM located at the University of Maryland Advanced Imaging and Microscopy Laboratory (AIMLab). EELS data were collected at 200 kV in STEM mode as spectrum images (SIs) with a probe size of 0.7 nm, convergence semi-angle of 12 mrad and collection semi-angle of 57 mrad. Typical SI dimensions were 30–60 nm wide (across the interface) and 30–60 nm long (parallel

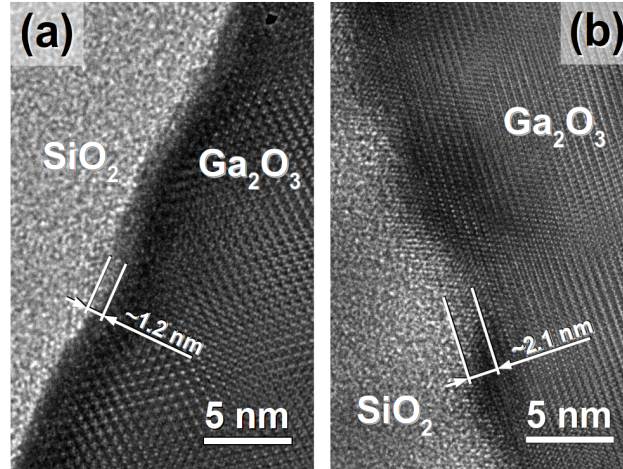


Figure 3.9: HRTEM images from Ga_2O_3 MOS capacitors subjected to post-deposition annealing (PDA) at different process temperatures. (a) The sample treated with $850\text{ }^\circ\text{C}$ PDA exhibited localized peak-to-valley roughness of about 1 nm, while the sample treated with $1000\text{ }^\circ\text{C}$ PDA showed roughness of 2–3 nm.

to the interface). Several SIs were collected at different locations along the interface of each specimen to increase the accuracy of the results.

3.2.1.2 Results and discussion

SiO_2 gate oxides

Interfacial roughening of $\text{Ga}_2\text{O}_3/\text{SiO}_2$ correlated with PDA temperature

High-resolution TEM imaging was performed first to identify the structural characteristics of the $\text{Ga}_2\text{O}_3/\text{SiO}_2$ interfaces. SiO_2 layers were amorphous, as is typical for the LPCVD and LTO processes. Localized roughness was observed along the interfaces of both devices with SiO_2 gates (Samples #531 and 324) as shown in Fig. 3.9. The peak-to-valley roughness amplitude was approximately 1 nm in the sample exposed to an $850\text{ }^\circ\text{C}$, 2-hour post-deposition anneal (PDA), and 2–3 nm in the sample exposed to a $1000\text{ }^\circ\text{C}$, 60-second PDA. The larger interfacial roughness

may be attributed to the higher PDA temperature, since both Ga_2O_3 substrates were treated by the same chemical-mechanical polishing process during manufacture, leading to surface roughness values of 0.21 nm before gate oxide deposition [23,107]. It has been previously shown that the RMS surface roughness of a (100)-oriented β - Ga_2O_3 substrate increases after annealing, from 0.2 nm on the as-received substrate, to 2.67 nm after a 950 °C, 3-min. anneal, to greater than 14 nm after 3 min. at 1100 °C [108].

The roughness of gate oxides is closely linked with the performance and reliability of semiconductor devices. In the ubiquitous Si/SiO₂ system, roughness on the order of 2 nm is known to develop during the standard growth of SiO₂ at 900 °C, which leads to undesirable electrical properties (reduced breakdown field and increased probability of failure for a given bias); both the roughness and poor reliability were ameliorated by post-oxidation annealing at 1050 °C [109]. Extreme surface roughness on the order of several (4–9) nm has been found to increase tunneling current, to the detriment of the gate oxide reliability [110]. With thermally grown SiO₂ on SiC, roughness is detrimental to the charge-to-breakdown metric (Q_{BD}) in time-dependent dielectric breakdown (TDDB) measurements, as increased roughness can contribute to more intensive local field stress in the gate oxide, leading to increased risk of failure over time [111]. For these reasons it is desirable to minimize roughness or large thickness variations in gate oxides of Ga_2O_3 MOS devices as well.

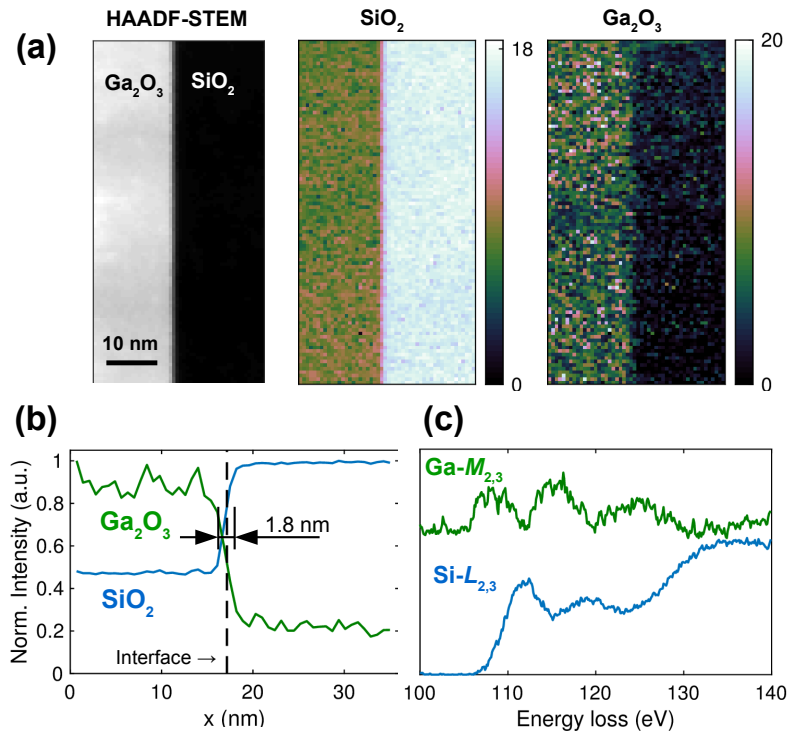


Figure 3.10: EELS principal components from a Ga₂O₃/SiO₂ MOS capacitor treated with 1000 °C PDA. (a) Relative intensities of the HAADF-STEM (Z-contrast) signal and the two principal components belonging to SiO₂ and Ga₂O₃, respectively. (b) Line-profile averages showing the change in relative intensities across the interface, which was abrupt, with minimal roughness in this region. (c) Constituent NMF component spectra corresponding to the maps in (a).

Electron energy loss spectroscopy of Ga₂O₃/SiO₂ interfaces

Scanning TEM and EEL spectrum imaging were performed in the energy range of the Si-*L*_{2,3} and Ga-*M*_{2,3} edges in order to study the chemical composition and bonding features of the interface. The onset energies of the two edges differed by only 2 eV, which can be resolved by the spectrometer, but severe overlap between the edges' extended fine structure made it difficult to separate them using traditional methods. In addition, EELS edges can exhibit a chemical shift of up to several eV depending on the bonding state, as with the elemental Si *L*_{2,3} edge (99 eV in pure Si)

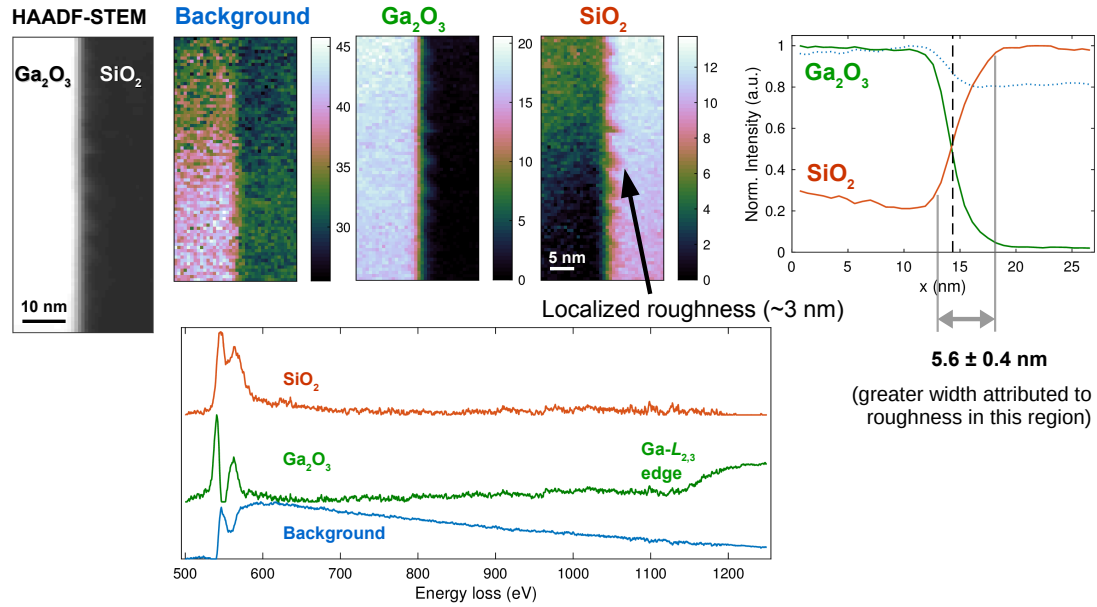


Figure 3.11: O-K EELS map from Sample #324 showing roughness of Ga₂O₃/SiO₂ interface following 1000 °C PDA. The roughness amplitude of approximately 3 nm is visible in the HAADF-STEM signal (periodic bright bands) as well as the Ga and Si EELS component maps.

vs. Si in SiO₂ (105 eV). The NMF algorithm made it possible to distinguish these components. Two principal components were sufficient to fully describe the core-loss spectrum image in Fig. 3.10, corresponding to the sample treated by 1000 °C PDA. In this region the interface showed minimal roughness (Fig. 3.10(b)) and was 1.8 ± 0.4 nm wide. Inspection of another SI from a different area along the same interface shown in Fig. 3.11 revealed similar roughness features as shown in the HRTEM image, with an amplitude of about 3 nm.

Al₂O₃ gate oxides

Crystallization of the Al₂O₃ gate layer under the electron beam

During HRTEM imaging of the devices with amorphous, ALD-grown Al₂O₃ gate oxides, it became apparent that the gate layer crystallizes under the electron beam in TEM. Two HRTEM images of one Ga₂O₃/Al₂O₃ interface (Sample #454) are shown in Fig. 3.12. The first (Fig. 3.12(a)), taken after only a few seconds of TEM beam exposure, shows a 1.5 nm crystalline layer adjacent to the substrate. After additional exposure on the order of tens of seconds, the crystalline region had propagated outward from the interface, and the Al₂O₃ film had fully crystallized under the beam (Fig. 3.12(b)). This crystallization phenomenon was confirmed multiple times by watching the Fast Fourier Transform signal of the Al₂O₃ film (Fig. 3.12, upper-right insets) evolve from amorphous halo rings to crystalline spots at different points along the TEM specimen, as well as by the HRTEM and electron diffraction imaging of the fully crystallized film. In total, of the three Ga₂O₃/Al₂O₃ samples studied in this work, all exhibited a qualitatively similar crystallization effect, including the sample that was annealed at 500 °C—meaning that the annealing did not by itself cause crystallization.

Since crystallization proceeded quickly to completion in under 60 seconds, it was not immediately apparent whether the initial image in Fig. 3.12a is representative of the sample as fabricated, or simply showing the initial stages of crystallization under the electron beam used to image the sample. The observation of a narrow

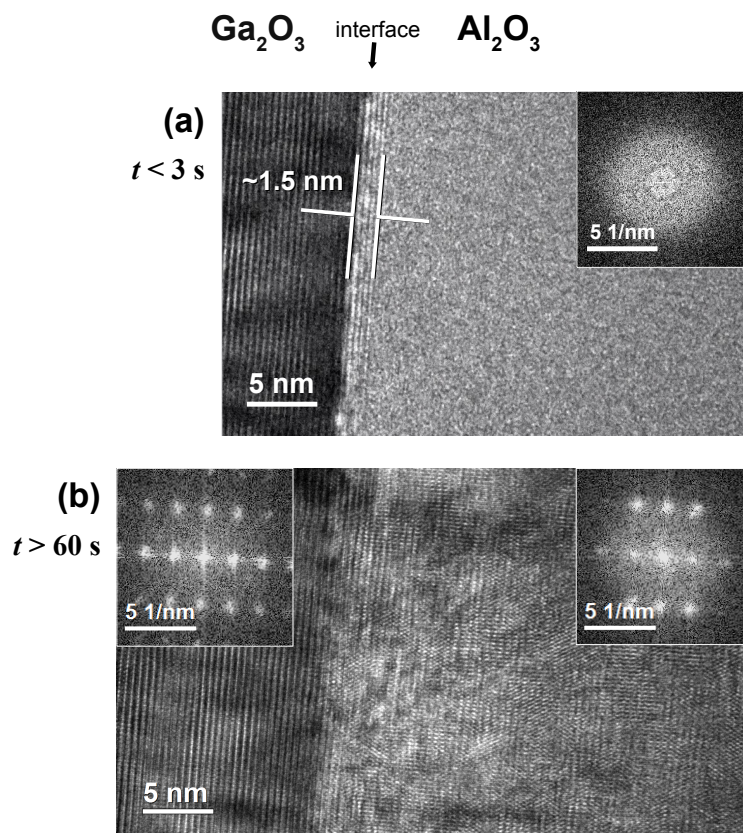


Figure 3.12: HRTEM images of the $\text{Ga}_2\text{O}_3/\text{Al}_2\text{O}_3$ interface. (a) After minimal electron beam exposure of a few seconds, a 1.5 nm-wide crystalline layer of Al_2O_3 was visible at the interface between the substrate and amorphous Al_2O_3 . Inset: Fast Fourier Transform (FFT) of Al_2O_3 layer in the region displayed. The absence of spots or rings in the pattern is indicative of the layer's amorphous character. (b) Further tens of seconds' exposure led to the complete crystallization of the Al_2O_3 layer in the region under the beam. Inset, right: Discrete spots in the FFT of Al_2O_3 demonstrate the formation of a complete crystalline layer in the region shown. Inset, left: FFT corresponding to the $[102]$ zone axis of the Ga_2O_3 substrate.

band of crystalline Al_2O_3 is similar to that observed by Kamimura et al. on (010)-, but not ($\bar{2}01$)-oriented Ga_2O_3 substrates [112]. In that work, no crystallization due to TEM electron-beam exposure was reported for any sample or imaging conditions, suggesting that the influence of the electron beam was greater in this work and that the initial crystallization shown in Fig. 3.12a was caused by the beam. Quantitative investigation of this crystallization phenomenon is discussed in Sec. 3.2.2.

Interdiffusion between Ga and Al

Several EEL spectrum images were collected in STEM mode from another $\text{Ga}_2\text{O}_3/\text{Al}_2\text{O}_3$ sample (#24) prepared under the same conditions. Multivariate statistical analysis (MSA) of EELS data was performed using the NMF and MCR-LLM algorithms as detailed in Sec. 2.1.2.2. NMF decomposition of one spectrum image in the range of the Al- $L_{2,3}$ and Ga- $M_{2,3}$ edges is presented in Fig. 3.13. Two NMF components were sufficient to fully describe the data, as with the $\text{Ga}_2\text{O}_3/\text{SiO}_2$ interface. However, unlike the systems containing SiO_2 , which exhibited somewhat abrupt transitions at the interface, the relative intensity of the Ga signal declined gradually with distance up to 3.2 nm into the Al_2O_3 layer. Such a profile indicates some interdiffusion between Ga and Al, most likely occurring during the ALD process. Similar interdiffusion has been reported in metal-organic CVD-grown GaN films on sapphire substrates [113] as well as with pulsed-laser deposited (PLD) $\beta\text{-Ga}_2\text{O}_3$ films on sapphire substrates above 600 °C [114]. The region of Ga interdiffusion was significantly wider on the device that was subjected to a 500 °C, 2-min. post-

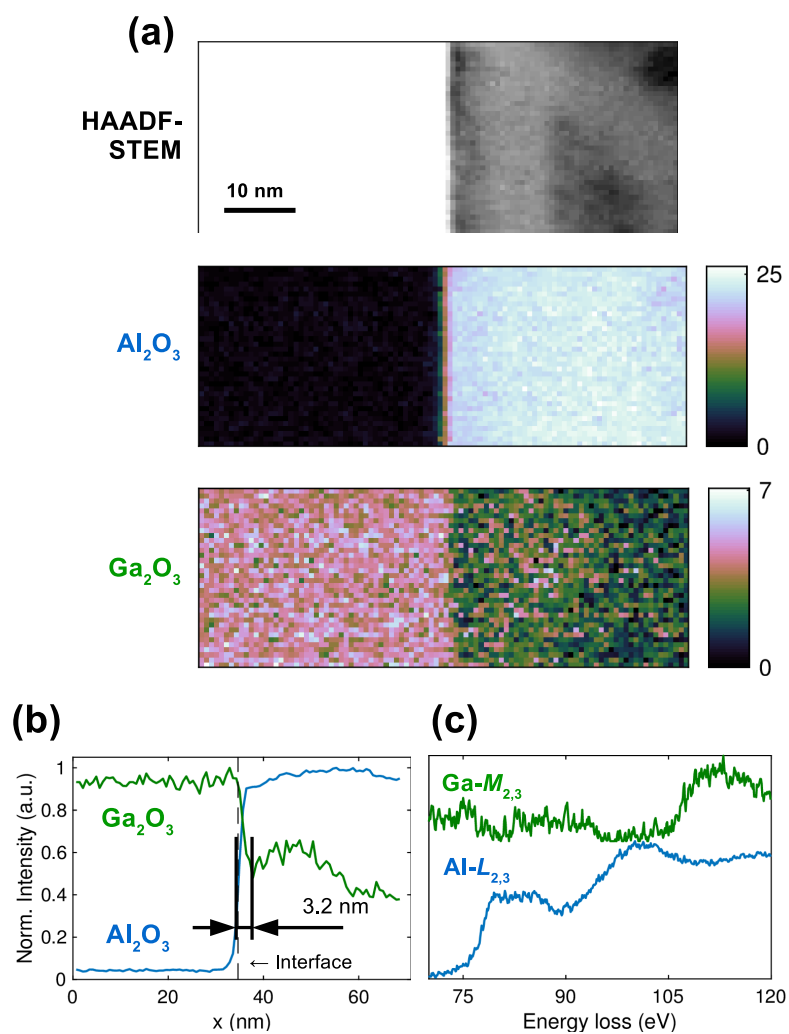


Figure 3.13: Decomposition of the core-loss EELS spectrum image from a Ga₂O₃/Al₂O₃ MOS device without post-deposition anneal (PDA). (a) From top to bottom: Relative intensities of the enhanced STEM (Z-contrast) signal, Al₂O₃ and Ga₂O₃ NMF components, respectively. (b) Line-profile averages showing the gradual decrease in Ga intensity across the interface. (c) NMF component spectra corresponding to the elemental maps in (a).

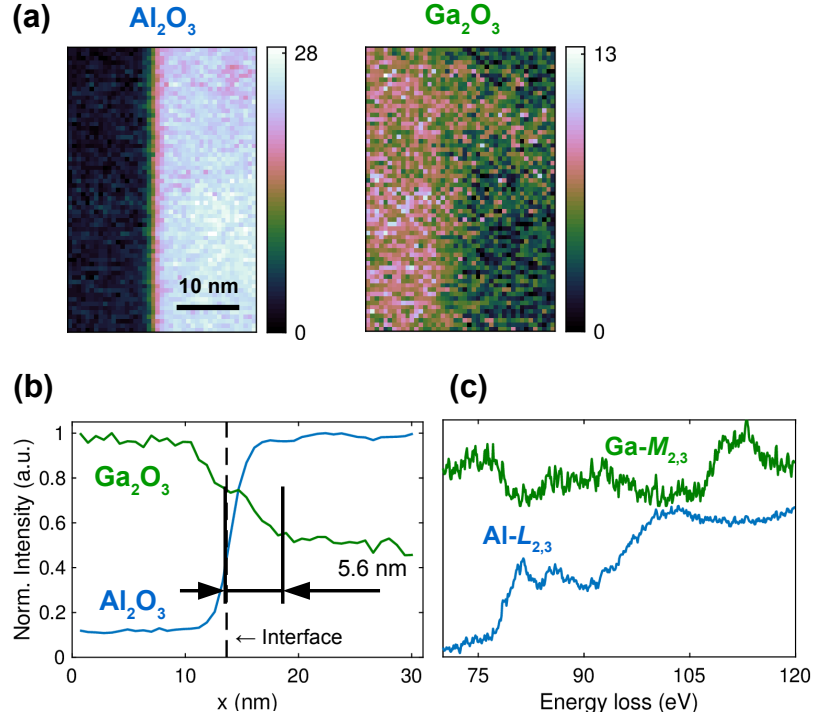


Figure 3.14: EELS spectrum image from a $\text{Ga}_2\text{O}_3/\text{Al}_2\text{O}_3$ MOS sample treated by 500 °C PDA. (a) Relative intensity maps of the principal NMF components belonging to Al_2O_3 (left) and Ga_2O_3 (right), respectively. (b) Line profile of the gradual tail-off in Ga intensity extending 5.6 nm into the Al_2O_3 layer. (c) NMF component spectra corresponding to $\text{Ga-M}_{2,3}$ and $\text{Al-L}_{2,3}$ EELS edges.

deposition anneal (Sample #25) as indicated by NMF analysis of interfacial EELS data presented in Fig. 3.14. The Ga signal in this device extended about 5.6 nm into the Al_2O_3 gate layer before leveling off.

This result was validated with higher confidence using the MCR-LLM algorithm which has been recently demonstrated to identify strongly overlapping, low signal-to-noise ratio EELS components as detailed in Sec. 2.1.2.2. A spatial integration of each column in the spectrum image (parallel to the interface) was performed prior to MCR-LLM decomposition in order to satisfy the constraint of the algorithm to 1 spatial dimension, as well as to enhance the strength of the raw EEL

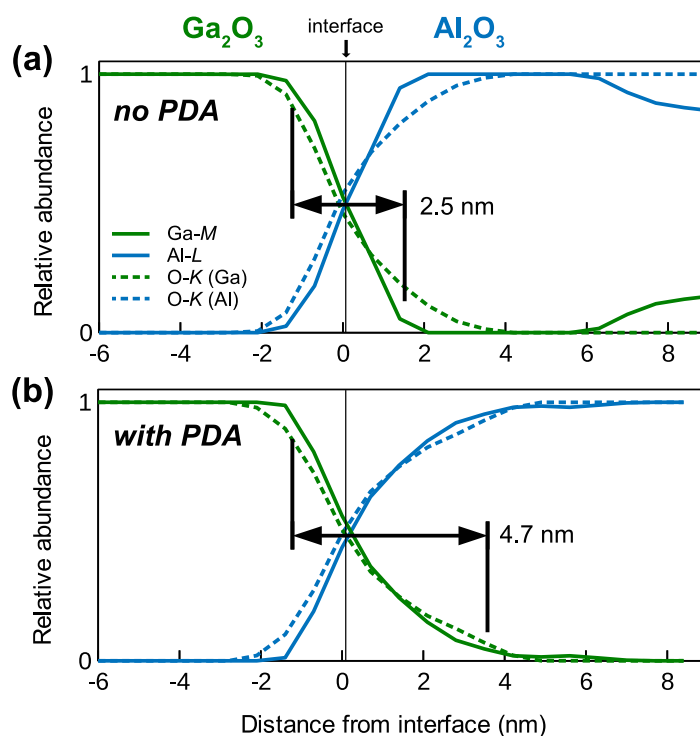


Figure 3.15: Comparison of line profiles generated by MCR-LLM from the $\text{Ga}_2\text{O}_3/\text{Al}_2\text{O}_3$ interface, (a) without PDA and (b) following $500\text{ }^\circ\text{C}$ PDA. The width of the 95–5% drop in intensity of the Ga-M component (solid green line) across the interface nearly doubled from 2.5 nm without PDA to 4.7 nm following the PDA process, clearly demonstrating the role of PDA in promoting interdiffusion between Ga and Al. Dashed green and blue lines represent the abundance of O-K signals originating with Ga_2O_3 and Al_2O_3 , respectively.

signal. MCR-LLM-generated line profiles of Ga and Al relative abundance across the interfaces are shown by the solid lines in Fig. 3.15a (corresponding to the NMF plot in Fig. 3.13b) and Fig. 3.15b (corresponding to Fig. 3.14b). Additionally, the abundance of O-K EELS edges are indicated for the Ga and Al components by dashed green and blue lines, respectively. The line profiles are qualitatively similar to those produced by NMF, but with significantly less noise, which facilitates understanding of the effects PDA has on the $\text{Ga}_2\text{O}_3/\text{Al}_2\text{O}_3$ interface. The width of the interdiffusion region was represented by the 95–5% intensity drop across the inter-

face. Following PDA the width of this region nearly doubled from 2.5 nm to 4.7 nm, indicating the pronounced diffusion effect promoted by PDA. MCR-LLM profiles also more clearly reveal the asymmetric nature of the diffusion, with Ga penetrating more deeply into the Al₂O₃ gate layer than Al into the Ga₂O₃ substrate.

An anomalous Ga feature appears within the un-annealed Al₂O₃ region, several nm away from the interface. This feature does not appear to be a non-physical “artifact” of the multivariate analysis, as it appeared in multiple Al-*L* + Ga-*M* spectrum images from the specimen (Sample # 24). Furthermore, a noisy but perceptible rise in Ga-*M* signal is also visible in the NMF decomposition (Fig. 3.13b) a few nm into the Al₂O₃ layer, around $x = 40\text{--}50$ nm. This feature was not expected to arise during ALD growth of the gate layer, nor was it seen in other samples prepared under the conditions in Table 3.1. By elimination of other possibilities, the most likely explanation for the anomaly is Ga⁺ ion implantation during final FIB preparation of the lamella. Ga FIB preparation has been known to induce ion-implantation damage in metallic Al foils up to 20 nm deep for a 30-kV Ga⁺ beam [115].

Relationship between interface structure and electrical peoperties

These results indicate that structural changes at the β -Ga₂O₃/Al₂O₃ interface indeed contribute to the increased density of interface traps measured by Jayawardena in these Ga₂O₃/Al₂O₃ devices subjected to post-deposition annealing [23]. Potential mechanisms for this increase include different interface trap profiles in the

mixed phase $(\text{AlGa})_2\text{O}_3$ transition region [116] and the formation of O vacancy or interstitial defects depending on whether the ambient process condition is O-poor or O-rich, respectively [117]. Annealing in this work was conducted in an O-poor forming gas environment and therefore expected to contribute O vacancies to the system, which tended to act as electron traps at the interface [118]. This dependence raises the possibility of controlling the defect structure at the $\text{Al}_2\text{O}_3/\beta\text{-Ga}_2\text{O}_3$ interface via the annealing environment as reported by Zhou et al., who compensated for O vacancies by annealing in O_2 [119].

This set of experiments sheds light on the structural features responsible for undesirable increases in interface trap density and interfacial roughness in Ga_2O_3 MOS capacitors with CVD-deposited SiO_2 and ALD Al_2O_3 gate oxides. Inspection of $\text{Ga}_2\text{O}_3/\text{SiO}_2$ interfaces by HRTEM imaging reveals that post-deposition annealing parameters affect the interface roughness, with greater roughness attributed to higher PDA temperatures. At the $\text{Ga}_2\text{O}_3/\text{Al}_2\text{O}_3$ interfaces, EELS line profiles show interdiffusion between the Ga_2O_3 substrates and Al_2O_3 films. This effect was amplified by post-deposition annealing and indicates mechanisms for the increased interface trap density associated with the mixed-phase region.

3.2.2 Electron beam-induced crystallization of Al_2O_3 gate oxides

Rapid crystallization of the initially amorphous ALD-grown Al_2O_3 gate layers in TEM lamellas was an unexpected finding from the work in Sec. 3.2.1, given the chemical stability of the materials in question and the unremarkable doses of

electron irradiation used for TEM imaging. This phenomenon was consistently reproducible, and warranted further investigation from a purely fundamental materials science standpoint. Furthermore, while it is not obvious from microscopy alone what the performance and reliability implications may be for MOS devices subjected to electron irradiation and/or complete crystallization of the gate oxide layer, recent reports indicate that they may be substantial. This section of the thesis describes quantitative investigation of the electron beam-induced crystallization phenomenon, further research possibilities and the potential implications for Al₂O₃-gated MOS devices based on β -Ga₂O₃.

3.2.2.1 Experimental methods

Sample preparation

The same set of TEM specimens prepared by Auburn University for the experiments in Sec. 3.2.1 were used to investigate the gate oxide crystallization, albeit with pristine regions of the interface not previously used for STEM/EELS spectrum imaging or HRTEM. Refer to Sec. 3.2.1 for fabrication conditions. All four samples with Al₂O₃ gate oxides were inspected qualitatively for crystallization phenomena, and one (#454) was investigated quantitatively in detail.

Electron microscopy imaging and spectroscopy

In addition to high-resolution images, diffraction patterns and Fast Fourier Transform patterns (FFTs) provided evidence of the crystal structures and orien-

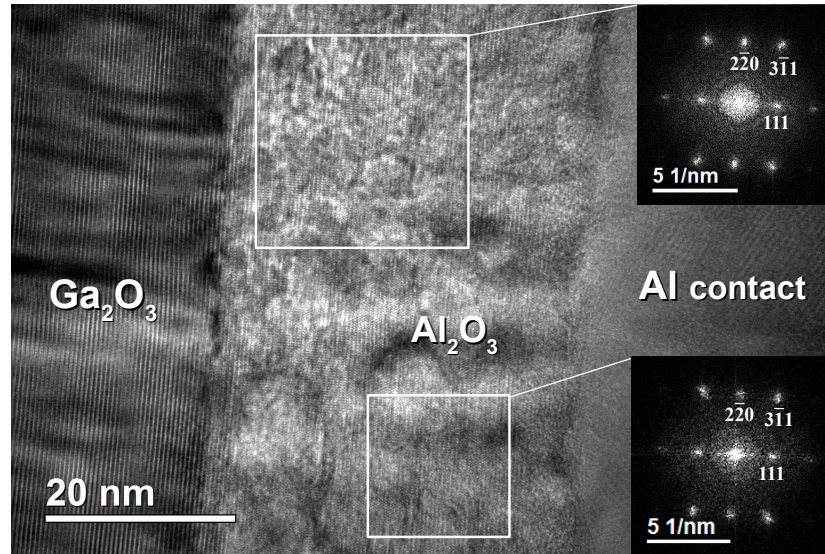


Figure 3.16: Lower-magnification TEM image of the interface near the area shown in Fig. 3.12(b) illustrating the lateral extent of crystallite formation along the interface. The crystallized region ultimately extended through the entire depth of the Al_2O_3 gate oxide layer up to the Al contact. Insets: FFT patterns indicate the high degree of crystalline orientation within the gate oxide.

tations at the interfaces studied. The lower-magnification image with associated FFTs in Fig. 3.16 illustrates the spatial extent and degree of crystalline ordering. A major challenge in studying this system was capturing images, diffraction and FFT patterns frequently enough to show the evolution of the amorphous–crystalline transition. Ideally each would be captured every second or even more frequently, which was not feasible manually or through the automatic capture functionality of Digital Micrograph. A successful workaround was to record a video screen capture of the live image and FFT together while translating along the interface and exposing different regions of the specimen to the electron beam. EELS spectrum images collected for Sec. 3.2.1 were also used in this section to identify features relevant to the crystallization phenomenon; analyses using the NMF and MCR-LLM algorithms

Beam energy (keV)	Beam diameter (nm)	Current density (A/cm ²)	Crystallization front rate (nm/s)	Time to crystallize (s)	Corresponding dose (e nm ⁻²)
200	168 ± 8	23.5 ± 2.0	2.3 ± 0.4	18	6.8 × 10 ⁷
200	360 ⁺³⁰ ₋₁₀₀	5 ⁺⁵ ₋₁	0.5 ± 0.2	60	5 ⁺⁵ ₋₁ × 10 ⁷
100	450 ± 24	5.0 ± 0.5	3.4 ± 0.4	13	1.4 × 10 ⁷
100	813 ± 43	1.5 ± 0.2	0.5 ± 0.2	55	1.3 × 10 ⁷

Table 3.2: Electron beam conditions (accelerating voltage and current density) and resulting crystallization effects on the Al₂O₃ gate oxide layer. At each of the 2 voltage conditions, the rate of crystallization corresponded to the electron dose rate and required similar overall doses to achieve complete crystallization, independent of the beam current density. Lowering the beam energy from 200 to 100 keV resulted in a factor of 4 drop in the necessary overall dose to complete crystallization.

were performed in order to clarify whether structural and compositional features originated with processing steps or were due to electron irradiation.

3.2.2.2 Quantification of the crystalline transformation

The crystallization phenomenon seen in all Al₂O₃ gate-oxide samples was qualitatively detailed in Sec. 3.2.1. A quantitative analysis of the crystalline transformation and its relationship to beam energies and intensities follows here. Measurements to determine electron-beam currents, current densities and dose rates imparted to the TEM specimens were performed in a separate session using a picoammeter in conjunction with the drift tube of the EEL spectrometer. The approach and results of these measurements are described in Appendix A.

Electron dose-rate dependence of crystallization front propagation

The electron beam conditions and corresponding crystallization phenomena in this work are summarized in Table 3.2. Crystallization was first observed under a 200 kV electron beam with a current density of 23.5 ± 2.0 A/cm², corresponding to an electron dose rate of 3.8×10^6 e nm⁻² s⁻¹. The crystallization front propagated in a direction parallel to the interface at a rate of 2.3 ± 0.4 nm/s. When the beam diameter was enlarged by a factor of 2, the current density was reduced to approximately 5 A/cm², and the same process was repeated in a pristine amorphous region where the crystallization propagated at the slower rate of 0.5 ± 0.2 nm/s. The roughly linear dependence of crystallization front speed on electron dose rate is suggestive of an electronic interaction mechanism. The overall dose required to locally achieve complete crystallization was independent of the beam convergence (current density).

About 18 seconds of exposure were required to completely crystallize the oxide layer under the 23.5 A/cm² condition, for a total dose of 6.8×10^7 e nm⁻². This value is comparable to the 4.5×10^7 e nm⁻² at 200 kV required by Nakamura et al. to obtain full transformation from amorphous to polycrystalline γ -Al₂O₃, as indicated by appearance of the (440) Debye-Scherrer ring [120]. In contrast, Murray et al. required a total of 2.0×10^9 e nm⁻² (16 min. under 13 A/cm²) to observe discrete diffraction spots with an Al₂O₃ film sandwiched between a sputtered Pt and Al film in a metal-insulator-metal capacitor structure [121].

Increased rate of crystallization at reduced beam energy

After observing crystallization under a 200 keV beam, pristine regions of the same sample were exposed to the same electron beam operating at 100 keV to provide insight into the nature of the electronic interaction process. Lower current densities were required to propagate crystallization at similar rates as with 200 keV electrons. Ultimately a factor of 4 lower electron dose was necessary to fully crystallize the gate oxide film under the 100-keV beam.

Two main types of electron beam-induced atomic displacement interactions occur in TEM: elastic scattering of electrons with atomic nuclei (knock-on displacement), and inelastic scattering of incident electrons with atomic electrons and subsequent bond-breaking (excitation and radiolysis, respectively). In general, knock-on effects are dominant for higher incident electron energies, which must be above a threshold energy E_0 (typically greater than 100 keV) in order to displace bulk atomic nuclei [122]. Radiolytic damage, by contrast, is more pronounced at lower energies because the inelastic scattering cross section is inversely related to the incident energy [123]. Inelastic scattering events are more likely with 100 keV electrons than 200 keV. Thus, the crystalline transformation observed may be attributed to an inelastic scattering process as reported by Nakamura et al. [120].

3.2.2.3 Factors contributing to crystallization of the Al₂O₃ gate layer

Negligible effect of beam-induced heating

High temperatures on the order of hundreds of degrees above ambient are normally needed to induce crystallization of amorphous ALD-deposited Al₂O₃ [124]. Two models of beam-induced heating independently show that beam-induced heating could not have played a meaningful role in the crystalline transformation described in this work.

The magnitude of beam-induced heating was first approximated using a simple heat-transfer model put forth by Egerton [122],

$$I \langle E \rangle = \frac{4\pi\kappa t(T - T_0)}{0.58 + 2\ln(2R_0/d)}, \quad (3.1)$$

where $I = 5$ nA is the TEM beam current as measured using the GIF and picoammeter, $\langle E \rangle = 45.1$ eV is the average energy loss within the gate oxide as measured by EELS (described in Fig. 3.17), i.e., the maximum energy per electron potentially lost to sample heating, $\kappa = 1.8$ W/(m K) is the thermal conductivity of Al₂O₃, the specimen thickness $t \approx 100$ nm, and the length scale R of the specimen is the 10- μ m width of the lamella. Under these conditions the temperature rise $T - T_0$ was only 0.2 K. This calculation suggests that beam-induced heating was negligible. However, this approach is limited by the assumption that the specimen has a single, isotropic value for thermal conductivity, which is not valid for a lamella comprising

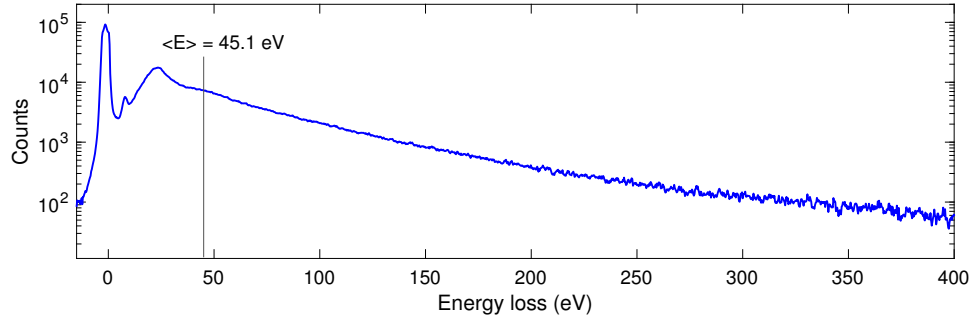


Figure 3.17: The average electron energy loss was identified by performing a weighted average of the complete EEL spectrum over the Al_2O_3 gate oxide layer shown above; $\langle E \rangle = 45.1$ eV. If it is assumed that all energy lost to the specimen via inelastic scattering is converted to heat, the maximum temperature increase of the specimen is given by Eq. 3.1. Note the use of a semi-log scale.

mostly Ga_2O_3 (whose conductivity is strongly anisotropic) and capped by an Al contact with good thermal conductivity.

To obtain a more complete understanding of thermal effects, a finite element model was constructed of the entire TEM lamella and Cu grid post to estimate the distribution of temperature rise due to beam-induced heating. The equilibrium temperature distribution of the lamella was simulated using the known specimen dimensions, material properties and electron beam current, and is illustrated in Fig. 3.18. The Al_2O_3 EEL spectrum in Fig. 3.17 indicated that an average of 45.1 eV of thermal energy was deposited into the lamella by each incident electron, at a rate corresponding to the electron-beam current of $I = 5$ nA. Using a simulated beam of diameter $d = 300$ nm, the maximum temperature rise was less than 0.2 K in all areas of the lamella.

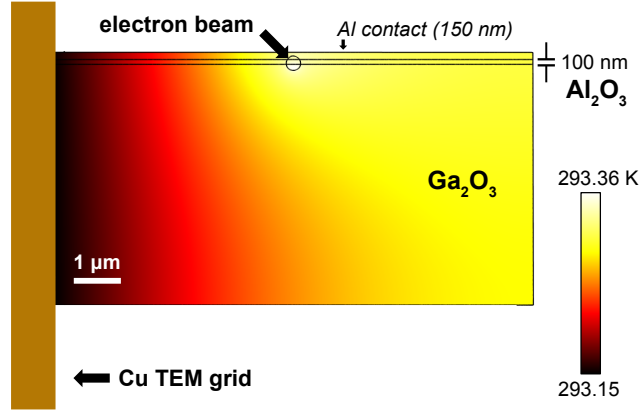


Figure 3.18: Finite-element model of the lamella temperature during exposure to a simulated 5-nA electron beam. The lamella consisted of the 100 nm thick, 10- μm -wide Ga_2O_3 substrate with a 100 nm-thick Al_2O_3 gate layer, capped by a 150-nm-thick Al contact pad and mounted on one side to a standard Cu grid post. Despite the relatively low thermal conductivities of both oxide materials, the maximum temperature rise was on the order of 0.2 K, far from sufficient to crystallize amorphous ALD-deposited Al_2O_3 .

Epitaxial relationship between $\gamma\text{-Al}_2\text{O}_3$ and $(\bar{2}01)$ $\beta\text{-Ga}_2\text{O}_3$

The comparatively fast formation of a fully crystalline Al_2O_3 layer with preferred orientation in this work is attributed to the crystallinity of the $\beta\text{-Ga}_2\text{O}_3$ substrate, facilitated by the relatively good lattice mismatch between the two layers. This is supported by the observation that crystallites of Al_2O_3 did not homogeneously nucleate within the bulk of the gate layer, nor did crystallization propagate from the interface of the gate layer with the top Al contact for any beam conditions or samples used in these experiments.

Examination of the film and substrate orientation provides insight into the heteroepitaxy of $\gamma\text{-Al}_2\text{O}_3$ on $(\bar{2}01)$ -oriented $\beta\text{-Ga}_2\text{O}_3$. The diffraction pattern of the fully crystallized Al_2O_3 (Fig. 3.19) corresponds to a $\langle 112 \rangle$ zone axis, parallel to the $[102]$ direction of Ga_2O_3 . In the plane of the film, therefore, $\beta\text{-Ga}_2\text{O}_3 [102] \parallel$

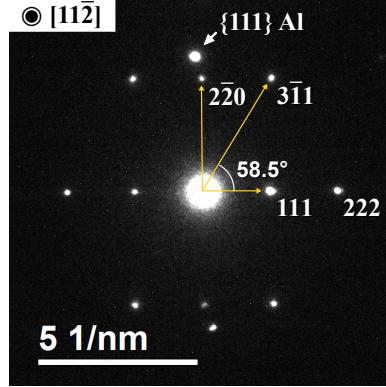


Figure 3.19: Electron diffraction pattern of the Al_2O_3 layer after crystallization. The magnitudes of the indicated diffraction peaks ($\mathbf{g}_{2\bar{2}0} = 3.54$ 1/nm, $\mathbf{g}_{111} = 2.12$ 1/nm and $\mathbf{g}_{3\bar{1}1} = 4.15$ 1/nm) as well as the angle between \mathbf{g}_{111} and $\mathbf{g}_{3\bar{1}1}$ match closely with the expected values for the idealized cubic $\gamma\text{-Al}_2\text{O}_3$ spinel structure [125].

$\gamma\text{-Al}_2\text{O}_3$ $[11\bar{2}]$. Parallel to the interface and normal to the electron beam, the in-plane epitaxial relationship observed is $\beta\text{-Ga}_2\text{O}_3$ $[010] \parallel \gamma\text{-Al}_2\text{O}_3$ $[\bar{1}10]$. Inspection of the oxygen sub-lattice of $(\bar{2}01)$ $\beta\text{-Ga}_2\text{O}_3$ shows that it has approximately hexagonal symmetry, similar to that of (111) $\gamma\text{-Al}_2\text{O}_3$ as depicted in Fig. 3.20. The average oxygen sub-lattice mismatch in each direction is calculated using the lattice constants for cubic $\gamma\text{-Al}_2\text{O}_3$ (denoted $a' = 0.79$ nm) [125, 126] and monoclinic $\beta\text{-Ga}_2\text{O}_3$ ($a = 1.2214$, $b = 0.3037$, $c = 0.5798$ nm, $\beta = 103.83^\circ$) [127]. Along the $[010]$ direction of Ga_2O_3 :

$$f_{010} = \frac{d_{110}^{\text{Al}_2\text{O}_3} - d_{010}^{\text{Ga}_2\text{O}_3}}{d_{010}^{\text{Ga}_2\text{O}_3}} = \frac{(a'/4)|[1\bar{1}0]| - b}{b} = -0.080 \quad (3.2)$$

and, using the empirically determined atomic structure of $\beta\text{-Ga}_2\text{O}_3$ [127–129] to find the average separation of O atoms along the $[102]$ direction, $d_{102}^{\text{Ga}_2\text{O}_3} = 0.490$ nm:

$$f_{102} = \frac{d_{112}^{\text{Al}_2\text{O}_3} - d_{102}^{\text{Ga}_2\text{O}_3}}{d_{102}^{\text{Ga}_2\text{O}_3}} = \frac{(a'/4)|[11\bar{2}]| - d_{102}^{\text{Ga}_2\text{O}_3}}{d_{102}^{\text{Ga}_2\text{O}_3}} = -0.013. \quad (3.3)$$

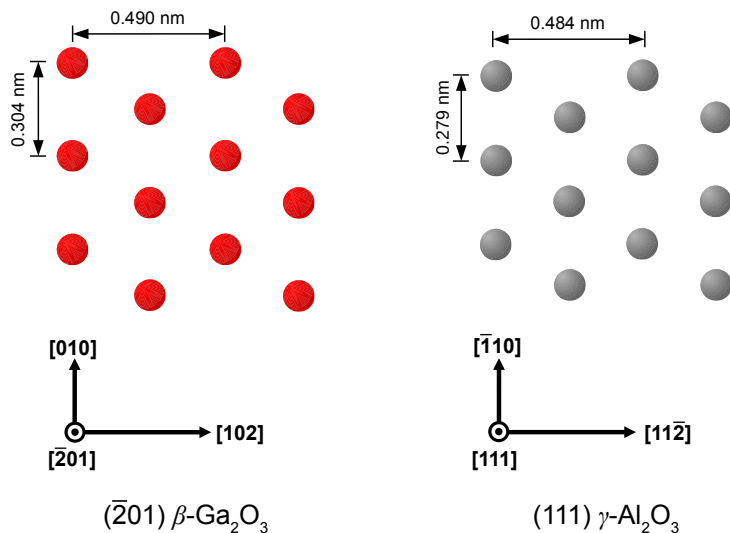


Figure 3.20: Oxygen sub-lattices of the $(\bar{2}01)$ β - Ga_2O_3 (red, at left) and (111) γ - Al_2O_3 planes (gray, at right) showing the in-plane epitaxial relationship observed. The $(\bar{2}01)$ β - Ga_2O_3 surface has approximately hexagonal symmetry, corresponding to the (111) surface of γ - Al_2O_3 . The in-plane lattice mismatch of the Al_2O_3 film along the $[\bar{1}10]$ direction of Al_2O_3 and the $[010]$ direction of Ga_2O_3 was approximately -0.080 , and about -0.013 along the $[11\bar{2}]$ direction of Al_2O_3 and the $[102]$ direction of Ga_2O_3 .

As discussed in prior works [112, 129] involving Al_2O_3 films on (010) -oriented β - Ga_2O_3 , an epitaxial relationship between these two systems is made possible by the similarity of their oxygen sub-lattices, which are both hexagonal in the plane of the film. The relatively small mismatch values, especially along the $[102]$ direction of β - Ga_2O_3 , allow for preferential orientation of the Al_2O_3 upon crystallization. The fact that both structures are well-matched is also consistent with the observation that the Al_2O_3 films only crystallized into the γ -phase in this work, not for example α - Al_2O_3 .

It is actually the θ - Al_2O_3 phase, and not γ - Al_2O_3 , which is monoclinic and isomorphic with the β - Ga_2O_3 substrate [126]. As such it is not intuitive that γ - Al_2O_3 will be the result of crystalline transformation. Nevertheless, the electron diffraction pattern of the fully crystallized Al_2O_3 (Fig. 3.19) is a better match to

γ -Al₂O₃ than to θ -Al₂O₃ in terms of the magnitudes and ratios of its \mathbf{g} -vectors. Furthermore, the lattice mismatch between β -Ga₂O₃ and *either* phase of Al₂O₃ is such that the Al₂O₃ film must be under tensile strain, due to the lattice constant $b = 0.304$ nm of Ga₂O₃ being larger than the corresponding $b = 0.291$ nm of θ -Al₂O₃ or $d_{220} = \sqrt{2}/4a = 0.28$ nm of γ -Al₂O₃. If the diffraction pattern were from θ -Al₂O₃, its $\mathbf{g}_{2\bar{2}0}$ magnitude would imply that the film were under significant *compressive* strain of $\frac{(1/3.44)-(1/3.54)}{1/3.44} = 2.8\%$. On the other hand, if the film were γ -Al₂O₃ as we assert, it would be under a more reasonable tensile strain of $\frac{(1/3.57)-(1/3.54)}{1/3.57} = -0.8\%$.

The density of amorphous alumina varies over a wide range, from 2.1–3.6 g/cm³ depending on deposition parameters, with typical values for low-temperature ALD ranging from 2.5–3.0 g/cm³ [130,131]—all lower than the 3.65 g/cm³ density for γ -Al₂O₃. In the course of accommodating this difference the crystallization process must therefore give rise to densification of the gate oxide layer. Tensile strain at the interface implies a local density reduction for crystallites that are coherently matched to the substrate, which should lower the energy barrier to initial formation of Al₂O₃ crystallites on the β -Ga₂O₃ substrate (as compared to e.g. a sapphire substrate).

Atomic rearrangement during post-deposition annealing

Consideration of the sample subjected to 500 °C, 2-min. post-deposition annealing (PDA) provides additional evidence of the negligible role of thermal effects on crystallization in this system. Despite annealing at elevated temperature, TEM

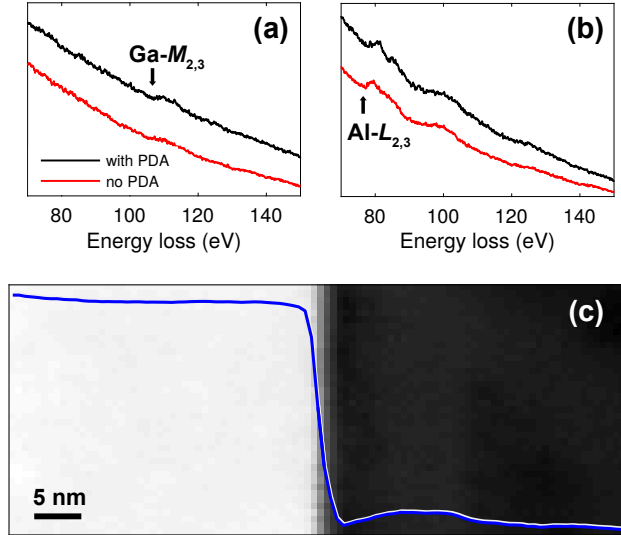


Figure 3.21: (a) Raw EELS spectra obtained as line scans from the bulk of the β -Ga₂O₃ substrates in the non-annealed (red) and annealed (black) samples. The weak, gradual onset of the Ga- $M_{2,3}$ EELS edge at 105 eV is indicated. (b) Corresponding EELS line-scan spectra from within the bulk of the Al₂O₃ gate layers (> 5 nm from the interface) after crystallization. The Al- $L_{2,3}$ edge is denoted at 77 eV. Signals from Si or other unintentional dopants were not observed. (c) HAADF-STEM image and normalized intensity line profile from the un-annealed sample collected simultaneously with the EELS data of the Ga- $M_{2,3}$ edge presented in the red curves of (a-b) and in Fig. 3.22.

imaging showed that the annealed gate oxide was initially amorphous, and became crystalline in the same way as the un-annealed samples following exposure to the electron beam. Furthermore, there is evidence that atomic rearrangement alone is not a sufficient condition for crystallization in the gate oxide layer, even at elevated temperatures. STEM-EELS spectrum imaging performed on samples with and without the PDA treatment (Fig. 3.21) revealed interdiffusion between Ga and Al in both cases. During the ALD process, interdiffusion led to a gradual drop-off in Ga intensity about 2.5 nm wide into the gate layer of the device not subjected to PDA, as shown in Fig. 3.22. In the annealed device, the width of this region had nearly doubled to 4.7 nm, indicating significant atomic rearrangement—but still with no observable crystallization of the amorphous Al₂O₃ prior to electron-beam

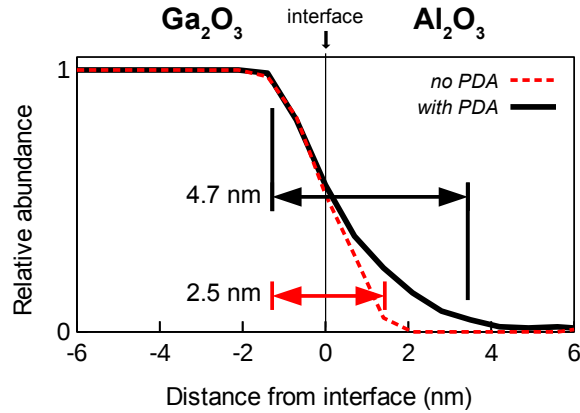


Figure 3.22: Line-profile average of the relative Ga- $M_{2,3}$ EELS edge signal identified by MCR-LLM in samples subjected to 500 °C post-deposition anneal (PDA) (solid black line; 5–95% intensity transition width 4.7 nm) and without post-deposition anneal (dashed red; transition width 2.5 nm). Despite the high temperature and atomic motion indicated by the broadening of the Ga signal tail-off following PDA, no crystalline interlayer was observed until the specimen was exposed to the electron beam.

irradiation in the TEM. This finding is consistent with recent work that subjected the (010) β - $\text{Ga}_2\text{O}_3/\text{Al}_2\text{O}_3$ interface to 5-min. PDA treatments at a range of temperatures and found that crystallization began between 600–700 °C [132].

3.2.2.4 Device performance implications and recommendations for future work

From a device applications perspective, the most natural questions relate to the stability and performance of MOS devices based on β - Ga_2O_3 with amorphous Al_2O_3 gate oxide layers. For instance, one of the desired use cases for WBG semiconductor electronics is high-radiation environments. Will the amorphous oxide remain stable under ionizing radiation? Recent work indicates that interface charge trapping and damage to the dielectric layer, not the intrinsic radiation hardness of the substrate, are the limiting factors for the robustness of a β - Ga_2O_3 device against gamma

radiation [133]. If an Al_2O_3 gate oxide crystallizes during the service lifetime of a device, this structural change will most likely be accompanied by changes in the device performance or reliability. The topics of radiation resistance and the effects of crystallization on the device behavior will require further investigation.

In summary, amorphous Al_2O_3 gate oxide layers grown by ALD on $(\bar{2}01)$ β - Ga_2O_3 substrates were found to become fully crystalline under electron irradiation in TEM. This phenomenon was observed reproducibly on samples both with and without PDA treatment at 500 °C. Estimates of the local temperature rise induced by the electron beam, on the order of 0.2 K, mean that thermal effects alone are far too small to induce crystallization in the amorphous gate layer. The roughly linear dependence of crystallization front propagation rate on electron dose rate, in combination with faster crystallization at lower beam energy, indicates that crystallization occurs via an electronic excitation process. Crystal growth is aided by the favorable lattice matching between β - Ga_2O_3 and γ - Al_2O_3 .

These findings raise several possible topics for further investigation. From an applications perspective, these include measuring the robustness (in terms of peak performance as well as long-term reliability) of β - Ga_2O_3 /amorphous Al_2O_3 devices during exposure to electron-beam or ionizing radiation, the electrical properties of devices after crystallization of the gate layer, and whether ALD process temperature plays a role in the early stages of the crystallization process.

Chapter 4: Modeling and characterization of nanocarbon-metal composites

Metal alloys are ubiquitous in modern life. From microscopic electromechanics to aircraft bodies, and from integrated circuits up to transcontinental electric grids—the engineering of metal alloys provides finely tuned combinations of cost-effectiveness, performance, and longevity in myriad applications. Copper and aluminum alloys have been the prevailing choice owing to their good combinations of electrical conductivity, mechanical strength, and low cost. Continued improvement in these properties is desirable, but difficult. Avenues for conductivity enhancement by traditional metallurgy techniques, such as striving for extremely high purity or designing single-crystal parts, are cost-prohibitive and offer limited benefits. As some nanostructured forms of carbon such as graphene [27] and carbon nanotubes (CNTs) [28] have exceptionally high mechanical strength and charge carrier mobility, the broad objective of this research is to investigate ways of incorporating carbon nanostructures into metal-matrix composites such that some combination of their bulk mechanical, electrical, or thermal properties are enhanced. The resultant nanocarbon-metal composites are known as *covetics*. This chapter describes a range of experiments to elucidate the structures responsible for these enhanced properties

using Raman spectroscopy, analytical electron microscopy, and modeling based on first-principles.

4.1 Analysis of C distribution and structure by Raman spectroscopy

Raman spectroscopy is an established technique that is well-suited to the characterization of carbon materials. Sec. 2.3 provides an introduction to the relevant literature regarding the characteristic modes of ordered and disordered carbon materials and the details of the curve-fitting routines used in this work. In Subsection 4.1.1, Raman spectroscopy has been used to provide new insights regarding the distribution of nano-graphitic crystallite sizes L_a , and in Subsection 4.1.2, to estimate the number of graphitic layers stacked in a typical cluster of GNRs.

4.1.1 Distribution of the nano-graphite crystallite size, L_a

Prior to the covetics reaction process

Raman spectrum imaging indicates that the activated carbon source material in this work was nanocrystalline, with an average crystallite size of 8.7 ± 1.8 nm calculated via Eq. 2.4. The uncertainty was estimated to be twice the standard deviation of a distribution containing 211 individual spectra from 4 separate areas of the activated C powder. Fig. 4.1 shows the average of all Raman spectra (left) and distribution of the associated L_a values from the individual spectra (right).

It is important to distinguish between the measurement error of the technique and the true width of the distribution, which is naturally greater than zero because

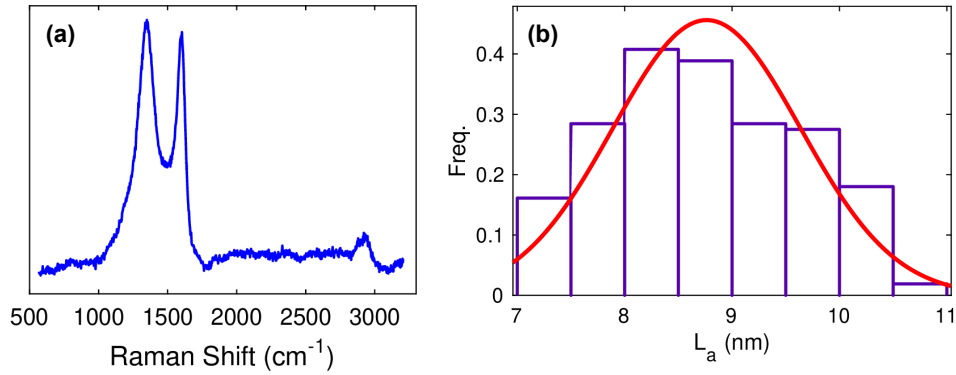


Figure 4.1: (a) The average Raman spectrum from activated C source material used in Al covetics qualitatively shows a low degree of ordering due to the broad D and G bands and low $I(G)/I(D)$ ratio. (b) Distribution of nano-graphite crystallite size L_a calculated from 211 individual spectra via Eq. 2.4. The average crystallite size was 8.7 ± 1.8 nm, with the uncertainty defined as 2σ .

the graphitic crystallites do not all have exactly the same size. The width of the distribution measured from the 211 spectra shown in Fig. 4.1(b) is the result of both of these sources of spreading. The narrow spread of L_a values is indicative of the low measurement error inherent in the Raman spectrum-imaging approach, as long as the signals are moderately strong; the absolute *uncertainty in the measurement* in any calculation of L_a via the $I(G)/I(D)$ ratio should not be greater than 1.8 nm.

After the covetics reaction

The threshold for distinguishing between converted and unconverted carbon in covetics is inevitably somewhat arbitrary, as the degrees of graphitic ordering lie on a spectrum, e.g. from fully amorphous to fully crystalline, and from small to large crystallites. The presence of a 2D peak, narrowing of the G and D peaks, and increase in the $I(G)/I(D)$ ratio are each indications of this transition which extend across a range, with fully “converted” and fully “unconverted” at either extreme.

It is nevertheless useful to define a threshold for conversion in order to make the analysis more quantitative. In the case of activated C powder, this threshold was defined as 2 standard deviations above the mean crystallite size, or 10.5 nm. On account of the normal distribution of the data, there is a less than 5% chance that any Raman spectrum would give an L_a value greater than this threshold in the as-received material (without having undergone transformation by the applied current).

4.1.1.1 Characteristic long-tailed distribution of L_a after conversion

Unlike the distribution of L_a for unconverted activated C, as shown in Fig. 4.1, distributions of L_a in covetics exhibited a distinct positive skewness. This asymmetry can be seen in datasets taken from 4 distinct covetic samples, each of which contains at least 1000 measurements from Raman maps collected in different regions of polished cross-sections. These data are presented in Fig. 4.2. The asymmetry was persistent across samples manufactured using different reaction times and different electrode geometries (therefore, different current densities), which suggests that it is characteristic of a sizable range of the covetics-fabrication parameter space. Each distribution is composed of a large number $N > 1000$ of L_a measurements from different parts of the specimen, and is therefore statistically meaningful.

In addition to the characteristic positive skewness, each of the distributions in Fig. 4.2 is bi-modal. As a consequence, it was necessary to fit each dataset to a

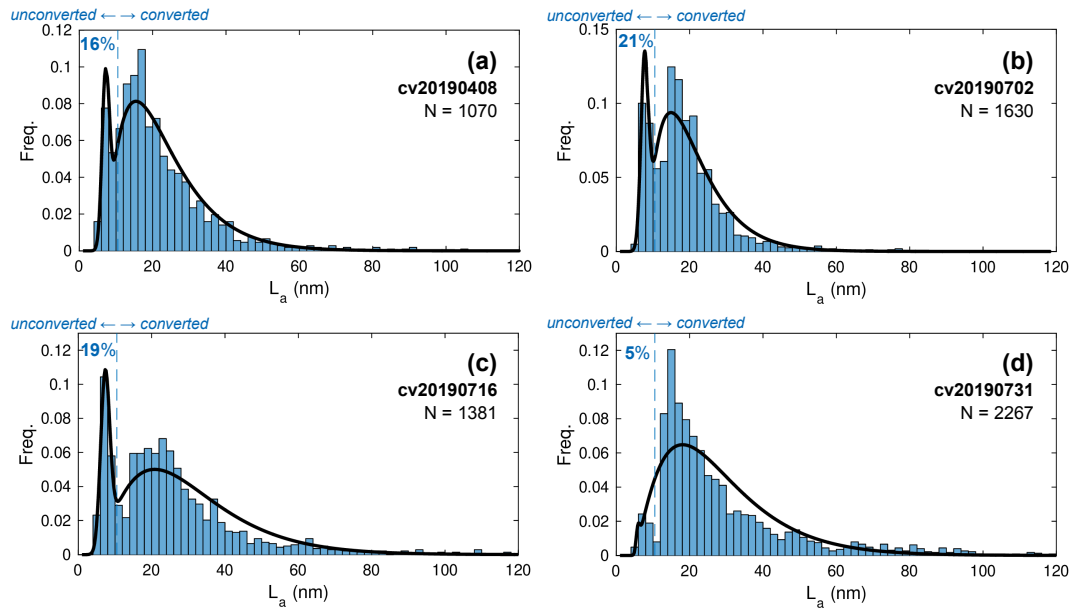


Figure 4.2: Distributions of carbon crystallite size L_a were consistently asymmetric across a range of covetics fabricated using different applied current densities and durations. The features of each distribution were enhanced by the use of a large number N of Raman spectra, each of which provides one measurement of L_a . Many of the distributions were bi-modal, which indicates that a fraction of the original carbon material remained unconverted (L_a below the cutoff of 10.5 nm, as indicated by the dashed vertical lines). A superposition of a normal distribution and a gamma distribution was chosen for the histogram fit in order to account for this feature. Each sample was identified by a number (cv2019xxxx) corresponding to its fabrication date. N is the total number of spectra used in the analysis of each sample.

superposition of a normal or Gaussian distribution and a gamma distribution:

$$(1 - p) \left[\frac{1}{\sigma\sqrt{2\pi}} e^{-\frac{1}{2}\left(\frac{x-\mu}{\sigma}\right)^2} \right] + p \left[\frac{1}{b^a\Gamma(a)} x^{a-1} e^{-x/b} \right] \quad (4.1)$$

where p is the fraction of converted carbon represented by the gamma distribution, $(1 - p)$ is the fraction of unconverted carbon represented by the Gaussian distribution, and the other symbols take their usual meanings in the context of probability distributions. Note that p was only used to determine the best fit for Eq. 4.1; a fixed cutoff of $L_a = 10.5$ nm was used to distinguish between the two regimes for all other purposes.

Physical meaning of bi-modality

When a prominent small- L_a peak was present, as in Fig. 4.2(a–c), it was narrow and symmetrical with a position of around 8 nm. This corresponds well with the distribution of L_a in the activated-carbon source material. As such, this peak can be attributed to un-reacted activated carbon. When the peak was small, as in Fig. 4.2(d), it is an indication that the graphitic conversion had proceeded more completely. In this case it is illustrative to note that sample #cv20190731 in Fig. 4.2(d) was fabricated for twice the duration of applied current, but otherwise under the same conditions as sample #cv20190716 in Fig. 4.2(c). This trend is supported more broadly by samples fabricated across a range of reaction residence times (i.e., the duration of applied current) as indicated by Fig. 4.3.

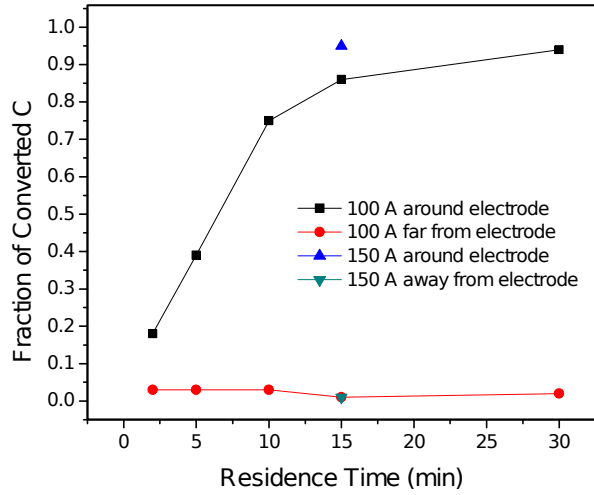


Figure 4.3: The fraction of carbon source material converted to larger graphitic crystallites, as defined by $L_a > 10.5$ nm, increased monotonically with residence time (the total exposure time of the melt to direct current), but only in regions within ≈ 5 mm of the electrode where the current density was above a critical value. Adapted from Ref. [134].

Physical meaning of positive skewness

The presence of positive skewness in the crystallite size distributions following the application of current is a clear indication of a physical transformation. No such feature was ever observed in the distribution of L_a in the as-received activated carbon material. In the midst of the large spread in the distribution, the mean of L_a values also increased monotonically with residence time. Representative distributions of samples fabricated using 100 A current over different durations are plotted in Fig. 4.4.

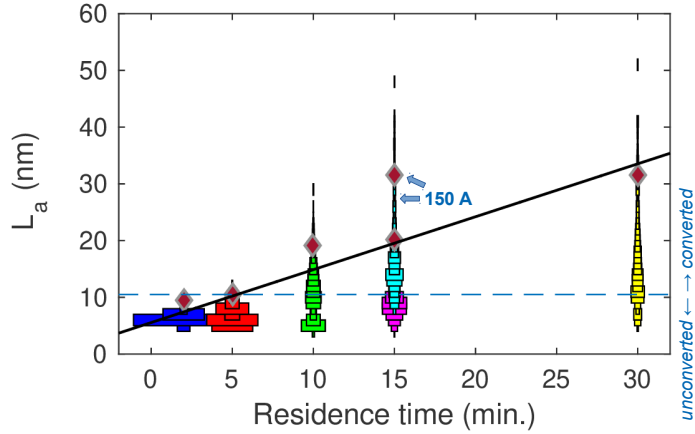


Figure 4.4: The mean L_a increased linearly with residence time ranging from 0 to 30 min. All reactions were conducted with an applied current of 100 A except for the single point and distribution indicated by arrows (light blue) for which the current was 150 A.

4.1.2 Estimating the thickness of embedded GNRs

It is not trivial to estimate the thickness (i.e., the number of layers) of the GNRs embedded in a covetic. Unlike the case of a wide and thin graphene sheet resting on a substrate, where the thickness can be obtained from visible light absorption of 2.3% per layer [135], optical thickness determination is not possible through the metal matrix (and furthermore, the GNRs are narrower than the wavelength of visible light). Conventional TEM imaging gives a projection through the whole specimen, and does not readily permit visualization of structures along the beam axis.

Inspection of the 2D Raman peak shape provides additional insight regarding the number of graphene layers. Experimental and theoretical studies show that the 2D band is described by a single Lorentzian peak for single-layer graphene, while the bilayer-graphene 2D band exhibits a pronounced shift, to 3 [136] or 4 peaks [83].

With 10 layers or more, a distinct asymmetry is present in the 2D band. (It is not possible to distinguish the number of layers when there are more than 10, because at that stage the 2D band begins to appear skewed positive, the same as it appears in bulk graphite [83, 137].) Qualitative inspection of 11 2D peaks distributed on the polished surface of a well-characterized covetic (cv20190408, Fig. 4.5) suggests that the typical number of layers is probably between 3 and 10. The 2D bands are broad, with maxima around 2700 cm^{-1} . These features are not consistent with single-layer graphene, which has a single Lorentzian peak around 2680 cm^{-1} [136]. Some of the bands are asymmetric, especially at spots 2, 9 and 11, as in bulk graphite with 10 or more layers; others appear more similar to spectra reported for structures with 2–6 layers [136, 137]. Overall, the GNRs contained approximately between 3–10 layers of graphene in this specimen.

It is important to bear in mind the limitations inherent in collecting Raman spectra from randomly distributed GNRs which have varying degrees of graphitic ordering. Since the Raman excitation-laser spot size is on the order of $1\text{ }\mu\text{m}$ in diameter—between one and two orders of magnitude greater than the width of GNRs—many GNRs will likely contribute to each Raman spectrum. The graphitization of the carbon precursor is not uniform for several reasons, including the non-uniformity of the current density distribution and/or mechanical stirring of the melt. Because of these uncertainties, the Raman-based interpretation of the number of graphene layers in GNRs remains an order-of-magnitude estimate.

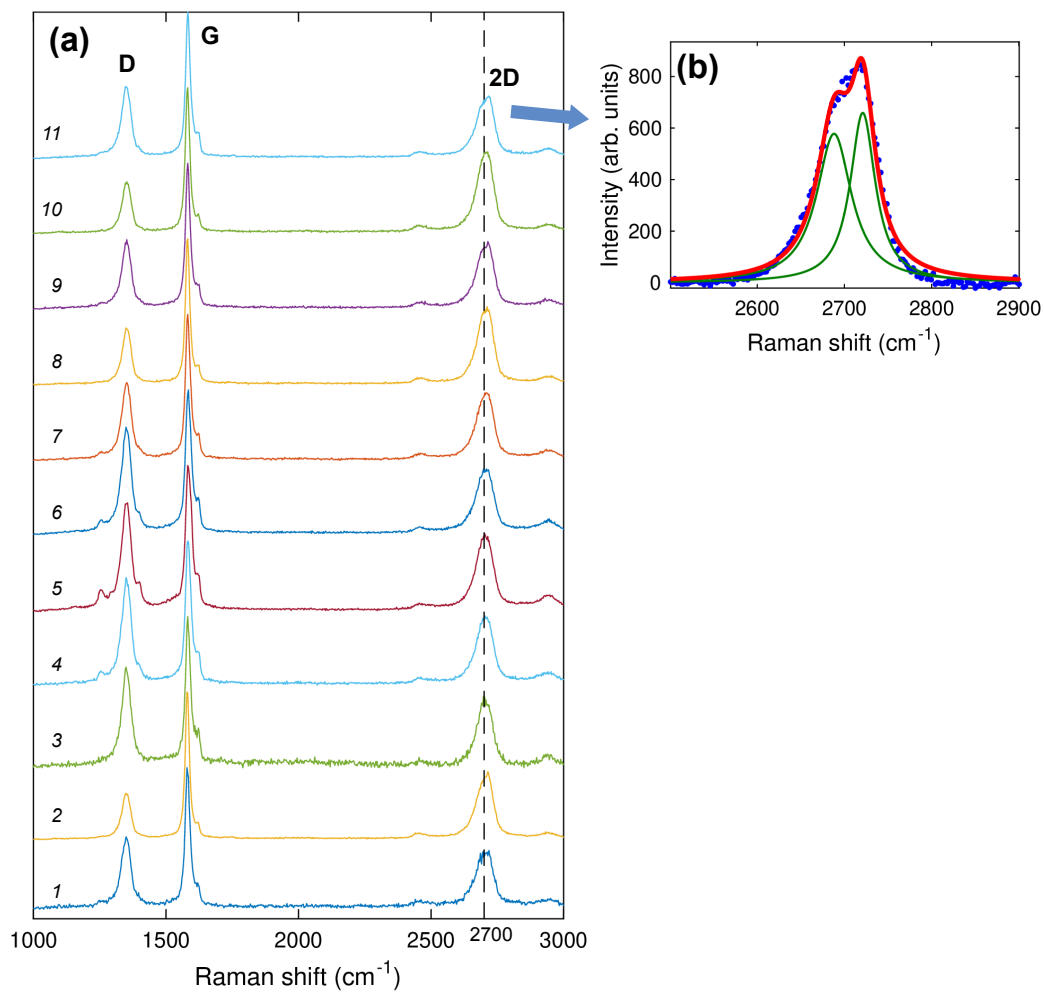


Figure 4.5: (a) Raman spectra from 11 points on the covetic sample cv20190408 with clearly defined 2D bands, plotted on a linear intensity scale of arbitrary magnitude. (b) Detail box of the 2D peak decomposition at point #11. The 2D bands do not appear as they would for either single-layer graphene (a single Lorentzian peak around 2680 cm^{-1}) or bulk graphite, which suggests qualitatively that the GNRs contained between 3–10 layers of graphene in the regions probed.

4.2 TEM investigation of metal-carbon interface structures

A wide range of TEM-based techniques were used to explore processing-structure-property relationships in Al coveotics produced under different conditions, as well as several reference specimens for comparison. The general approach was to evaluate structures over a broad range of length scales, from micron to sub-nanometer, to adapt to the many length scales across which the structure of a composite can vary.

4.2.1 Specimen preparation and experimental approach

As described in the preceding section, Raman spectroscopy was generally the first characterization step following fabrication, cutting and polishing. The optical- and spectrum-imaging length scale of tens of microns was well suited to positively identifying carbon-containing regions. These regions typically displayed darker contrast relative to the matrix, and often—but not always—exhibited strong Raman signals. Occasionally clusters of unconverted activated C were observed, physically trapped in the matrix. Being unique to coveotics, the ordered regions were prime candidates for further characterization, and their positions were recorded relative to a corner or other distinct feature of the sample surface so that they could be located later in SEM. An illustration of this approach is shown in Fig. 4.6.

Conversely, Raman spectra of carbon in any form were almost *never* observed in parts of the matrix that appeared optically like pure metal alloy. This limitation is due to the shallow penetration depth of visible light into metals; for example in Al, 90% of incident 532 nm light is attenuated within the top 15 nm, decaying expo-

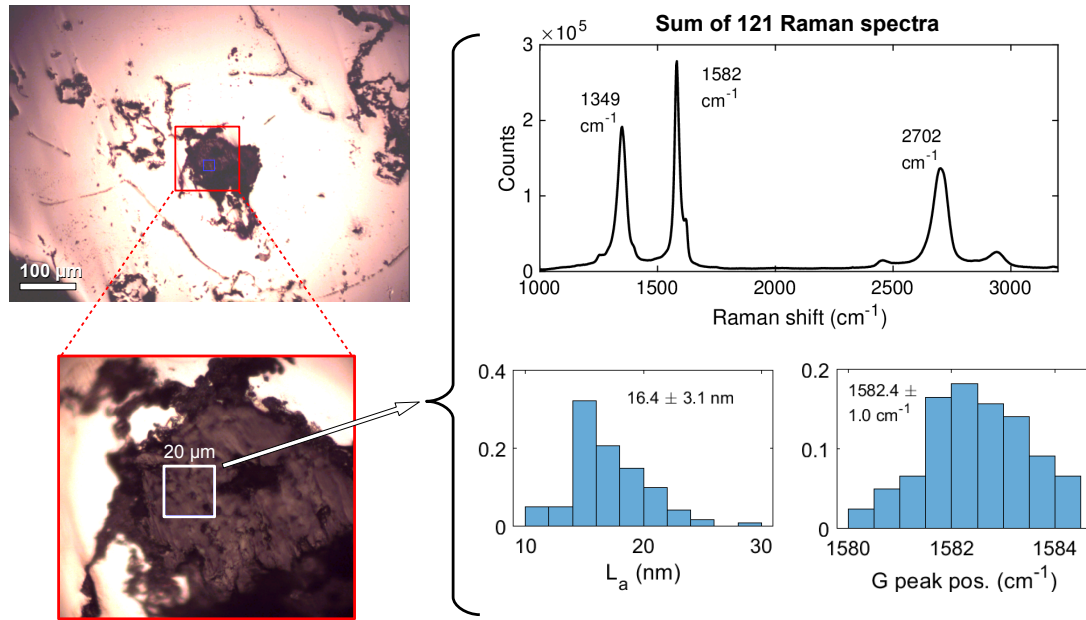


Figure 4.6: Simultaneously-collected optical image and average Raman spectrum of a polished covetic cross-section (Sample #cv20190408). The Raman spectra were collected from the region highlighted in the 20- $\mu\text{m} \times 20\text{-}\mu\text{m}$ white box (lower left detail box). According to the Raman spectra, the bright regions of optical images were exclusively metal matrix with no C signal, while the dark regions indicate graphitic or disordered carbon, grain boundaries, scratches, or voids.

nentially [138]. Essentially, only the surface of the cross section could be inspected for carbon of any degree of ordering; everything greater than a few nm below the surface was rendered invisible by the metal above it.

Several cross-sectional TEM specimens were prepared from regions similar to that shown in Fig. 4.6. EDS mapping prior to milling confirmed the presence and distribution of C; for instance, in the map in Fig. 4.7, which corresponds to the graphitic feature in Fig. 4.6. The approximately 1- μm depth of the volume of interaction in SEM at a beam energy of 20 keV [139] implies that these carbon structures extended on the order of 1 μm below the sample surface.

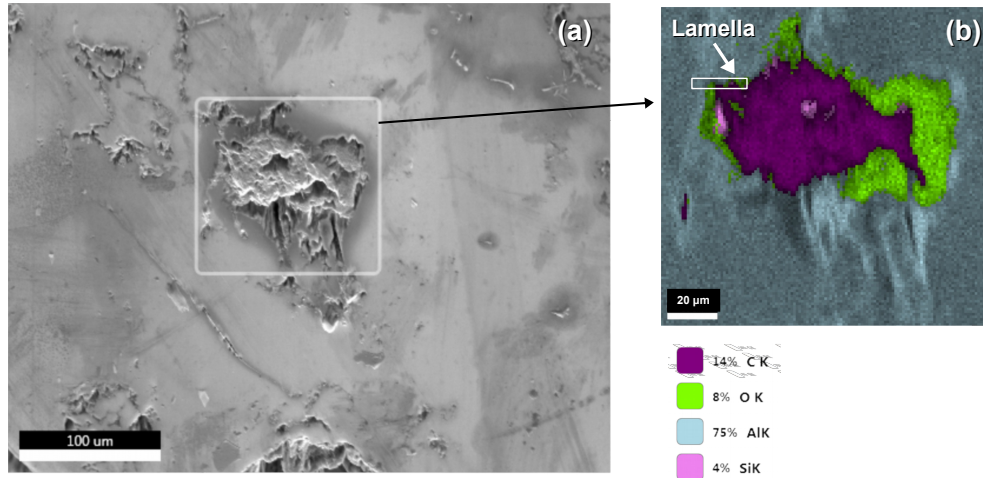


Figure 4.7: SEM-EDS mapping of the graphitic C feature shown in Fig. 4.6 prior to lamella extraction from the region indicated, using a beam energy of 20 keV.

4.2.2 Large-scale graphitic carbon structures in Al covetics

TEM revealed that the nano- to micro-structure of covetics was highly variable, even within the same sample. The most common feature was graphitized carbon on length scales of microns to tens of microns. A less common microstructure, aligned graphitic fibers and ribbons on a width scale of under one micron, is relatively more homogeneous and therefore offers potentially more benefits for the resultant composite, as previously identified by Jaim et al. [56] and explored theoretically in Sec. 4.3.

Samples were numbered by their date of fabrication. The sample numbered cv20190408 was ultimately found to exhibit both strongly graphitic Raman signals (Fig. 4.6) and a significant $5.7 \pm 1.5\%$ increase in conductivity relative to a carbon-free control subjected to the same metallurgical process [140]. As such, it was analyzed by a range of TEM-based techniques including bright-field (BF) and

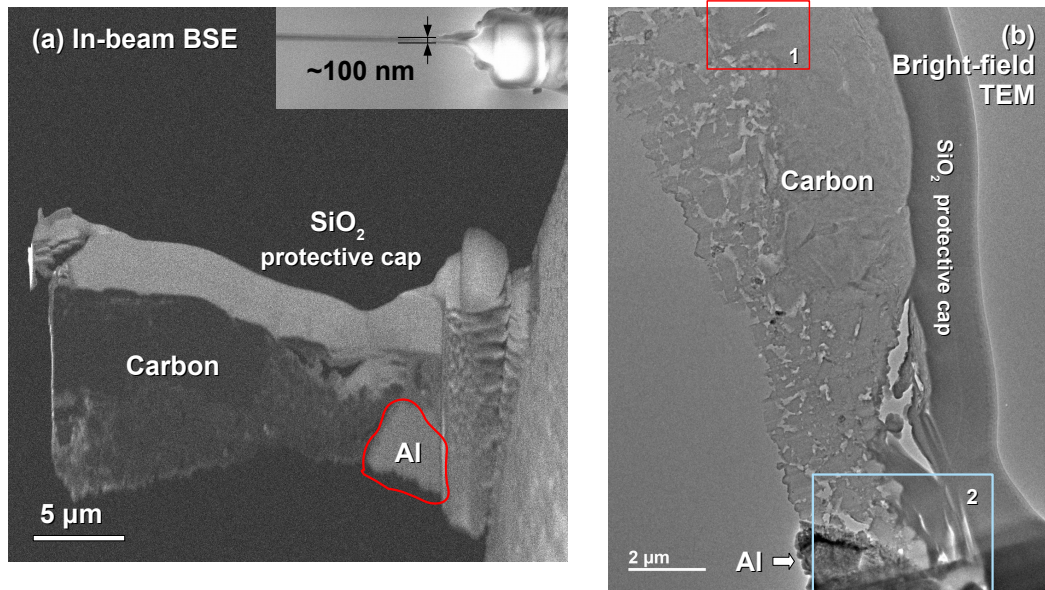


Figure 4.8: (a) In-beam backscattered electron (BSE) SEM image of the cv20190408 lamella after final thinning to approximately 100 nm with a 5-keV Ga^+ ion beam (Inset: SEM view down the lamella top edge). Higher- Z atoms produce stronger signals in the BSE detector, allowing the Al, C and protective SiO_2 regions to be distinguished. (b) 2 kx-magnification composite TEM image with two regions of interest highlighted: 1. Locally thinner area from the bulk of the graphitic inclusion; 2. The Al-C interface region.

dark-field (DF) imaging, diffraction pattern analysis, and scanning TEM (STEM) spectrum imaging. SEM and TEM images of the cv20190408 lamella are shown in Fig. 4.8.

Fig. 4.9(a) shows that the graphitic structures are uniform over several microns in some areas, while others are locally thinner or thicker, or appear as small grains. Higher-resolution inspection of region 1 indicated that the bulk of the carbon inclusion is graphitic. The electron diffraction pattern from this region (Fig. 4.9(b)) indicates a lattice spacing of 0.353 nm, which is about 4% larger than the c -axis interplanar spacing of graphite. The locally thin structure visible in Fig. 4.9(c-d) shows lattice fringes of C parallel to the longer dimension of the thin area. This

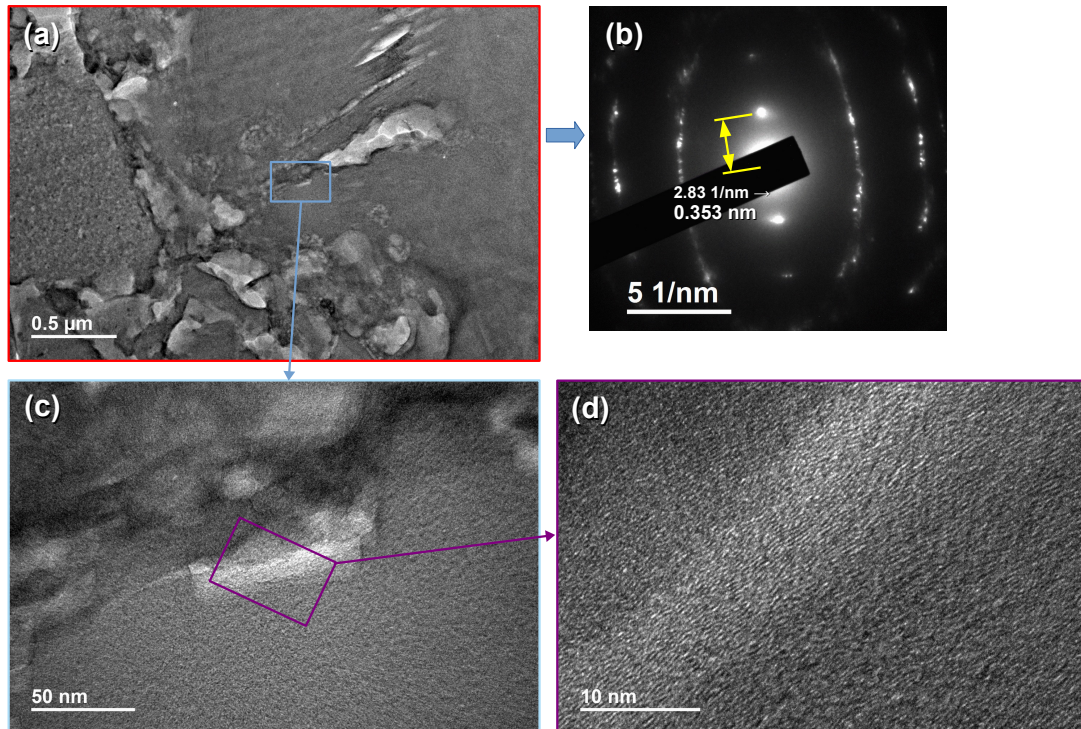


Figure 4.9: TEM images of region 1 from Fig. 4.8(b) at progressively increasing resolution. (a) 8 kx image of graphitic structures which are uniform over several microns in some areas, while other areas are locally thinner, thicker, or comprise small grains. (b) Electron diffraction pattern corresponding to (a) indicating an interplanar spacing corresponding to that of layered graphene. (c–d) Detailed view of a locally thin area at 100 kx and 500 kx, respectively, with the latter showing lattice fringes of C with small-scale undulations along the longer dimension of the thin area.

structure is substantially more ordered than the activated carbon source material, however it retains some disorder at the atomic scale.

Composition analysis of this specimen was primarily done via energy-filtered TEM (EFTEM), which makes use of the filtering capabilities of the electron energy-loss spectrometer to form images using only the chosen energy-loss signals (Sec. 2.1.2). It provides a fast, qualitative picture of composition over a large length scale, complementary to e.g. STEM-EELS spectrum imaging. EFTEM images from the bulk of the graphitic region 1 are shown in Fig. 4.10. They reveal that C is the predominant element in this region, with trace presence of O around the edges of the thin regions in the specimen (which appear brighter in the bright-field and zero-loss images). No meaningful signals were seen in energy ranges corresponding to Si-*L* and Fe-*L*, which are trace elements in Al 1350 (the parent alloy for this specimen) and other 1000- and 6000-series alloys [141].

The region containing the Al-C interface (ROI 2 in Fig. 4.8(b)) was also imaged by EFTEM; these composition maps are shown in Fig. 4.11. Carbon is predominant on the left side of the interface in the EFTEM images, while Al is present only on the right. Some oxygen was present everywhere, generally overlapping with the Al. This overlap suggests that the graphitic carbon was in contact with an aluminum oxide phase and not pure metal. A color-enhanced superposition of the C, Al, and O EFTEM maps shows this structure more clearly in Fig. 4.12.

A second TEM specimen was prepared from the same bulk sample of cv20190408 by ion milling in order to explore a larger electron-transparent area with similar interface features. The regions of interest indicated in Fig. 4.13 were investigated by

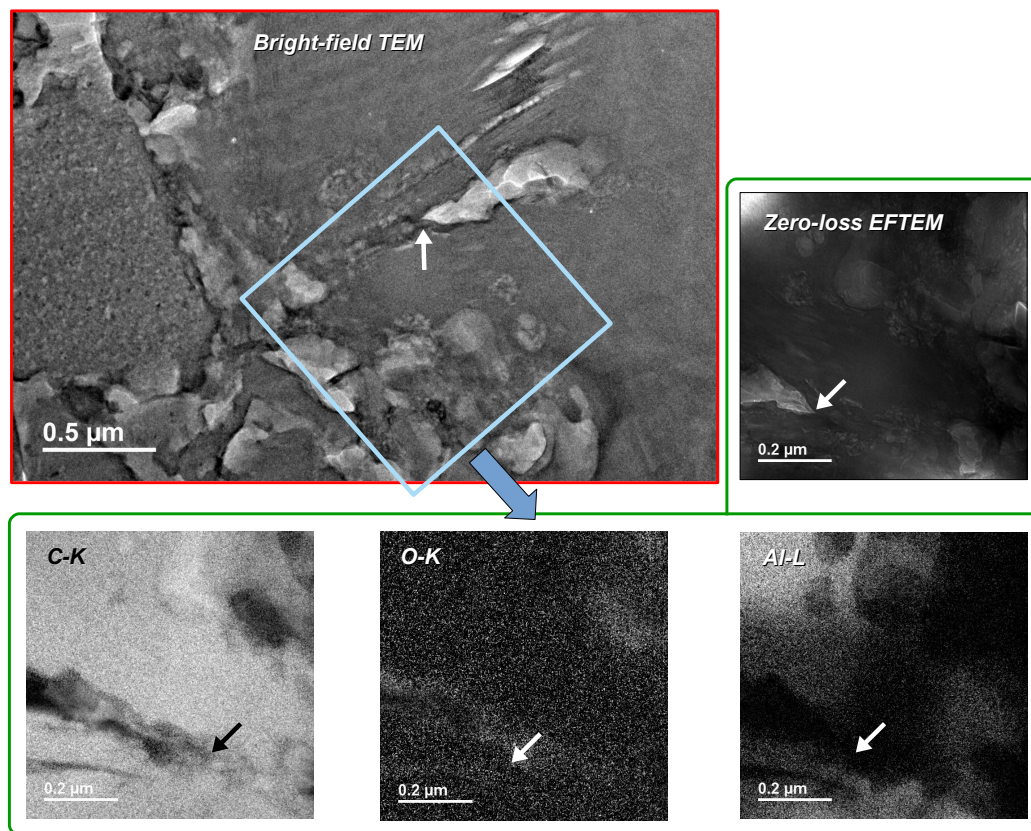


Figure 4.10: Energy-filtered TEM images captured from the graphitic bulk in the region highlighted, revealing predominantly C with weak traces of other elements. The zero-loss EFTEM image is composed of electrons with energy losses less than 10 eV (the slit width), while the core-loss edges used a slit width of 30 eV. Black and white arrows indicate a common feature of reference (point of elongated thin feature) and direction between the BF and EFTEM images to assist with the viewer's orientation.

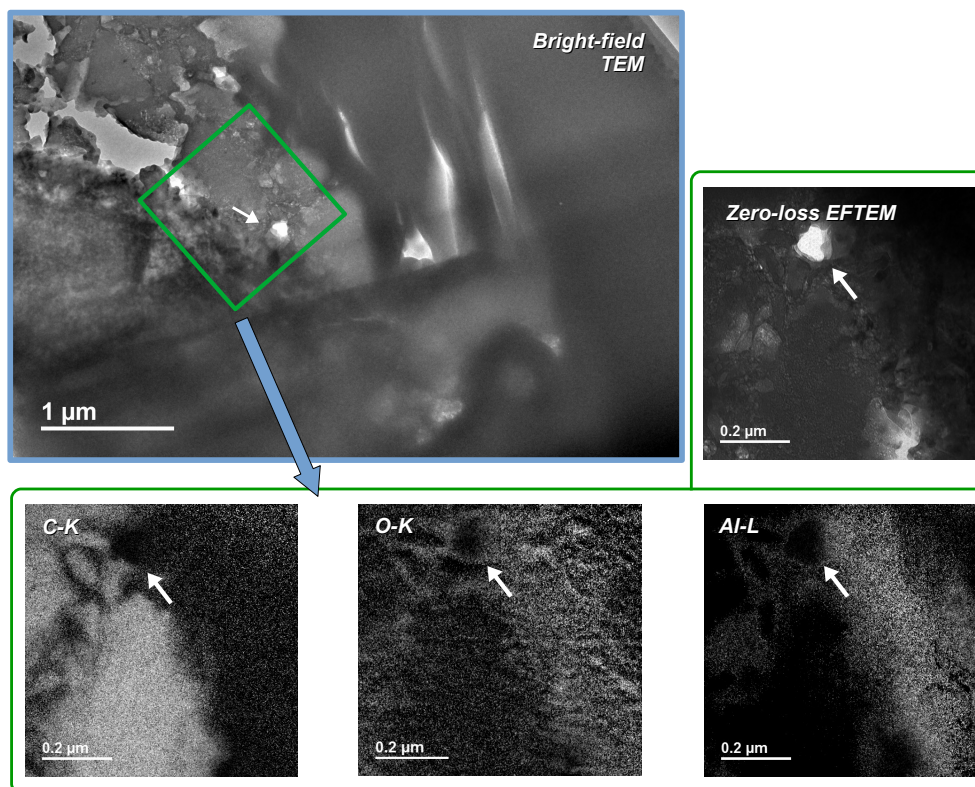


Figure 4.11: EFTEM composition mapping captured from the graphitic carbon/Al interface of cv20190408 over the region highlighted in green in the bright-field TEM image. Arrows face in the same direction towards a common feature in all images. Overlap in the Al- and O-rich regions at the right of the EFTEM images suggest the presence of an aluminum oxide phase next to the carbon.

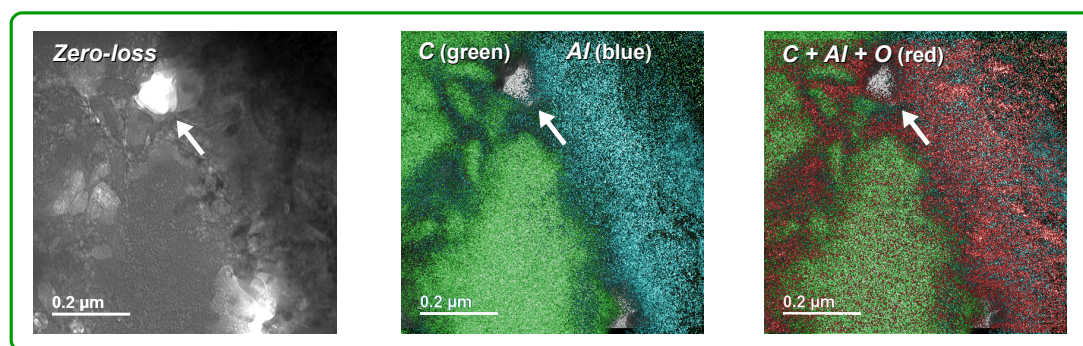


Figure 4.12: Color-enhanced superposition of EFTEM images from the C/Al interface in Fig. 4.11. Center image: superposition of C (green, left side) and Al signals (blue, right side) reveals minimal overlap between the two phases. Right image: All three concentration maps (C, Al, and O, red) superimposed. O and Al coincide, suggesting an aluminum oxide phase instead of pure Al alloy.

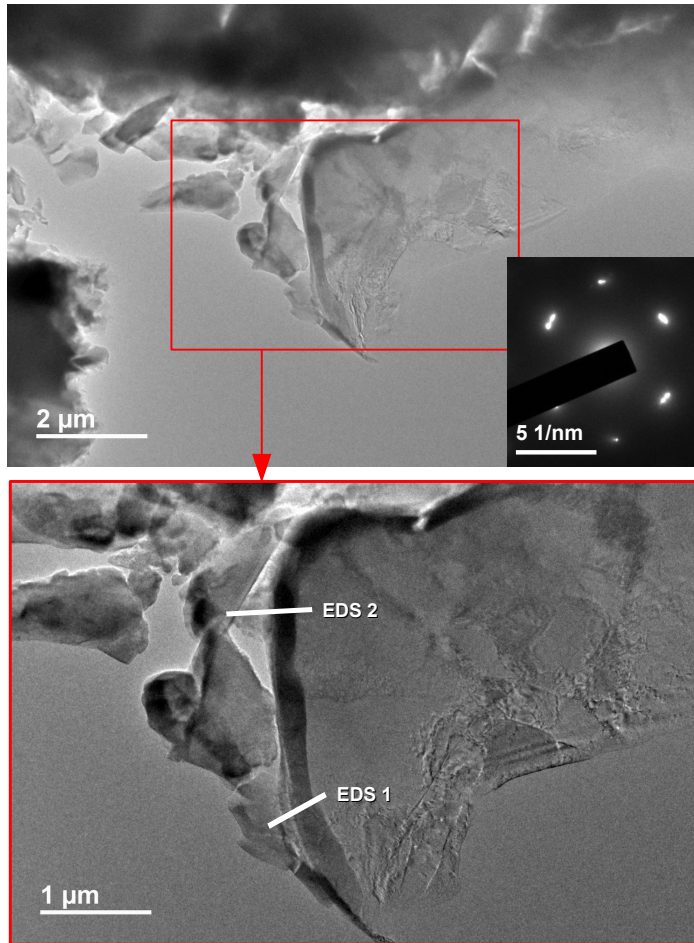


Figure 4.13: Survey of cv20190408 TEM specimen prepared by ion milling. Top: The Al/C interface structure shown is representative of others seen around the electron-transparent perimeter of the hole in the ion-milled specimen. Inset: Multiple diffraction spots originating from Al indicate slight misorientations of Al crystallites around a $\langle 110 \rangle$ zone axis. Bottom: Detail view of the interface structure with two regions of interest marked for STEM-EDS analysis.

STEM-EDS to provide a more quantitative composition analysis. The specimen was oriented such that it was imaged down a $\langle 110 \rangle$ zone axis. Multiple diffraction spots originating from Al indicate slight rotations of Al crystallites with respect to each other; this grain structure was frequently seen in covectics. STEM and EDS data from the thinner region of interest denoted EDS 1, near the bottom of Fig. 4.13, are shown in Fig. 4.14. In the HAADF-STEM image in Fig. 4.14(a), bright regions

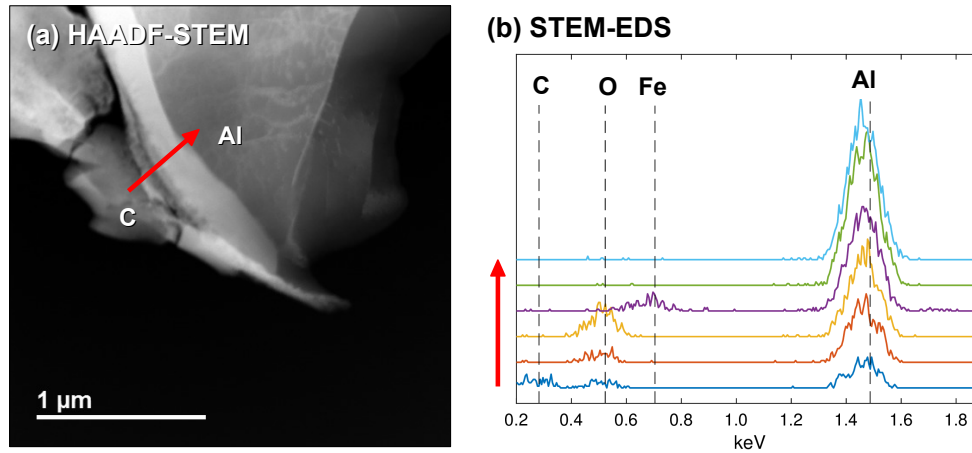


Figure 4.14: (a) High-angle annular dark field (HAADF)-STEM image from the region of EDS 1 in Fig. 4.13; the red arrow indicates the position of the EDS line scan. Stronger (i.e. brighter) high-angle scattering signals originate with higher atomic-mass species, indicating that such species were present in a band between C and Al. (b) EDS line-scan signals plotted from points 100 nm apart, moving from C into Al in the direction of the arrow. The EDS signals indicate that the bright band between C and Al was an Fe-, Al- and O-rich secondary phase. The C phase (dark blue EDS spectrum) also contained O and Al, while the concentration of other elements in the Al region was below detection limits.

correspond to higher atomic-mass species. The bright band in the center of the structure thus appears to be a secondary phase of the Al 1350 alloy used in the composite, such as one rich in Fe, which is the highest-concentration constituent of Al 1350 after Al (up to 0.4% [141]). Indeed, the EDS line scan in Fig. 4.14(b) (purple spectrum) confirmed that the bright band was both Fe- and Al-rich.

EDS signals collected from the second region of interest were subjected to the MCR-LLM algorithm to enhance the low signal-to-noise ratio of the raw spectra and to identify unique phases. Fig. 4.15 presents the HAADF-STEM and TEM structure images (a–b, respectively) and EDS components and relative intensities along the line scan (c–d). Three constituent EDS signals were identified in the line scan. Each phase contained a strong Al- K_{α} signal around 1.5 keV. The C-rich

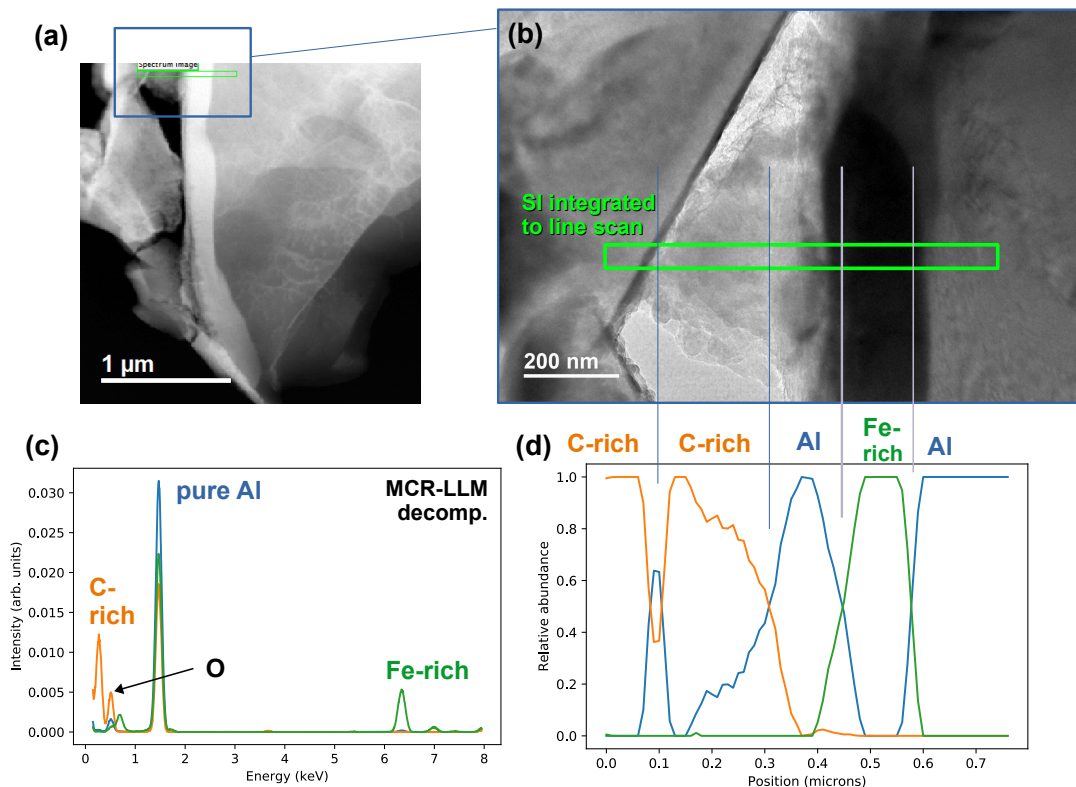


Figure 4.15: Structure and composition of the second EDS region of interest along the interface. (a) HAADF-STEM and (b) bright-field TEM images showed similar contrast features as EDS 1 (Figs. 4.13 and 4.14). A narrow spectrum image (SI) was collected from the green box and summed along the short dimension to improve signal-to-noise ratio. (c) EDS spectra of 3 phases identified in the SI by the MCR-LLM decomposition. Each contained a strong Al- K_{α} signal. The C-rich phase displayed C- K_{α} and O- K_{α} signals in addition to Al. The other two phases displayed no evidence of C and only weak O signals (in the case of Al, likely from an oxide passivation layer). (d) Normalized intensity profile of the three phases along the SI. Al and C overlap only in the thinner region to the left of the Fe-rich intermetallic band.

phase displayed prominent C- K_α and O- K_α signals in addition to Al, while neither of the other two displayed evidence of C; the Fe-rich phase was predominantly Fe and Al, and the “pure Al” phase contained only a weak O signal in addition to Al—which is to be expected, given the rapid formation of an oxide passivation layer on Al exposed to air and the small thickness of the specimen. The normalized intensity profile (Fig. 4.15(d)) shows some overlap between C and Al signals to the left of the Al/Fe secondary phase. This region therefore could contain the sort of Al/C interface structures expected to give rise to enhanced conduction properties. However, the uniformly ≈ 200 nm-thick band of Al/Fe intermetallic appears to have blocked longer-range interaction between the C and Al.

A subsequent covetic sample exhibited similar intermetallic and oxide features. The cross-sectional TEM specimen was prepared by FIB from a region displaying strong graphitic Raman spectra. A composite low-magnification TEM image shows the entire lamella in Fig. 4.16. The lamella comprised distinct C and Al phases separated by an interfacial band in the center. Close inspection of the carbon phase indicated that it is graphitic. Selected-area electron diffraction from region of interest 1 and HRTEM imaging (with corresponding Fast Fourier Transform) of region 2 indicated that the lattice spacing was in the range of 0.337–0.339 nm, which corresponds to the (0001) interplanar spacing of graphite (Fig. 4.17). Graphitic ordering was again strongest in the (0001) out-of-plane direction, as with the previous covetic structure shown in Fig. 4.9. The aligned contrast features visible on the left-hand side of the TEM image in Region 1 indicate that the atomic planes of carbon were

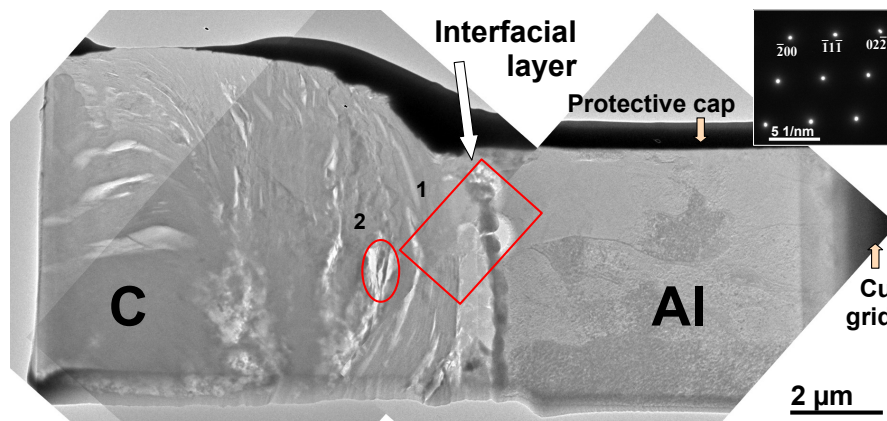


Figure 4.16: Composite bright-field TEM image of cross-sectional TEM specimen cv20190502, which consisted of distinct Al and C phases separated by an interfacial band. A protective tungsten cap was deposited before lamella extraction in order to limit amorphization damage effects from the ion beam. The two regions of interest marked 1 and 2 were investigated in further detail. The selected-area diffraction pattern was captured from the Al phase only.

well-aligned on a length scale of up to a micron, but nevertheless exhibited consistent small-scale undulations as seen in the HRTEM image of Region 2.

EDS composition analysis (Fig. 4.18) was performed on the interfacial band separating the C and Al phases shown in Fig. 4.16. The EDS data indicated that the C phase was pure and contained minimal O and Al signals, as was the Al phase, which exhibited only a weak $O-K_{\alpha}$ peak in addition to Al. The interfacial band visible in the STEM image was approximately $0.25 \mu\text{m}$ wide. Correspondingly, the full width at half-maximum (FWHM) of the $O-K_{\alpha}$ signal from the same region was $0.2 \mu\text{m}$. As with the two specimens of cv20190408, this interfacial oxide layer appears to have blocked the C phase from coming into contact with the Al matrix in the region of the sample from which the lamella was taken.

A portion of the Al matrix near to the interface was also imaged at high resolution, shown in Fig. 4.19, in an effort to identify any nanostructured C that

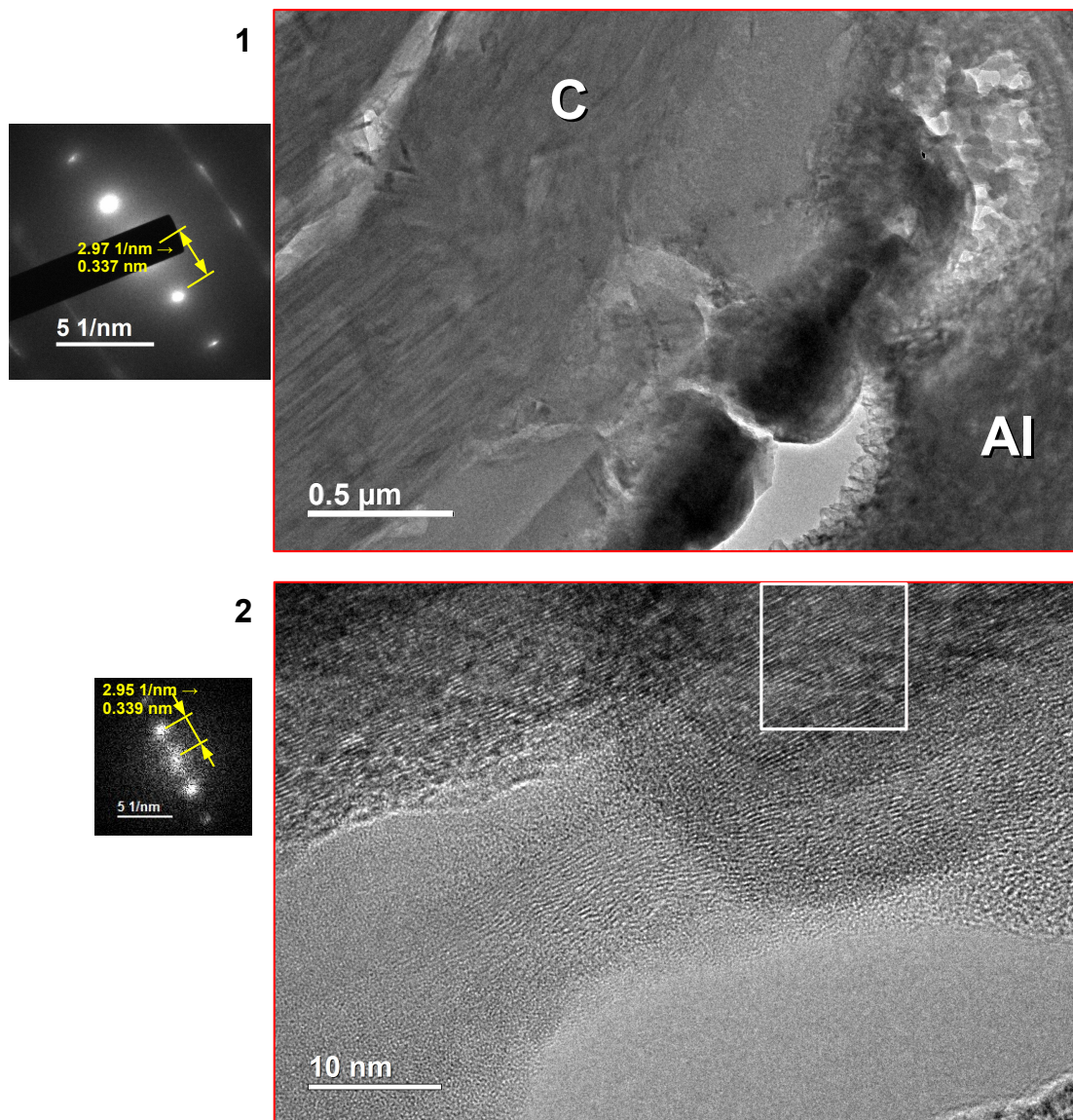


Figure 4.17: Closer inspection of the 2 regions of interest indicated in Fig. 4.16. Region 1: The selected-area diffraction pattern (left) was collected approximately from the left side of the image (right), in the area where banded contrast features are visible in the carbon phase. The reciprocal of the \mathbf{g} -vector magnitude between primary diffraction peaks matches the interplanar spacing of graphite at 0.34 nm. Region 2: The HRTEM image and associated Fast Fourier Transform pattern (left) generated from the white box confirms the presence of graphitic ordering.

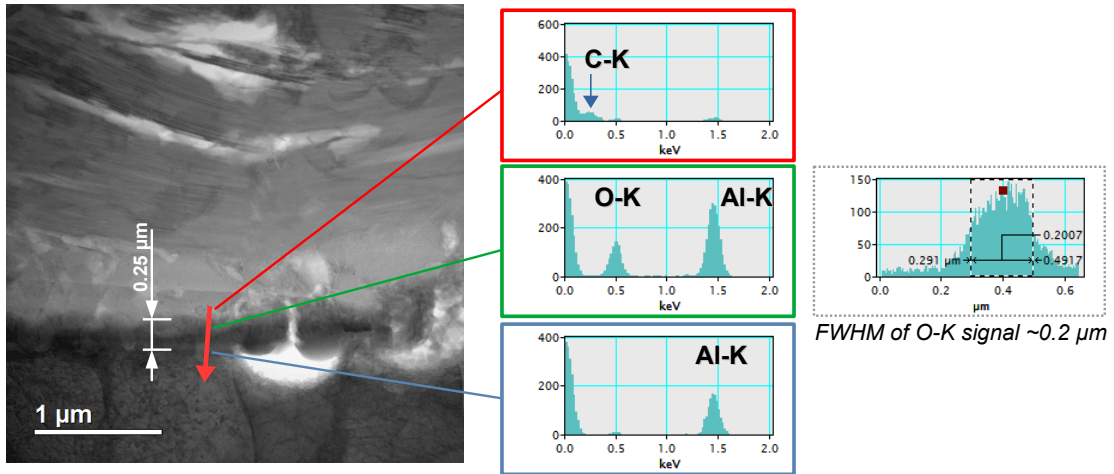


Figure 4.18: STEM-EDS line scan across the Al/C interface region. Left: Bright-field STEM image with the red arrow indicating the line-scan direction across the interface. The dark interfacial band was approximately $0.25 \mu\text{m}$ wide. Right: Selected EDS spectra from representative areas of the scan within the C- (red outline), O- (green), and Al-rich phases (blue). The full width at half-maximum (FWHM) of the O- K_{α} signal was about $0.2 \mu\text{m}$, corresponding to the width of the dark band in the STEM image.

might have been incorporated in it. The Al was locally thinner in this region, and therefore was affected proportionally worse by FIB amorphization damage (mostly confined to the top quarter of the image). The interplanar spacing in the most ordered crystalline direction was 0.231 nm , which matches the $\langle 111 \rangle$ direction in FCC Al. The crystallites were oriented on a $\langle 110 \rangle$ zone axis but with many slight rotations off-axis, which gave rise to additional spots in the FFT pattern and to defects indicated by the inverse FFT. Two weak spots in the FFT indicated similar distance in real space to the interplanar spacing of graphene; however this was not captured on a larger scale by an electron diffraction pattern such as the inset to Fig. 4.16, indicating that C incorporation within the Al lattice was either limited to a short distance from the interface or that the concentration of C in question was too low to produce noticeable diffraction peaks.

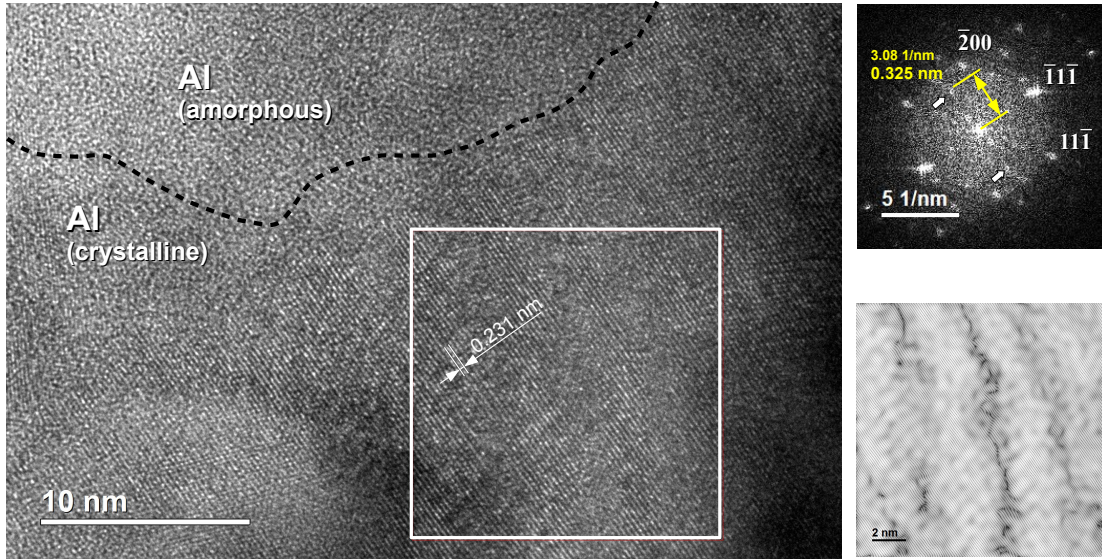


Figure 4.19: HRTEM of the Al structure near the interface with C (out of frame, to the top and left). The thinnest part of the Al was amorphous in that region, most likely due to FIB damage and not the covetics reaction. Within the crystalline Al, the zone axis was $\langle 110 \rangle$ as indicated on the FFT pattern on the top right (generated from the white box). Several additional weak spots were also visible, including one pair marked by arrows that matched the interplanar spacing of graphite. Local mis-orientation and texturing was visible in the inverse FFT image generated using the $\bar{1}\bar{1}\bar{1}$ spots of Al.

4.2.3 Well-integrated carbon nanostructures in Al covetics: Analytical TEM-EELS

Analysis of the carbon structures described in the previous section raises as many new questions as it answers. On the one hand it is apparent that graphitic ordering takes place during the covetics fabrication process, because the carbon source material is disordered and amorphous before the reaction, and no graphitic structures were found by Raman spectroscopy or TEM in the reference samples from the original alloy material. Furthermore, variable but persistent gains in bulk electrical conductivity have been reported in Al covetics [140]; these are not explained by micron-scale inclusions of graphite, whose bulk conductivity (2×10^6 S/m [32]) is

lower than that of pure Al (3.5×10^7 S/m). The main question is, therefore: What forms of nanostructured carbon are responsible for the bulk properties observed?

One early covetic Al 6061 alloy sample, known by its manufacturer-assigned reference number H49, has outperformed nearly all other covetics in terms of relative conductivity enhancement—from 15% after heat treatment up to over 40% in the as-extruded condition [57]. This sample also exhibited significant integration and epitaxy of graphitic nanoribbons in the Al lattice, on a length scale of over 1 μm [56]. Such structures are the best explanation of its conductivity properties especially in light of the conductivity modeling described in Sec. 4.3 of this work. In this section, new HRTEM and EELS results from sample H49 are presented and contrasted with more recent covetics structure findings.

Several TEM specimens of H49 had been previously prepared by electropolishing prior to this work. One of these (known to the research group as “#3”, reflecting the original sequence of preparation) was re-visited using analytical TEM and EELS in order to identify new features of interest using more precise data-analysis methods such as NMF. Fig. 4.20 presents a visual summary of the results. At low magnification in Fig. 4.20(a), several rod-like structures over 1 μm long are visible connecting 2 distinct Al grains. Inspection at higher resolution in Fig. 4.20(b) shows that these are about 20 nm wide, and exhibit spots and rings in the diffraction pattern matching the $\langle 10\bar{1}0 \rangle$ and $\langle 11\bar{2}0 \rangle$ interplanar spacings in graphite (Fig. 4.20(d)). Crucially, EELS spectrum imaging indicated that the structure exhibited 2 principal components of the C-K EELS edge (Fig. 4.20(e-f)). π^* and σ^* peaks were present in both components.

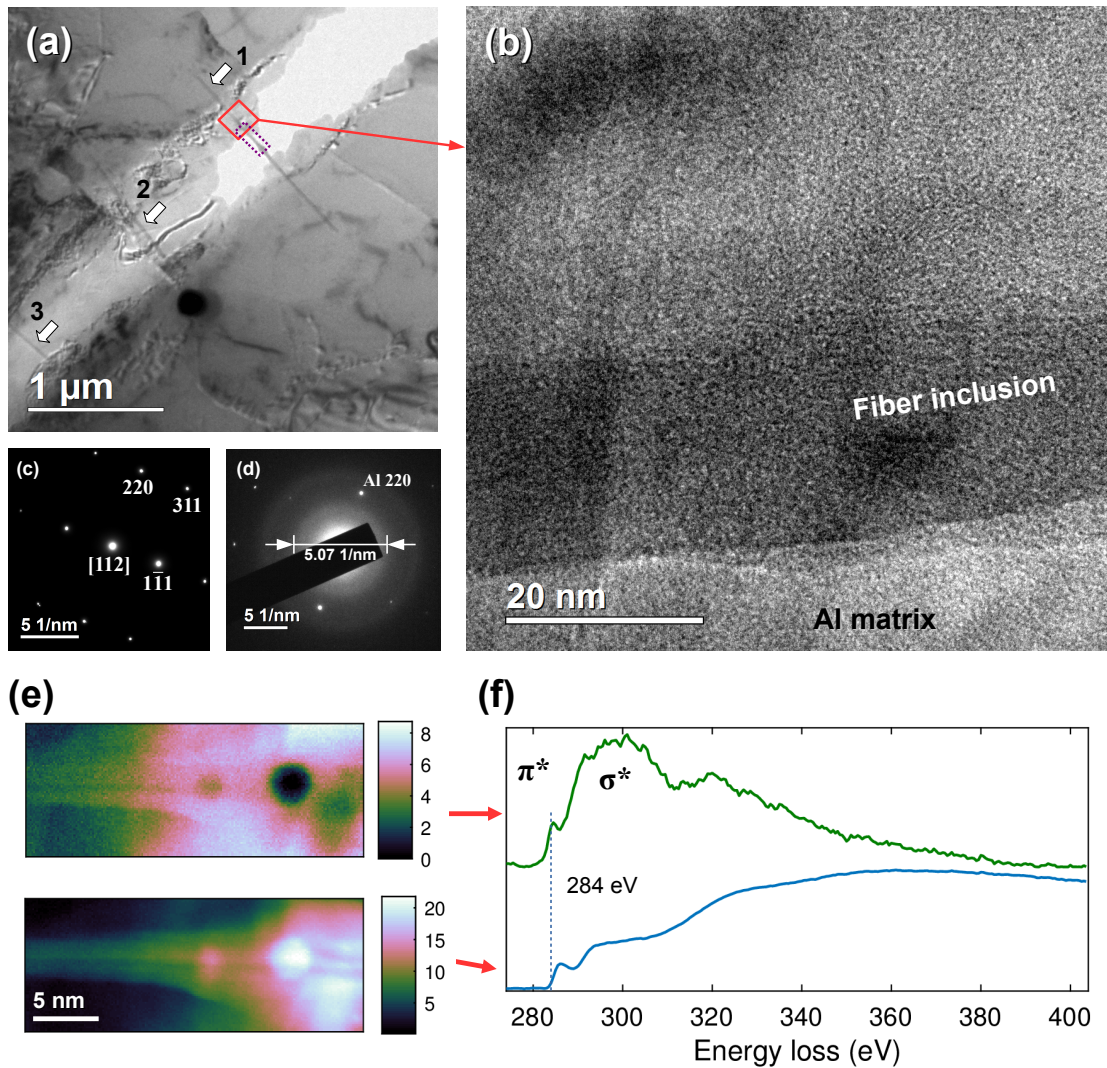


Figure 4.20: TEM and EELS of rod-like graphitic structures in electropolished Al 6061 covetic #3. (a) Bright-field TEM image of a gap between 2 Al grains bridged by 3 rod-like structures (numbered and indicated by arrows). (b) HRTEM reveals a crystalline Al matrix closely integrated with the fiber structure. (c) Electron diffraction pattern from the Al matrix, oriented such that the electron beam imaged along a $[112]$ zone axis. (d) Diffraction pattern from the region of the fiber inclusion. Spots corresponding to the Al $\langle 220 \rangle$ directions are visible. The inner and outer rings correspond to distances of 0.197 and 0.121 nm, respectively matching the $\langle 10\bar{1}0 \rangle$ and $\langle 11\bar{2}0 \rangle$ interplanar spacings in graphite. (e) NMF decomposition identified two significant components with intensities distributed as shown. (f) The corresponding components of the C-K EELS edge each displayed a π^* peak associated with sp^2 bonding character.

Inspection of the C-*K* edges' energy loss near-edge structure (ELNES) provides further insight into the bonding character of atomic C. sp^2 hybridization contributes a characteristic π^* peak around 284 eV, whereas both sp^2 and sp^3 bonding gives rise to the edge onset around 290 eV (σ^*) [142]. Intensity ratios of these peaks can be used to estimate the degree of sp^2 character in a particular region, relative to a reference such as highly oriented pyrolytic graphite (HOPG) [142,143]. Qualitative inspection of the blue curve in Fig. 4.20(f) therefore indicates that the center of the fiber, as shown in the lower map in (e), has a stronger sp^2 character than the periphery (upper map; green curve). This observation is consistent with the concept that graphitic (i.e., sp^2) ordering took place during the covetics fabrication process, with the later addition of a hydrocarbon contamination layer or other source of C with a weaker sp^2 character.

TEM imaging of the specimen was also performed along a $\langle 111 \rangle$ zone axis of Al near the rod-like features. Diffraction patterns and conventional dark-field imaging indicate that ordered graphitic ribbons were present, similar to those previously reported by Jaim et al. [56]. These data are shown in Fig. 4.21. In addition to the $\{220\}$ spots of Al, distinct secondary peaks are visible in the diffraction patterns throughout the specimen (insets of (a) and (b)). These correspond to $d = 0.204$ nm and $d = 0.211$ nm respectively, which match the $\langle 10\bar{1}0 \rangle$ spacing in the basal plane of graphite. Conventional TEM dark-field imaging (Fig. 4.21(c)) was also performed using the signal from one of these diffraction spots, circled in (b). This image showed a series of parallel graphitic ribbons roughly 20 nm wide and hundreds of nm long linking 2 adjacent Al grains. Such structures were visible throughout the electron-

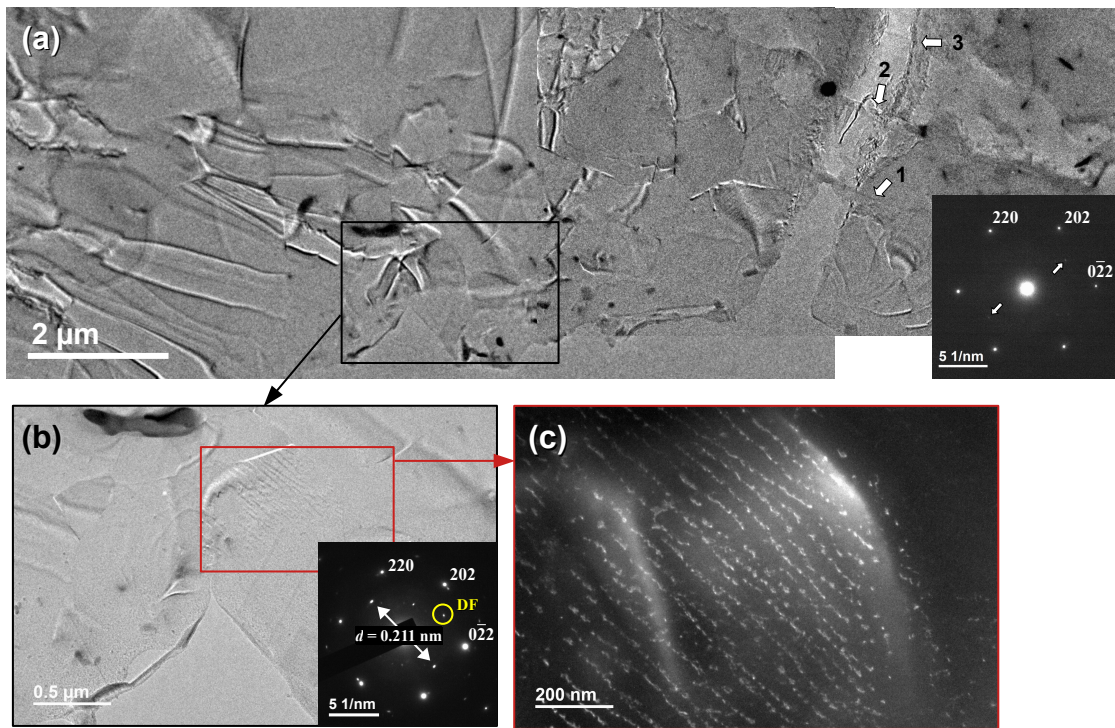


Figure 4.21: TEM imaging of aligned GNRs near the C fiber structures along a $\langle 111 \rangle$ zone axis of Al. (a) Composite bright-field image showing the thin perimeter of the electropolished specimen. The C fiber structures introduced in Fig. 4.20 are visible on the right, labeled 1, 2, and 3. (Inset: corresponding Al diffraction pattern with additional weak spots marked by arrows, indicating an interplanar distance of 0.204 nm.) (b) Bright-field TEM image showing banded features across 2 Al grains. Inset: Al $\langle 111 \rangle$ electron diffraction pattern with 4 secondary spots corresponding to $d = 0.211$ nm, which matches the $\langle 10\bar{1}0 \rangle$ spacing in graphite. (c) Dark-field TEM imaging using the graphitic diffraction spot indicated “DF” in (b) revealed a series of aligned ribbons about 20 nm wide and several hundred nm long.

transparent regions of the specimen and—to the extent that graphene nanoribbons provide enhanced electrical conduction pathways in the composite—give the best explanation for this sample’s exceptional conductivity properties.

4.2.4 Dislocation structure, microstructure, and mechanical properties of covetics

Dislocation structure and microstructure are known to significantly influence both mechanical and electrical behavior of Al alloys [144]. These aspects of covetics were investigated using TEM and other methods through collaboration between UMD and the U.S. Army Research Laboratory (ARL). A series of covetic samples prepared by UMD were subjected at ARL to micro- and nanomechanical testing to determine hardness, ultimate tensile strength, and local contact resistance; after these tests a subset of the samples were characterized using the TEM techniques featured in this thesis, including energy-filtered TEM and dark-field imaging, to explore the defect structures of covetics.

Al 1350 covetic samples were subjected to nano-indentation with the goal of validating molecular dynamics simulations of graphitic C structures embedded in Al [145]. The inclusion of graphene nanoribbons in a metal matrix was expected to influence the composite’s mechanical properties (e.g. tensile or yield strength). Rectangular arrays of spherical nano-indentations on the order of 100 nm deep were imposed across a grain boundary on a polished surface of the covetic sample known as “29A.” This array is shown in Fig. 4.22(a). A cross-sectional TEM specimen

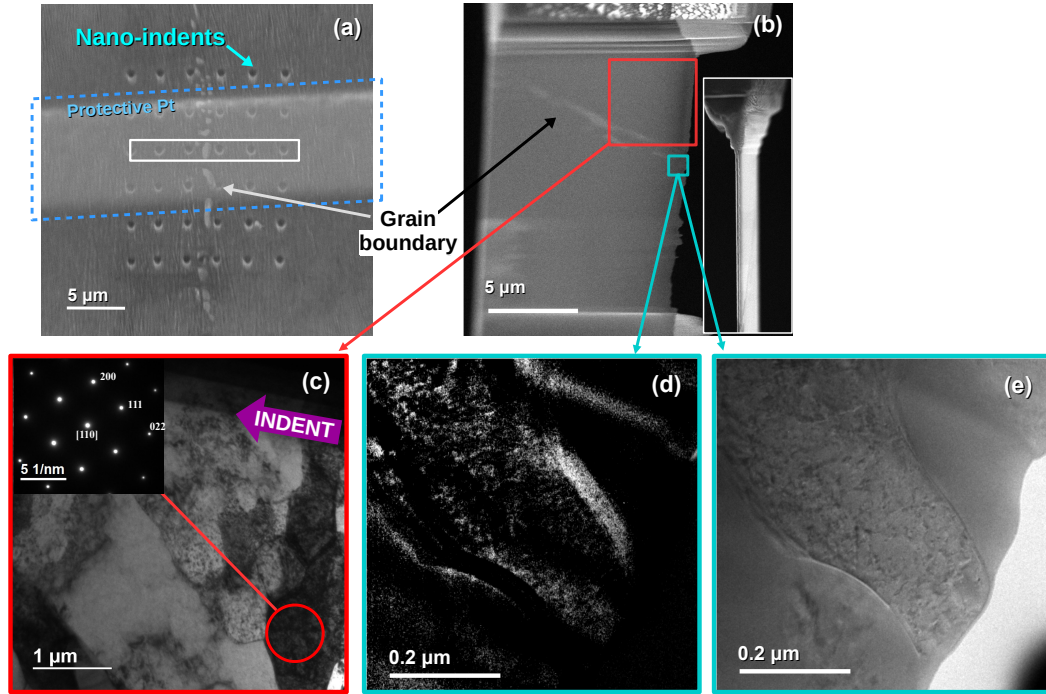


Figure 4.22: Characterization of the covetic sample 29A after nano-indentation. (a–b) The cross-sectional lamella was extracted from the region highlighted in the white box in (a), after deposition of a protective Pt capping layer, and thinned to ≈ 90 nm thick. (c) High-contrast image of one Al grain revealed that it was composed of several smaller, closely-oriented ≈ 1 - μm grains. (d) Energy-filtered TEM image of the grain boundary region generated using electrons from the energy loss range matching the C-K EELS edge. C signals were visible in the grain boundary region as shown and not elsewhere in the specimen. (e) Zero-loss EFTEM image corresponding to (d).

(Fig. 4.22(b)) was prepared by FIB from the indicated region in order to capture the area under the indent array from both sides of the grain boundary. Each of the two grains exhibited a single unique electron-diffraction pattern, corresponding to $(1\bar{1}1)$ and (011) on the left and right sides of the grain boundary in Fig. 4.23(a), respectively. As seen in the bright-field image in Fig. 4.22(c), however, these grains were highly textured and ultimately composed of several smaller, highly-oriented grains. Inspection of multiple electron diffraction patterns within the (011) -oriented grain revealed sub-grain misorientations of typically 2 – 3° . This fine-grained struc-

ture matches the report of paracrystalline behavior previously observed via electron backscatter diffraction (EBSD) which is often correlated with large dislocation densities [145]. Similar fine-grained features were also observed in a TEM specimen extracted far away from the indent array, indicating that these features were a product of the bulk process and not mechanical testing. Energy-filtered TEM indicated the distribution of C around the grain boundary region in Fig. 4.22(d). Meaningful concentrations of C were not observed outside of this region.

Conventional TEM dark-field (DF) two-beam condition was used to enhance contrast between grains and dislocation features, and is summarized in Fig. 4.23(b). The DF image was generated from the $(1\bar{1}1)$ -oriented grain using the $\mathbf{g} = (022)$ diffraction spot. A high concentration of dislocations and low-angle grain boundaries are visible near the surface of indentation. The dislocation density under the indent region was estimated to be $2.3 \times 10^{14} \text{ m}^{-2}$ in the highest-density region bounded by the dashed blue box, roughly 2 orders of magnitude greater than in a typical sample of pure unstressed Al [146]. In comparison, the dislocation densities simulated by Shumeyko et al. were on the order of 10^{16} m^{-2} . The main reason for this discrepancy is the significantly smaller length scale of the molecular dynamics simulation (angstroms) compared to TEM (hundreds of nanometers to microns). Experimental limitations such as differences in FIB milling rates also led to uncertainty in the exact position of the final lamella relative to the indents—i.e., the lamella plane could correspond to the top or bottom edge of the white box in Fig. 4.22, not directly under indents, and represent a less-strained area. Furthermore, $\approx 50 \text{ nm}$ of the lamella top surface—expected to be the most defective

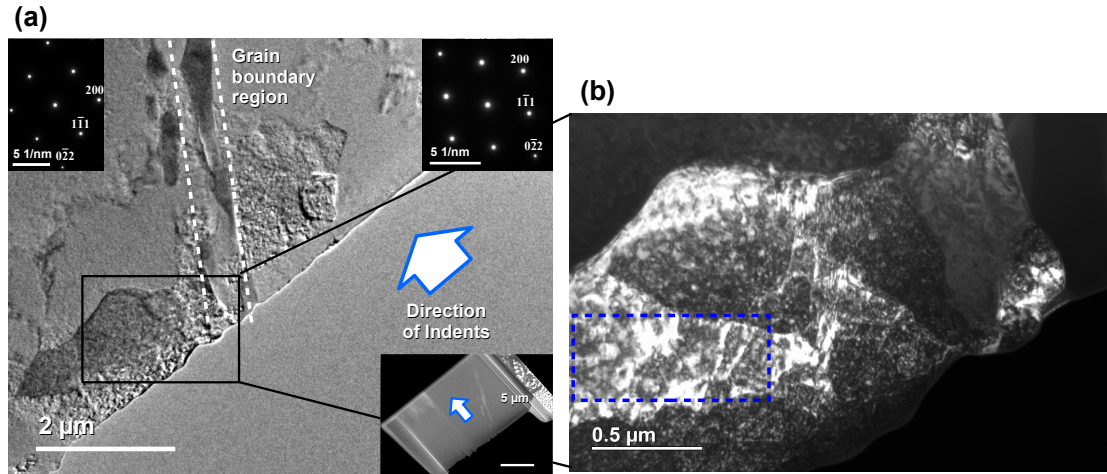


Figure 4.23: (a) Bright-field TEM image showing differently-rotated $\langle 011 \rangle$ grains on the left and right sides of the grain boundary, respectively. Indentation was performed in the direction indicated; the inset shows the TEM lamella with an arrow specifying the direction of nanoindentation. (b) TEM dark-field image from the outlined region in (a) using the $\mathbf{g} = (022)$ diffraction spot. Several low-angle grain boundaries were visible and the dislocation density was estimated to be $2.3 \times 10^{14} \text{ m}^{-2}$ in the area outlined in the dashed blue box.

area after indentation—was damaged or removed during the final FIB milling step. For this reason the dislocation density values reported from experiments should be considered low-range estimates.

It is encouraging for the concept of mechanical-property enhancement that GNR distribution in simulated Al covectics is correlated with different dislocation density and propagation behavior, which lends credence to the principle that GNRs block dislocation motion within the metal matrix and lead to increased strength and hardness [145]. TEM dislocation-density estimates support this concept, as the dislocation density away from the indents in the covectic 29A was about $1.3 \times 10^{14} \text{ m}^{-2}$, lower than the $1.7 \times 10^{14} \text{ m}^{-2}$ seen in an Al 1350 control subjected to the same metallurgical treatment. This implies that the propagation of dislocations away from the indent region may have been blocked more effectively in the covectic

than in the control, and is a promising first step towards a larger body of results to corroborate models; however, this difference is not itself statistically significant, and further work is needed in this area.

Similar defect structures between covetics and controls

Further characterization of mechanical properties was conducted at larger scales to assess whether these differed between covetic composites and reference Al alloys (i.e. controls—without the addition of C but otherwise subjected to the same melt/cool cycle and treatment). The importance of this topic was twofold: First, since graphitic structures are known for their high tensile strength and other mechanical properties, the inclusion of these materials could provide a pathway to enhanced strength of the composite. Second, even if a certain application calls only for high electrical conductivity, with no particular concern for mechanical behavior, it is important to understand the effect of microstructural features such as grain size on the conductivity of covetics, in order to separate it from enhancements due to the introduced carbon.

Previous research on traditional (non-covetic) Al6061 alloys shows a clear relationship between increased annealing temperature, decreasing yield strength, and increasing electrical conductivity (Zhang et al. 2018, Fig. 9 [144]), a straightforward demonstration of the concept that a higher density of structural defects (e.g. grain boundaries and dislocations) increases the difficulty to propagate both dislocations and electrons through the metal structure. By contrast, “traditional” metallurgical

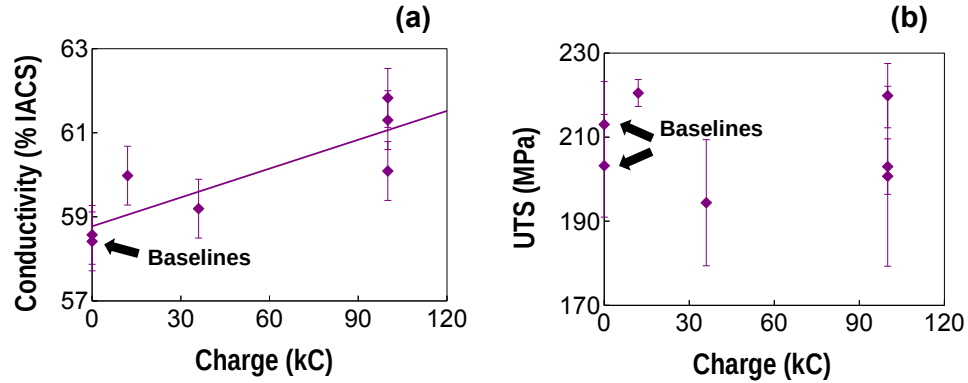


Figure 4.24: Trends in covetics' (a) electrical conductivity and (b) ultimate tensile strength as functions of total charge applied through the melt during fabrication (i.e., current \times reaction time, in kilo-Coulomb (kC) units). While the conductivity tended to increase with total charge, no corresponding decrease in UTS was discerned, suggesting that the conductivity increases were not simply due to reduction in dislocation density or other changes in defect structure. Original data were collected by S. Zhang of General Cable [140].

structure interpretations do not explain the increased electrical conductivity in covetics. A side-by-side comparison of the electrical- and mechanical-property trends in several covetic samples, Fig. 4.24, shows how the conductivity tended to increase with total charge applied during the fabrication process, but no corresponding decrease in UTS was observed, as one would expect if the conductivity increase had been due solely to reduced density of microstructural defects. Furthermore, the typical grain size of Al 1350 covetics as determined by optical micrographs of etched surfaces were similar to an Al 1350 control (Fig. 4.25.) Taken all together, bulk mechanical property characterization shows that Al 1350 covetics' hardness, ultimate tensile strength, and grain size distributions do not differ significantly from the parent alloys subjected to the same processes. Because the inclusion of C does not alter the bulk Al microstructure, direct comparison of electrical conductivity between covetic samples and parent-alloy control samples is permissible.

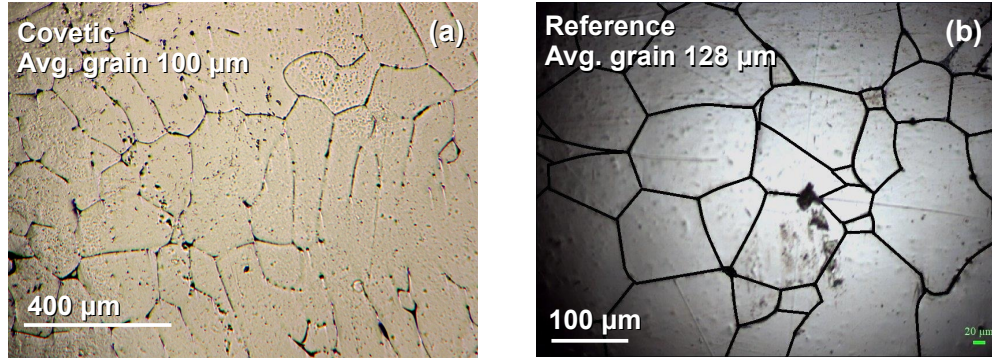


Figure 4.25: Optical micrographs indicated that the typical grain sizes of (a) the Al 1350 covetic and (b) the control were not substantially different. A direct comparison of electrical properties is therefore reasonable, because resistance due to electron grain-boundary scattering will be comparable in both materials.

4.3 Effective medium model of electrical conductivity

A simple model of NCMC conductivity based on fundamental principles will be important to fill gaps in understanding regarding conductivity enhancement in covetics—especially considering the many different forms and structures that carbon can take when embedded in a metal matrix. Significant uncertainties have persisted regarding the magnitude of conductivity enhancement in NCMCs such as the Al covetics characterized in this work. Early reports on a 3 wt.% C-Al6061 covetic suggested conductivity enhancement of 43% and 15% above the reference Al6061 in the as-extruded condition and following T6 heat treatment, respectively [57]. In contrast, investigations of covetics based on other metals such as Cu and Ag have shown much less or no improvement [147], and extensive measurements of as-cast Al 1350 covetics have produced increases in conductivity in only the 0–5 % range [140]. Furthermore, large variations and uncertainties in the measurement

also arise depending on the specimen aspect ratio and surface treatment [57]. As such, there remains a great deal of uncertainty regarding electrical conductivity enhancement in composites: the magnitude of increase in bulk samples, the fabrication and metallurgical processing treatments which affect it, the nature of the nanoscale structures which enhance or inhibit conductivity, and what the maximum increase in conductivity might be under ideal conditions.

4.3.1 The need for a new model

The rule of mixtures provides a simple starting point to understand the conductivity of an Al-matrix composite with embedded graphitic inclusions. Provided that the inclusions are uniaxial and aligned, this model approximates the effective conductivity of a composite, σ_e , as a volume-weighted average of the conductivities of the matrix (σ_m) and inclusions (σ_f). The conductivity is bounded by the minimum, set by the case of a load (i.e., a voltage) applied transverse to the inclusions (Reuss model, [148]) and the maximum set by the case of a load along the inclusion axis (Voigt model, [149]):

$$\left(\frac{f}{\sigma_f} + \frac{1-f}{\sigma_m} \right)^{-1} \leq \sigma_e \leq f\sigma_f + (1-f)\sigma_m \quad (4.2)$$

where f is the inclusion volume fraction.

The electrical conductivity of Al 1350 and similar alloys is about 3.5×10^7 S/m. This value is larger than conductivities reported for graphitic structures such as ideal pure graphite ($\approx 2 \times 10^6$ S/m, [32]) or even suspended graphene ($\sigma = ne\mu = 2.2 \times 10^7$

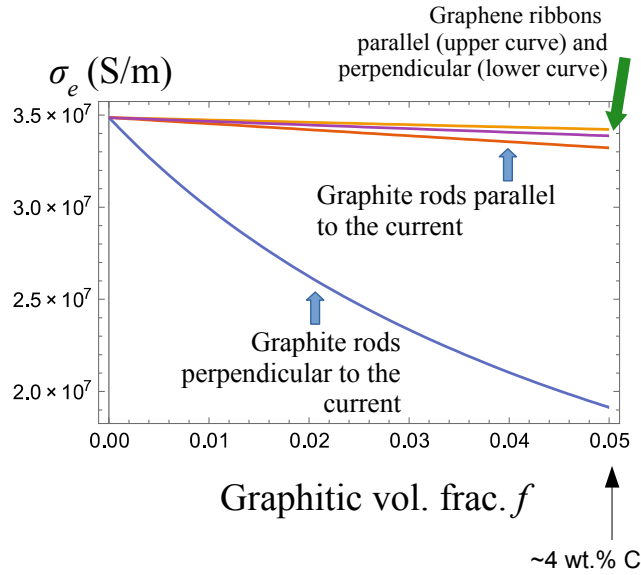


Figure 4.26: The projected conductivity σ_e of nanocarbon-Al composites following the rule of mixtures decreases monotonically, whether the inclusions are graphite (σ bounded by the lower 2 curves) and suspended or non-interacting graphene (σ bounded by the upper 2 curves). This simple model is contradicted by measurements showing conductivity increases in covetics, indicating that a more sophisticated model is needed.

S/m, [34]). Therefore, σ_e will always be smaller than σ_m for any volume fraction of carbon f greater than zero, as shown in Fig. 4.26, as long as the assumptions implied by the rule of mixtures are valid—namely, that the inclusions and the matrix are non-interacting. This assumption appears *not* to be valid for covetics because many samples have shown conductivity enhancement. These samples serve as evidence that metal-carbon interaction such as charge transfer is present in covetics, and that this interaction serves to enhance their conductivity. A more sophisticated model is needed to accurately represent the effective conductivity of covetics.

A 2004 theoretical study by Hjortsam and co-workers sought to demonstrate the high-conductivity potential of carbon-metal composites [150]. Their effective medium model suggested that the effective conductivity of an aligned single-wall

CNT (SW-CNT)-Cu system could be a factor of 2 greater than the International Annealed Copper Standard (IACS) conductivity, with a volume fraction of 30–40% SW-CNT. Such a large magnitude of projected conductivity enhancement is promising. However, obtaining this result required simplifications that are not physically realistic. Hjortsam et al. neglected the existence of a percolation threshold, the critical volume fraction above which inclusions are likely to form long-range interactions. The percolation threshold is substantially lower than 40% for elongated inclusions: it drops below 1% for aspect ratios between 50 and 100 [151]. Secondly, metal-carbon interfaces were treated as ideal and non-interacting, which is not likely for a moderately reactive metal such as Al.

4.3.2 Structural inputs to the model

The effective medium approximation (EMA), introduced in Sec. 2.4, forms the basis for the model developed in this section. Previous studies have utilized EMA to estimate the effective properties of composites containing nanostructured C [152]. A number of experimental reports relate to an insulating matrix such as a polymer with embedded CNTs, showing enhancement of thermal conductivity and hardness [153, 154].

The effective-medium approach in the present work incorporates several key modifications to that of Hjortsam, in order to reflect the structure of covectics as it is understood thus far, and to bridge the remaining knowledge gaps in a rigorous

way using theoretical and computational approaches. Two key assumptions were as follows:

1. Graphitic structures are randomly oriented

Previous TEM investigations of covetics at the nanoscale, such as the work by Jaim [56] and in Sec. 4.2.3 of this thesis, suggest local orientation of GNRs on the Al (111) crystallographic planes. However, the casting and/or furnace cooling process produces a polycrystalline metal matrix. A macroscopic piece of covetic composite will therefore have randomly aligned grains, unless it has undergone a process that imparts directionality, such as extrusion. This randomness implies that embedded graphitic structures will also be randomly oriented on a macroscopic scale, independent of the carbon structures' degree of alignment within individual grains. A schematic illustrating the orientation of GNRs in two adjacent metal grains is shown in Fig. 4.27. Some experiments have even found significantly smaller average grain sizes in covetics than in parent 6000-series Al alloys [155, 156], which would contribute further to the random orientation of carbon structures within the bulk composite.

2. Graphitic carbon takes the form of multi-layer graphene ribbons

The multi-layer nature of GNRs in covetics was identified using Raman spectroscopy as discussed in Sec. 4.1.2. Most GNRs appeared to contain between 3 and 10 layers. The thickness of the embedded graphene nanoribbons will have a substantial negative effect on their ability to provide a composite with enhanced electrical

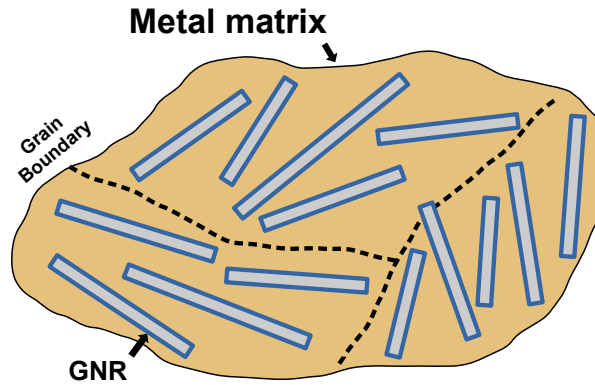


Figure 4.27: Schematic representation of GNRs embedded in a polycrystalline metal matrix. Even while the nanoribbons are locally aligned within one grain or across a grain boundary, they are treated as randomly oriented across macroscopic length scales as a consequence of the metal grains' random orientations with respect to one another. This assumption is valid as long as orientation is not introduced in a subsequent processing step, e.g. extrusion.

properties. Fundamentally, thick graphene is analogous to graphite, whose electrical conductivity is worse than many transition metals [157]. The c -axis electrical [158] and thermal [159] conductivities of graphite are lower than their corresponding in-plane values owing to weak van der Waals bonding between the layers. Furthermore, when graphene is doped by interaction with a substrate leading to a shift in the Fermi level, as described in Sec. 1.2.1, this interaction only affects the layer next to the substrate [160]. It is therefore desirable that GNRs be as thin as possible (single- or bilayer). This effect is addressed in the present work by introducing an effective volume fraction parameter to consider only the top and bottom monolayers of GNRs as contributing to enhanced conductivity.

4.3.3 Electronic inputs to the model

The Cu-CNT model put forth by Hjortsam et al. [150] rests upon the assumption that the matrix and inclusions each retain their original electronic properties when formed into a composite. Experimental findings and calculations indicate that this is not the case in a metal-GNR system, where electronic interactions between the metal matrix and graphitic inclusions lead to enhanced conductivity at these interfaces. In addition, quantization of electron energies in narrow graphene ribbons leads to a conductivity that is dependent on the GNR width, which must be taken into account in order to build a representative model.

4.3.3.1 Charge transfer at the metal-graphene interface

In the work of Cao et al., first introduced in Sec. 1.2, conductive atomic force microscopy (c-AFM) measurements were taken from metal-graphene layered structures with varying numbers of graphene layers from 1 to 20 [44, 45]. It was demonstrated that the conductivity of graphene embedded in Cu was up to 3 orders of magnitude greater than the matrix, up to 7.1×10^{10} S/m [44], but only for single- or bilayer graphene. Increasing the number of layers caused the peak current measurement to drop precipitously, which suggested that the conductivity enhancement was closely confined to the interface. The authors attributed this trend to the mechanism of charge carrier transfer from metal to graphene, which has been theoretically predicted in Cu, Al, and other metals [42, 43, 161]. Follow-up density-functional theory (DFT) calculations by Cao et al. support this mechanism, predicting electron

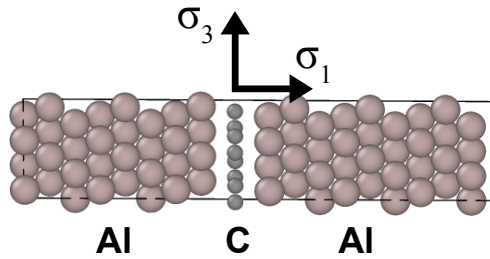


Figure 4.28: Structure of the simulated Al–GNR–Al interface with a single-layer graphene ribbon (gray) bounded on both sides by Al(111) oriented crystals (brown), used for carrier density calculation and the estimate of out-of-plane vs. in-plane GNR conductivity σ_1/σ_3 .

densities on the order of 10^{14} cm^{-2} in bilayer graphene embedded in either Cu [44] or Al [45].

In collaboration with Andrew Palughi of Texas A&M University, first-principles DFT calculations were used to estimate the charge carrier concentration n of a graphene sheet embedded in Al, as well as the ratio of the electrical conductivity normal to the plane of the GNR relative to in-plane, σ_1/σ_3 . All calculations were performed using the Vienna Ab Initio Simulation Package (VASP) [162, 163]. The system consisted of a single layer of graphene placed on the (111) crystallographic plane of FCC aluminum, with 17 Al layers in total, as illustrated in Fig. 4.28. The magnitude of charge transfer was obtained via electronic structure calculations. On average, $0.045e$ per 2-atom graphene unit cell were transferred from the metal to the GNR, which translated to a carrier density n of $1.7 \times 10^{14} \text{ cm}^{-2}$. The ratio of out-of-plane to in-plane GNR electrical conductivity, σ_1/σ_3 , was obtained using the implementation of the Boltzmann transport equations in the BoltzTrap2 package [164]. This ratio was on the order of 10^{-5} , so the conductance normal to the plane of graphene is negligible.

4.3.3.2 Width dependence of GNR conductivity due to quantum confinement

Some of the unique electronic properties of graphene are attributed to its constrained geometries. In addition to the characteristic two-dimensional electron gas behavior, conductance in graphene nanoribbons is subject to quantum confinement; due to their narrow width, the ribbons act as electron waveguides and propagating electrons' energies are quantized. This phenomenon has been explored experimentally [160] as well as theoretically [165, 166]. Wider GNRs are ultimately able to support more electron-wavefunction states and therefore exhibit higher conductivity than narrow ribbons. This conclusion is supported by the following two cases of a quantum-conductance model.

Simplified case: An isolated GNR as an infinite potential well

The analysis of Naeemi et al. in Ref. [165] serves as a starting point for the present work. In the language of quantum mechanics, an isolated nanoribbon (for instance, suspended in vacuum) may be treated as an infinite potential well. Outside of the ribbon the electron wave function must be equal to zero, implying the transverse boundary condition $\sin(k_{\perp}W) = 0$, where W is the width of the ribbon. The corresponding allowed wavevectors are

$$k_{\perp} = \frac{n\pi}{W} \quad (4.3)$$

where n is an integer. The approximate dispersion relation is given by [35]:

$$E(\vec{k}) = \pm \hbar \nu_F |\vec{k}|, \quad (4.4)$$

where \hbar is the Planck constant h divided by 2π and ν_F is the Fermi velocity of graphene. This leads to the allowed energies E_n ,

$$E_n = \hbar \nu_F \left(\frac{n\pi}{W} \right) = n \Delta E. \quad (4.5)$$

The energy level spacing $\Delta E = \hbar \nu_F / 2W$ is an inverse function of the GNR width [165]. This result shows the plausibility that a wider GNR is more conductive, because it allows a greater number of electronic wavefunctions.

The scattering behavior of different propagating electron modes is another way in which conductance depends on W . As discussed by Berger [160] and Naeemi [165], the mean free path of the n th mode l_n is also a function of W . Assuming that scattering at the edges is diffusive (corresponding to edge roughness greater than ≈ 1 nm [160, 165]), l_n is a function of the ratio between longitudinal and transverse wavevectors, k_{\parallel} and k_{\perp} respectively. Adapting Eq. 3 from Ref. [165]:

$$l_n = \frac{k_{\parallel}}{k_{\perp}} W = W \sqrt{\left(\frac{E_F / \Delta E}{n} \right)^2 - 1}, \quad (4.6)$$

where E_F is the Fermi energy. In other words, as k_{\perp} increases with n , electrons propagate progressively shorter distances l_n before scattering at the edges. The W dependence can be seen qualitatively in the illustration in Fig. 4.29. An expression

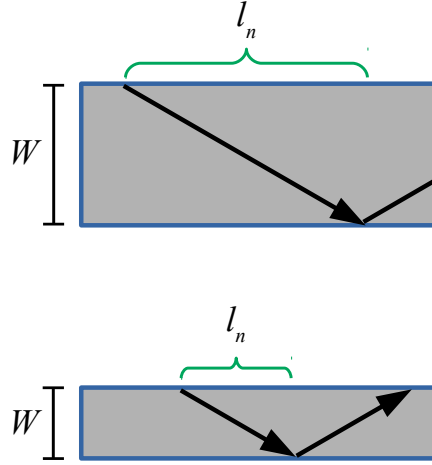


Figure 4.29: The electron mean free path due to edge scattering l_n is finite for all $n \neq 0$ as a consequence of the transverse wavevector k_{\perp} , which is non-zero except for $n = 0$. A wider graphene ribbon (top) is therefore able to accommodate a longer path length in the longitudinal direction than a narrow ribbon (bottom).

for the total conductance G is obtained by applying Matthiessen's rule, given by Ref. [165], Eq. 4 :

$$G = \frac{2e^2}{h} \sum_n \frac{1}{1 + L(1/l_D + 1/l_n)} \quad (4.7)$$

where $2e^2/h$ is the quantum conductance (hereafter defined as G_0), L is the GNR length, and l_D is the mean free path corresponding to defect and phonon scattering, independent of the edge scattering effects. Reported values of l_D range from 600 nm [160] to tens of microns in special cases, such as for 40 nm-wide GNRs epitaxially grown on SiC (16 μm , [49]) or graphene sheets encapsulated in hexagonal boron nitride (28 μm , [167]). l_D was assumed to be 1 μm for the purpose of this model [165]. The trends of Eq. 4.7 are illustrated in Fig. 4.30 for various n , W , and E_F .

Having identified a model for G in isolated GNRs, it is possible to estimate G for GNRs embedded in a metal matrix using a known value of the Fermi energy

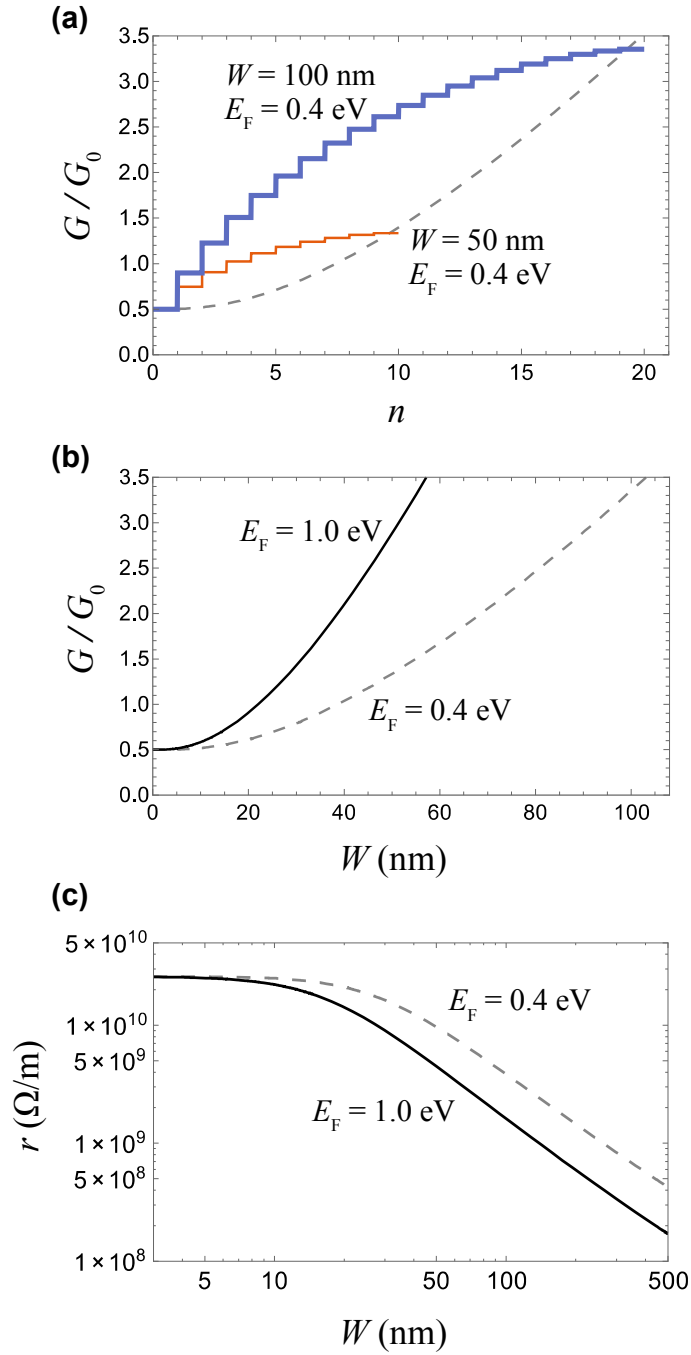


Figure 4.30: The effects of W and E_F on the conductance G of GNRs with $L = l_D = 1 \mu\text{m}$. (a) For a given $E_F = 0.4$ eV, G increases step-wise with the number of quantum modes n . Both the number of allowed modes and the magnitude of increase in G per additional mode increases with W , as illustrated by the stepped curves for $W = 50$ and $W = 100$ nm, respectively. The dashed gray line indicates the envelope of $G(W)$. (b–c) The increase of G with W is more pronounced with larger E_F ; the log-log plot in (c) presents the same curves in (b) in terms of the equivalent resistance per unit length, r .

E_F , which is related to the carrier density n via the 2D density of states function for graphene, as introduced in Sec. 1.2.1. Applying the $D_{2D}(E)$ expression in Eq. 1.2 to the definition of n :

$$\begin{aligned}
 n &= \int f(E)D(E)dE \\
 n &\approx \int_0^{E_F} D_{2D}(E)dE \\
 n &= \frac{E_F^2}{\pi\hbar^2\nu_F^2}
 \end{aligned} \tag{4.8}$$

Plugging in the carrier density $n = 10^{14} \text{ cm}^{-2}$ for the graphene/Al system estimated via DFT by Cao et al. [45], a value of $E_F = 1.2 \text{ eV}$ is obtained. This value is larger than those presumed by Naeemi et al. [165], however it is not beyond the realm of possibility; Fermi energies on the order of 1 eV have been experimentally observed in systems with “ultrahigh” carrier densities of around 10^{14} cm^{-2} [38,168], which would be expected to produce conductivities increasing with W similar to that illustrated in Fig. 4.30.

Modeling the metal-graphene interface as a finite potential barrier

Although it is a helpful starting point, the infinite potential well is a better approximation of an isolated or suspended GNR than one embedded in a metal matrix. Electrons in the embedded GNR will experience a finite energy barrier, V_0 , which is determined by factors such as the work functions of the metal (ϕ_M) and of graphene (ϕ_G), as well as the nature of the bonding interaction at the interface [43, 169, 170]. One interpretation for the magnitude of V_0 is the difference in

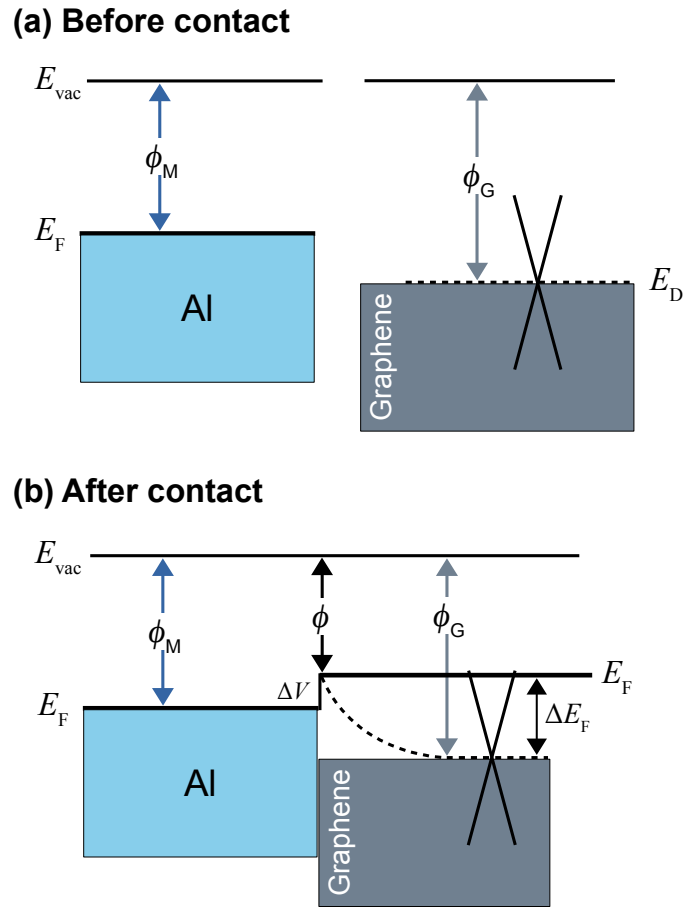


Figure 4.31: (a) Work functions of the isolated metal and graphene surfaces with respect to the vacuum level, E_{vac} . (b) Band bending at the Al-GNR interface. ϕ_M is the work function of the metal (4.24 eV for Al), $\phi_G = 4.6$ eV for pure graphene, and $\phi = 4.04$ eV for graphene adsorbed on Al. ΔV is a potential barrier at the metal-graphene interface defined by $\phi_M - \phi$ [43]. Adapted from Refs. [43, 161, 171].

work functions, $V_0 = \phi_M - \phi_G$, i.e., about $4.6 - 4.24 = 0.36$ eV, as illustrated in Fig. 4.31 [43, 170]. The height of the potential energy barrier between the metal and graphene—through which electrons must tunnel to enter and exit the graphene—can also be considerable. Using DFT, the height of this barrier has been estimated at 1.2 eV for Al with a corresponding transmission probability of 35% [172].

Consider a graphene nanoribbon as a finite potential well of width $W = 2a$, as in Fig. 4.32. The following solution is based on the standard approach employed in

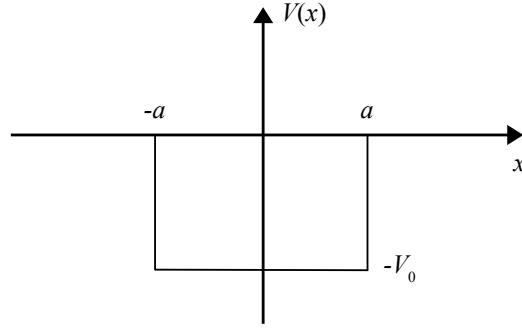


Figure 4.32: A finite potential well representing a GNR of width $W = 2a$.

many quantum mechanics texts [173]. The Schrödinger equation within the region $V = -V_0$ is given by

$$-\frac{\hbar^2}{2m} \frac{d^2\psi}{dx^2} - V_0\psi = E\psi, \text{ or} \quad (4.9)$$

$$\frac{d^2\psi}{dx^2} = -l^2\psi, \text{ where } l \equiv \frac{\sqrt{2m(E + V_0)}}{\hbar}.$$

V_0 is positive and $E < 0$ for bound states; a finite number of bound states are allowed for electrons with $E < V_0$, which take the form $\psi(x) = C \sin(lx) + D \cos(lx)$ within the well. Outside of the well, $\psi(x)$ takes the form of decaying exponential functions of the form $Be^{\kappa x}$, where $x < 0$, and $Fe^{-\kappa x}$ where $x > 0$. $\psi(x)$ is subject to the typical constraints that $\psi(x)$ and $d\psi/dx$ are continuous at the barrier walls, which gives rise to the condition that $\kappa = l \tan(la)$. Defining a change of variables where $z \equiv la$ and $z_0 = (a/\hbar)\sqrt{2mV_0}$, one obtains the transcendental equation

$$\tan(z) = \sqrt{(z_0/z)^2 - 1}, \quad (4.10)$$

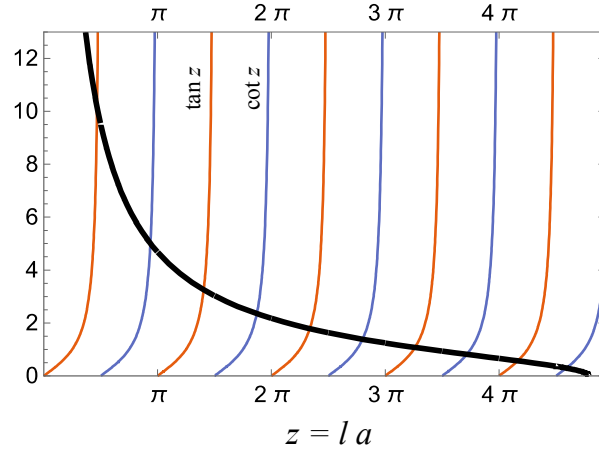


Figure 4.33: Graphical solution for electrons confined to a GNR of width $W = 50$ nm and potential well depth $V_0 = 0.4$ eV. The thick black line is the right-hand side of Eq. 4.10. Its intersections with the left-hand side, $\tan(z)$ and $\cot(z)$, provide the even and odd solutions, respectively. The vertical axis is dimensionless.

which may be solved numerically or graphically for the allowed values of z (and therefore the allowed wavevectors l). At this stage the dispersion relation $E(l)$ for graphene given in Eq. 4.4,

$$E + V_0 = \hbar\nu_F l, \quad (4.11)$$

is reintroduced. For the case where the well is “large” in terms of a and V_0 , the allowed wavevectors l_n and the bound-state energies are approximately as follows:

$$\begin{aligned} z_n \equiv l_n a &\approx \frac{n\pi}{2} \\ E + V_0 &\approx \frac{\hbar\nu_F n\pi}{2a}, \end{aligned} \quad (4.12)$$

where n is an integer. The graphical solution to this system shown in Fig. 4.33 indicates that this approximation is reasonable for $W = 50$ nm and $V_0 = 0.4$ eV (and therefore all larger W and V_0 [173]). The number of allowed states, 10, is

the same as for the simplified infinite-potential well case shown in Fig. 4.30(a) (the orange stepped curve with $W = 50$ nm and $E_F = 0.4$ eV). In terms of the number of allowed states and their contributions to the GNR conductance, therefore, the infinite-well case produces reasonable results. The principal difference in the finite-energy barrier case from the infinite-well case is that it is not possible to create an arbitrarily large number of states given an arbitrarily large Fermi level energy: If V_0 is an intrinsic parameter of the material system, it will impose a limit on the effect of E_F , because states where $E > V_0$ are scattering (continuum) states, not bound (quantized) states. Based on this result, a maximum Fermi energy of the tunneling barrier height for Al contacting graphene, 1.2 eV [172], will be considered the most reasonable within the context of the effective-medium model for the overall conductivity of Al-graphene composites developed in the following section.

4.3.4 The effective conductivity of a composite with randomly-oriented inclusions

An analytical expression for conductivity in such a system containing randomly-oriented rod-like inclusions is given by Ref. [91]:

$$\frac{\sigma_e}{\sigma_m} = 1 + \frac{f}{3} \left[\frac{1}{(\frac{\sigma_3}{\sigma_m} - 1)^{-1} + H} + \frac{2}{(\frac{\sigma_1}{\sigma_m} - 1)^{-1} + (1 - H)/2} \right], \quad (4.13)$$

where f is the inclusion volume fraction, σ_m denotes the conductivity of the metal matrix, σ_3 and σ_1 are the in- and out-of-plane conductivities of the graphitic structures, respectively, and H represents the influence of the GNR aspect ratio $p = L/W$

via the expression

$$H(p) = \frac{1}{p^2 - 1} \left[\frac{p}{\sqrt{p^2 - 1}} \ln \left(p + \sqrt{p^2 - 1} \right) - 1 \right] \quad (4.14)$$

where L is the ribbon length and W is the width. As p becomes larger (more needle-like), $H(p)$ rapidly becomes small; $H \approx 0.002$ for $p = 40$.

It follows from the c-AFM measurements of Cao et al. [44] that, due to the low carrier density *within* a sheet of many-layer graphene, the bulk of the graphene does not contribute to enhanced conductivity of the overall composite. Therefore, in this work, the relevant volume fraction is only the outermost atomic layers of graphene which are in direct contact with the metal. It now becomes necessary to replace the overall C volume fraction f in Eq. 4.13 with an effective volume fraction, f_{eff} , representing only the volume of the top and bottom monolayers of graphene in a many-layer graphene nanoribbon:

$$f_{eff} = f \left(\frac{V_{GNR,surface}}{V_{GNR,total}} \right) = f \left(\frac{2}{N \text{ of GNR layers}} \right), \quad (4.15)$$

such that Eq. 4.13 becomes

$$\frac{\sigma_e}{\sigma_m} = 1 + \frac{f_{eff}}{3} \left[\frac{1}{\left(\frac{\sigma_3}{\sigma_m} - 1 \right)^{-1} + H} + \frac{2}{\left(\frac{\sigma_1}{\sigma_m} - 1 \right)^{-1} + (1 - H)/2} \right]. \quad (4.16)$$

Note that f_{eff} depends only on the thickness of the graphene; it is independent of both L and W . Therefore, for needle-like inclusions with p large and $H(p)$

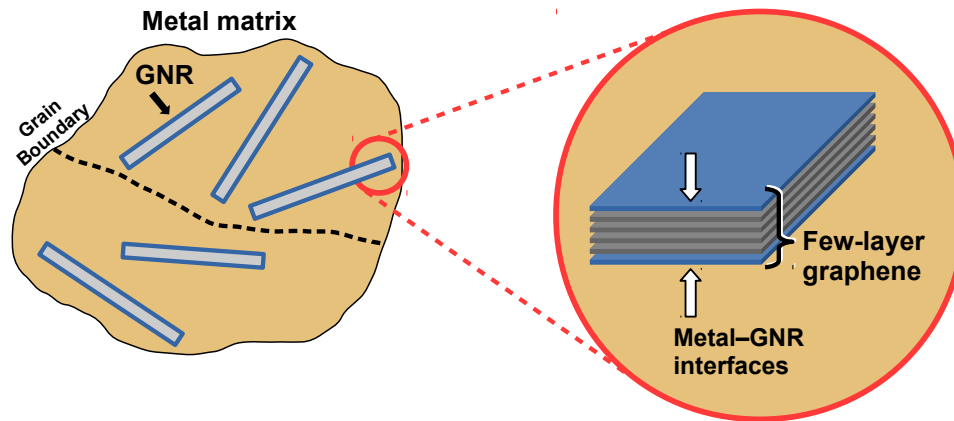


Figure 4.34: Enhanced detail of the metal matrix and embedded few-layer graphene. Only the outer monolayers of graphene (metal-GNR interfaces, highlighted in blue) are treated as having enhanced conductivity; the interior of the GNRs and the matrix properties are identical to their respective bulk values.

small, the thickness of the nanoribbons is overwhelmingly the dominant dimensional variable in this model.

The present work assumes that the bulk properties of carbon (i.e. graphite) and metal are unchanged in composites with the exception of the doped metal/graphene interface. Thus, the inclusion of a single GNR in the metal matrix is treated as illustrated in the detail box on the right-hand side of Fig. 4.34, with distinct edge regions (blue; top and bottom) and bulk regions (gray; interior). The model assumes ideal electrical contact at interfaces and neglects percolation effects, as the total volume fractions f under consideration are small, under 5%.

4.3.5 Results

The effective medium model was first validated using the experimental results of Cao et al. [44]. The operative principle was that if the model is accurate, it should

be able to take the theoretical calculation of carrier density and graphene dimensions as inputs, and generate the experimentally-measured conductivity increase as the output. Using the reported values of $\sigma_3 = 7.1 \times 10^{10}$ S/m at the Cu-graphene interface, graphene bilayer thickness of 0.7 nm, width and length of 30 μm , and fill factor $f = 0.008\%$, an effective relative conductivity of $\sigma_e/\sigma_m = 103.5\%$ is predicted. This 3.5% increase compares favorably with the 5.2% enhancement measured by c-AFM and attributed to the presence of graphene by Cao et al., indicating that the model should produce adequate predictions for systems yet to be realized. The following models predict the bulk conductivity of covetics using doped-graphene conductivities that were respectively measured and reported in literature (Case 1), and predicted using the quantum conductance model introduced in Sec. 4.3.3 (Case 2).

Case 1: Few-layer graphene embedded in Al with σ_3 measured at imperfect interfaces

Recent covetics work has focused largely on Al [56, 156], which is preferred for many applications such as grid-scale power transmission due to its favorable combination of mechanical strength, electrical conductivity, and low density. However, the formation of an Al-graphene composite presents unique challenges. Ensuring good graphene-metal contact is more difficult with Al than with Cu as it is not a suitable substrate for CVD growth of graphene, and additionally forms an oxide passivation layer rapidly upon contact with air or other source of oxygen [45]. Using the effective medium model to predict the properties of a “real world” Al-GNR system requires an estimate of the impact of this oxide layer on the metal-graphene charge transfer responsible for bulk conductivity enhancement. Reasonable values were provided by

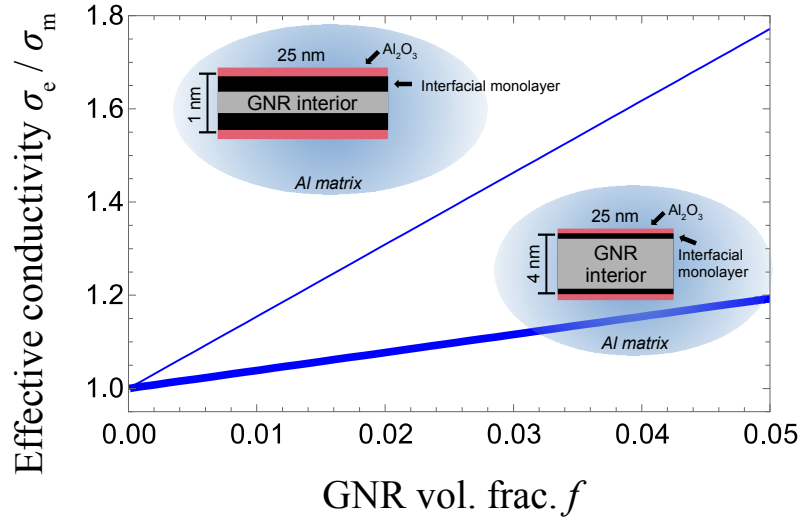


Figure 4.35: Estimated effective conductivity of Al-matrix composites with randomly aligned GNRs of the cross-sections shown (insets; not to scale), $1\text{-}\mu\text{m}$ long, as a function of GNR volume fraction f . Thicker GNRs have a smaller fraction of their volume exposed to the metal surface, so the effective conductivity is correspondingly lower. σ_e was calculated using Eq. 4.16 via a measurement of conductivity at a real Al/graphene interface [45].

conductive AFM measurements of the Al-bilayer graphene system reported by Cao et al. in Ref. [45]; in that case, σ_3 was 2.55×10^9 S/m. This measurement accounted for the few-nm thick aluminum oxide passivation layer which was observed in that system. The projected conductivity enhancement as a function of GNR vol. fraction is illustrated in Fig. 4.35 for this value of σ_3 , with $\sigma_1 = 10^{-5} \times \sigma_3$, GNRs 25 nm wide \times $1\text{ }\mu\text{m}$ long, with thicknesses of 3 and 12 layers (respectively 1 and 4 nm) and a nominally 60% IACS Al matrix.

For a GNR volume fraction of 5% (equivalent to ≈ 4 wt.% C), the effective conductivity of the bulk composite with 12-layer GNRs would be 19% greater than the matrix, which corresponds to an absolute conductivity of about 71% IACS. The enhancement is significantly greater in the 3-layer system, where 2/3 of the carbon volume supports enhanced conductivity, as opposed to 1/6 of the volume

in the 12-layer GNRs. The direct measurement of in-plane conductivity σ_3 used in this calculation took into account the detrimental effect of interfacial Al_2O_3 (red in Fig. 4.35) on the conductivity enhancement as described in Ref. [45]. Since the interfacial conductivity σ_3 was provided by measurement of a real system, this model accounts for the presence of interfacial oxide impurities, as long as the dimensions assumed for graphene ribbons can be ensured throughout the composite.

Case 2: Few-layer graphene embedded in Al with σ_3 corresponding to the ideal quantum conductance

To complement the measurement-based model, one can also build a model on the conductivity values determined from first principles within the framework of quantum mechanics. The preceding effective-medium case uses a direct measurement of conductivity from a specific geometry of Al-graphene system, which brings with it some inherent limitations. The most significant of these is that the measurement was based on a carefully built-up stack of metal foils and graphene sheets which extended laterally for tens of microns in both in-plane directions [45]; however, the conductance will be different for different graphene geometries, as explored in Sec. 4.3.3.2. From the plot of resistance per unit length, r , in Fig. 4.30, the axial conductivity of graphene nanoribbons is readily obtained via

$$\sigma_{GNR} = \frac{GL}{A}, \quad (4.17)$$

where A is the ribbon cross section taken to be $W \times 0.34$ nm. The conductivity σ_{GNR} relative to aluminum is shown in Fig. 4.36(a).

Using these values as inputs to the effective-medium model of Eq. 4.16, Fig. 4.36(b) shows the effective conductivity increase for bulk Al-GNR composites as a function of carbon volume fraction f , in conjunction with the geometry depicted in the inset: $W = 120$ nm, $L = 1000$ nm, and $t = 3$ layers. The most obvious difference between this case and Case 1 (shown again on Fig. 4.36(b) as “Cao reference”) is the significantly lower projected conductivity increases. In the case of $E_F = 0.4$ eV, where the conductivity of the 120 nm-wide GNR is very close to that of Al, the conductivity of the resultant composite actually decreases with f , due to the low out-of-plane conductivity term ($\sigma_1 = 10^{-5} \times \sigma_3$) and insufficiently high in-plane conductivity to compensate for it. Larger E_F yields small improvements in the conductivity of the bulk composite, roughly on the order of what has been recently reported in Al covetics: A 3.6 wt.% graphitic C concentration was correlated with an increase in bulk conductivity σ_e from $58.5 \pm 0.7\%$ to $61.8 \pm 0.7\%$ IACS, for a fractional improvement of $5.7 \pm 1.7\%$ on a length scale of roughly 1 cm [140].

4.3.6 Discussion

The results of the effective-medium models in the preceding section illuminate several concepts that are significant for covetics development. Comparison of the two model cases—the first based on a conductivity measurement from a carefully engineered stack of Al foils alternated with CVD-grown bilayer graphene sheets, and

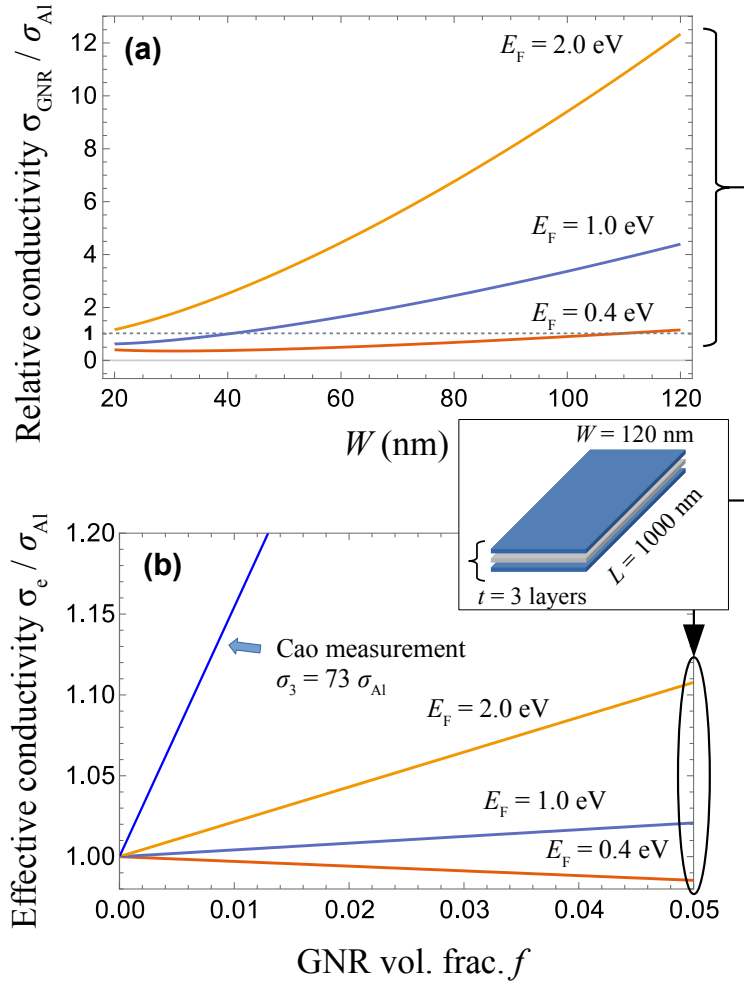


Figure 4.36: (a) Ideal GNR conductivities relative to pure Al, taken from the calculated resistances per unit length shown in Fig. 4.30(c). For each value of E_F , the conductivity of the GNR transitions to being greater than the metal at a critical width, indicated by intersection with the dashed gray line. (b) Effective conductivity of composites made from GNRs with the indicated dimensions. The effective-medium approximations were calculated using Eq. 4.16 and the σ_{GNR} values given in (a) at $W = 120$ nm as the in-plane conductivities, σ_3 .

the second grounded more firmly in the fundamental physics—helps to elucidate these concepts.

The fundamental point to establish is that the potential exists to enhance the bulk conductivity of Al alloys by incorporation of small volume fractions of graphitic nanostructures. This is the same conclusion reached by Hjortsam et al. in 2004 regarding carbon nanotubes embedded in copper [150], however the present work builds upon that of Hjortsam in important ways. First, the present model is better adapted to a realistic composite system in terms of the low carbon loading: 5 vol.% or lower vs. over 40% in Hjortsam. Such a large C volume fraction would likely compromise the structural integrity of the composite as a whole, especially given the potential for structural weakness and oxidation at metal-carbon interfaces. The Hjortsam model additionally did not account for scattering within or between graphitic structures, whereas both model cases in the present work incorporate the effects of scattering (either by reference to direct measurement or by theory). Even the more conservative Case 2, based on the quantum confinement of electrons in a narrow GNR, suggests a modest conductivity enhancement in the bulk Al covetic of between 2–10% for Fermi energies between 1–2 eV and a carbon volume fraction of 5% (i.e., 4 wt.%). The recently reported 5.7% relative conductivity enhancement for a 3.6 wt.% C-Al covetic falls neatly within this range [140].

Furthermore, it is clear that the geometry of the graphitic carbon has a large influence on the conductivity of the final composite, based on the roughly 10-fold difference in measured in-plane conductivity for wide graphene sheets embedded in Al ($\sigma_3 = 2.55 \times 10^9$ S/m, [45]) relative to the projections based on quantum

confinement. The different dimensions of graphene between the two cases may account for most if not all of this difference. A larger width/length dimension (the two can be considered equivalent for the case of randomly oriented inclusions) appears to lead to greater conductivity in the graphitic inclusions, and thus the overall composite, due to the greater number of quantum-mechanical modes allowed for a particular Fermi energy. On the other hand, larger thickness is always detrimental to conductivity because only a small fraction of the total carbon present is doped by contact with the metal; the interior layers of graphene are analogous to graphite, which results in diminished conductivity as illustrated by the simple Rule of Mixtures model in Fig. 4.26. In spite of the broad applicability of the effective-medium approach, uncertainty surrounding the dimensions of graphene ribbons and sheets embedded in metals leads to a wide range of projected conductivity changes in the bulk composite, ranging from trivial to remarkable.

It was not feasible to directly calculate the carrier mobility of the Al-GNR interface due to the long relaxation time of phononic interactions. An order-of-magnitude estimate for the conductivity of this region may be obtained via mobility measurements from similar systems, such as graphene-based field effect transistors (FETs). These systems yield mobilities on the order of $10^4 \text{ cm}^2/\text{Vs}$ [174, 175], including in the regime of large carrier densities above 10^{14} cm^{-2} facilitated by interfaces such as ionic gates [40]. Given $\mu = 10^4 \text{ cm}^2/\text{Vs}$ and $n = 1.7 \times 10^{14} \text{ cm}^{-2}$ (i.e. $5.1 \times 10^{21} \text{ cm}^{-3}$), the doped GNR conductivity would be on the order of $8 \times 10^8 \text{ S/m}$. This value is not far off from the measurement of $\sigma_3 = 2.55 \times 10^9 \text{ S/m}$ used for the effective medium approximation, which indicates that the model is,

generally speaking, reasonable. Nevertheless, the measured conductivity was higher by a factor of 3, even though it represented a reduction from the ideal (due to the interfacial aluminum oxide). This implies that electrons may behave differently in graphene embedded in metals compared to graphene that is suspended [34] or on a non-metallic substrate, which tend to show a $\mu \propto 1/n$ dependence [37, 48] that was not observed in the work of Cao et al. [44, 45].

A further constraint on the domain of the model is that it is not valid for high concentrations of inclusions. When the volume fraction f is sufficiently large that the inclusions are able to interact directly with each other over a long range, the assumption inherent in the model—that inclusions are dilute and non-interacting—no longer applies. At this stage the system has reached the percolation threshold where transport can proceed through chains of inclusions rather than the matrix [87]. If the inclusions are more conductive than the matrix, the overall conductivity proceeds to rise sharply above the effective medium prediction with increasing f over a small transition region [176]. The specific volume-fraction value of the percolation threshold is a strong function of the inclusions' aspect ratio of length to width; for instance, needle-like inclusions can connect end-to-end with less material than required for spheres or plates. This dependence is reflected in numerical [151] and analytical estimates [176] showing threshold volume fractions of randomly-oriented ellipsoids ranging from 0.29 for spheres to below 0.01 for aspect ratios greater than 100 [151].

4.4 Summary

A broad range of qualitative and quantitative measurements were performed on a series of covetic and reference specimens in the course of this work. By identifying graphitic regions of interest using Raman spectroscopy, it was possible to prepare TEM specimens corresponding to specific graphitic features and orientations within the samples. Distributions of graphitic crystallite size, L_a , estimated from Raman spectroscopy were positively-skewed after the covetics reactions, which suggested non-uniform rates of graphitic ordering. Inspection of the Raman 2D peaks indicated that graphitic carbon generally took the form of few-layer graphene comprising 3–10 layers.

Large and thick ordered carbon structures on length scales of microns to tens of microns were observed by TEM in a majority of samples. Electron diffraction and HRTEM imaging confirmed that these were graphitic, but also exhibited small-scale undulations. Al and C phases also tended to remain separate in these regions, with minimal penetration of C structures into Al. STEM-EDS mapping of these interface regions indicated that an aluminum oxide layer of up to 250 nm thick was often present between C and Al. This interfacial layer and the large-scale nature of these thick graphitic structures suggest that they will not contribute to enhanced electrical conductivity and could be actively detrimental. On the other hand, a covetic specimen with a reported conductivity enhancement of over 15% shows unique nanostructured forms of graphitic carbon, including long narrow fibers and ribbons spanning across Al grain boundaries. In contrast to the larger inclusions, these

structures appeared well-ordered and well-integrated in the metal matrix and did not show evidence of oxidation. Investigation of the samples' mechanical properties indicates that observed increases in electrical conductivity were independent of microstructural defects such as grain boundaries. Graphitic nanoribbon structures are therefore the most likely origin of electrical conductivity enhancement in composites.

A simple effective medium approximation was used to model the conductivity of Al-based nanocarbon-metal composites with varying graphitic inclusion dimensions and concentrations. Conductivity enhancements on the order of 10% relative to the matrix are projected on the basis of localized conductivity measurements reported in literature as well as first-principles DFT calculations, which indicate doping of graphene layers via electron transfer in the presence of metals. Two model cases were used to project the conductivity of bulk composites based on reported measurement and on quantum confinement of propagating electrons, with the latter providing a conductivity value closely aligned with recent experimental work. Graphene nanoribbons will ideally be wide, long, and thin (mono- or bi-layer) in order to fully exploit the localized charge transfer at the metal-graphene interface. Future computational research in this area may explore first-principles methods to determine the transport properties—in particular, carrier mobility—of the doped Al-graphene interface, which in conjunction with the calculated carrier density would provide a complete theoretical prediction of conductivity enhancement in composites.

Chapter 5: Conclusions

5.1 Summary of research

Through the analytical framework of electron microscopy, this work brings together two seemingly unrelated material systems—wide-bandgap semiconductors and nanocarbon-metal composites. Both of these systems have the potential to support more efficient and sustainable energy transfer technologies such as lighter-weight vehicles which will be essential to confront global challenges such as climate change. They also present materials-characterization challenges, which must first be understood in order to realize that vision.

5.1.1 Wide-bandgap MOS interfaces

Silicon carbide represents a success story in the realm of wide-bandgap technologies, as the last 20 years have seen it transition from the laboratory into commercial applications. The potential for continued improvement nevertheless remains, in the form of novel annealing treatments that may exceed the performance enhancement imparted by the present NO anneal. This thesis has explored the structural and composition characteristics of SiC MOS structures with boron-doped SiO₂ ox-

ide (BSG) and Sb ion-implanted SiC in conjunction with NO post-oxidation anneal (Sb+NO). In the SiC/BSG system, EELS spectrum imaging in conjunction with multivariate statistical analysis indicated a narrow pile-up of B less than 3 nm wide immediately at the interface, with a uniform lower concentration throughout the bulk of the BSG layer. The fine structure of the B-*K* edge indicated sp^2 hybridization, which is predicted to relieve interfacial stresses and thus can act as a mechanism for the reduction in D_{it} previously observed in B-doped SiC MOS devices. This system also provided an opportunity to explore and validate the MCR-LLM algorithm for hyperspectral decomposition of EELS data in a doped wide-bandgap MOS structure. In the Sb+NO system, this algorithm was used to identify a weak Sb EELS edge that could not be identified by NMF. The relatively smaller interface transition width in this device and overall abrupt, stable structure suggest that Sb counter-doping is a viable method to improve channel mobility from a structural quality perspective, independently from and in addition to post-oxidation annealing.

Gallium oxide device technology is significantly less mature but presents significant advantages over SiC and other wide-bandgap systems for very high-power and high-voltage applications. This thesis investigated the structure of β -Ga₂O₃ interfaces with SiO₂ and Al₂O₃ gate oxide layers prepared under a range of deposition and post-deposition anneal (PDA) conditions. Elevated PDA temperature was correlated with a larger amplitude of interfacial roughening likely to be detrimental to the long-term reliability of the gate oxide. In the case of Al₂O₃ gate oxides produced by atomic layer deposition, an interdiffusion region containing both Ga and Al was found to extend several nm wide across the interface, with the use of a PDA step

correlated with the wider transition regions. TEM characterization of $\text{Ga}_2\text{O}_3/\text{Al}_2\text{O}_3$ specimens also led to the unexpected finding that the initially amorphous Al_2O_3 became crystalline upon exposure to the electron beam. The phenomenon resulted in a highly-oriented, fully-crystalline gate oxide layer after tens of seconds' exposure. Faster rates of crystallization using a 100-keV electron beam indicated that an ionization-induced atomic rearrangement mechanism is the probable origin of this phenomenon, which is likely to alter the electronic properties of the device.

5.1.2 Nanocarbon-metal composites (Covetics)

The goal of covetics development is to utilize the superior properties of nanostructured carbon to enhance the bulk properties of widely used metals such as aluminum alloys, ultimately leading to industrial efficiency gains in terms of reduced resistive losses and lower material usage. This thesis has sought to explore covetic Al composites from both experimental and theoretical angles in order to capture the full range of possibilities presented by a technology which remains far from maturity.

Structure-property relationships in covetics were investigated experimentally using progressively smaller-scale spectroscopy methods. Raman spectroscopy was used to determine the carbon distribution and degree of ordering on length scales of microns to millimeters. Raman spectrum images comprising hundreds to thousands of individual spectra indicated that graphitic ordering consistently occurred after exposures to concentrated direct current above critical thresholds of current density and duration. Graphitic crystallite size, L_a , was estimated from the integrated

intensity ratios of the G (graphitic) to the D (disorder) peaks in the Raman spectra and compared to the ratio in the activated carbon used as source. The average value of L_a was directly related to the duration of applied current. Compilation of over 1000 spectra per sample revealed that the L_a distribution became asymmetric after the covetics reaction, which is a clear indication that the applied current had played a role in the ordering of graphitic crystallites embedded in the Al matrix. Inspection of the Raman 2D peak strongly associated with layered graphitic structures indicated that between 3–10 layers of graphene were typically stacked together.

TEM investigation of several Al covetic samples in Sec. 4.2 revealed significant variability in the structure and distribution of carbon within the metal matrix. Two main types of structure were identified: graphitic inclusions on the length scale of microns to tens of microns, and thin, narrow aligned graphene ribbons tens of nm wide and several microns in length. The thicker inclusions generally exhibited an interfacial oxide region between C and Al on the order of 100 nm wide, which would be detrimental for bulk conductivity and tensile strength and most likely prevented the carbon from extending into the Al matrix surrounding these areas. Conversely, graphitic ribbons were well integrated in the metal matrix, spanning between grains with minimal separation or oxidation, and are the most likely to lead to enhanced bulk conductivity in these structures.

The magnitude of property enhancement that a covetic composite may provide constituted an important knowledge gap at the start of this work. This thesis sought to develop more quantitative modeling approaches for the prediction and engineering of electrical conductivity in nanocarbon-metal composites. Using a quantum

mechanical model, graphene nanoribbons embedded in Al were estimated to contribute a locally enhanced conductivity at the Al/C interface. An effective-medium model was used to predict the effect of this enhancement on a bulk Al composite with randomly oriented graphene nanoribbons as a function of the ribbon geometry and the C volume fraction. Wide, thin ribbons contribute most efficiently to the conductivity enhancement, up to several percent relative increase per volume percent of C.

5.2 Recommendations for future work

5.2.1 Wide-bandgap MOS interfaces

Further investigation will be necessary to image the nanostructure of the β -Ga₂O₃/amorphous Al₂O₃ system prior to initial crystallization, because even the moderate electron doses and accelerating voltages used for structure determination in this work were sufficient to initiate the crystalline transformation. The techniques of *high-speed electron microscopy* will be useful for this purpose. There are broadly two categories of high-speed techniques, each facilitated by laser-induced photoemission: single-shot or dynamic TEM (DTEM) and stroboscopic or ultrafast TEM (UTEM) [177]. The former generates an intense pulse of $\approx 10^9$ electrons on a timescale of nanoseconds, which is suitable to capture irreversible processes such as microstructure evolution or crystallization in conjunction with a fast image-capture system. In the case of beam-induced crystallization the primary advantage is that, unlike conventional in-situ imaging, the illumination does not need to be continu-

ous and the total electron exposure necessary to capture an image may be reduced. High-speed EM techniques offer a potential solution to the difficulties encountered in this work of imaging the interface structure as-fabricated, without altering it through excessive exposure to the electron beam.

5.2.2 Nanocarbon-metal composites

A range of different covetic micro- and nanostructures were observed in the course of this work. Uncertainty remains regarding when and how certain features emerge, and the ability to control the composite structure will be essential to covetics' commercialization. With regard to fabrication, it would be worthwhile to investigate ways to eliminate the interfacial aluminum oxide between C and Al, for instance by preparing samples in an oxygen-free environment. Greater control over the graphitic nanostructure will also be desirable in order to increase the concentration of graphene nanoribbons and sheets, and avoid trapping large graphitic clusters in the matrix. Potential for improvement exists with regard to more uniform, higher-speed mixing of the melt and bubbling of inert gas to remove oxygen and eliminate void formation; these are topics of active research at the time of this writing. Additionally, the wetting behavior between molten Al and graphitic C is known to be poor [178, 179]; the potential for alloy-compatible additives such as Cu or Ni to increase contact between the matrix and inclusions in covetics would be worthy of further investigation. There are several broader directions in which covetics research and development may be extended. Other metals' potential as

covetics have not been studied as thoroughly as Al; elemental Cu and Ag are better electrical conductors which have also been demonstrated as covetics. It would be worthwhile to investigate the processing, structure and performance of Cu- and Ag-carbon composites in order to validate and build upon the findings in this project. Furthermore, Cu is of particular importance for microelectronic interconnects, where continual reductions in component size—without loss of performance—are essential to facilitate continued development of advanced semiconductor technologies.

Appendix A: Measurement of electron-beam currents in the field-emission TEM

In order to quantify the effect of the electron beam on the crystallization of the gate oxide, it was necessary to estimate the total current imparted by the beam to the specimen, including backscattered electrons and accounting for any systematic error in the current density reported from the fluorescent screen. Neither the TEM nor the specimen holder in this work were equipped with a Faraday cup to measure the current directly. However, it was possible to make a series of accurate beam current measurements using the drift tube of the Gatan Imaging Filter (GIF) in conjunction with an external picoammeter, as described by Mitchell and Nancarrow [180].

A.1 Approach

Following this method, the magnetic prism was switched off so that electrons reaching the bottom of the TEM column, which would strike the screen or CCD to form images, instead struck the wall of the drift tube. The resulting electric current was captured by a safe high voltage (SHV) cable ordinarily leading from the drift tube to the GIF power supply. For these measurements, the SHV cable from the GIF was connected directly to a Keithley electrometer (Model 617) with

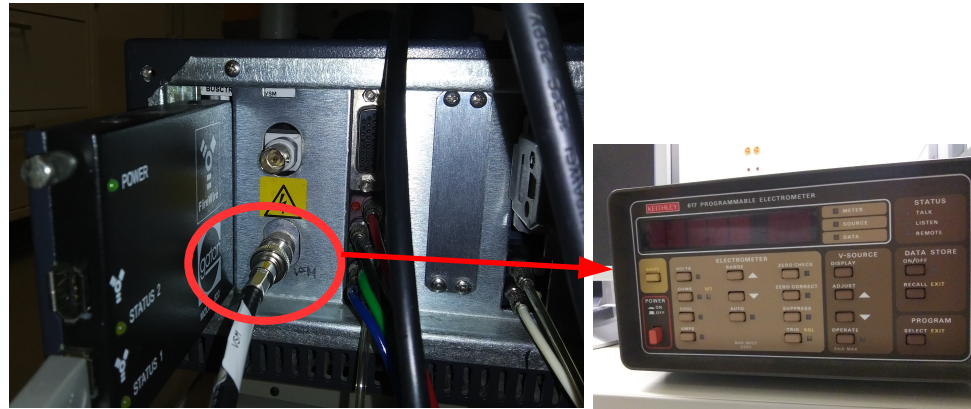


Figure A.1: The safe high voltage (SHV) cable leading from the EEL spectrometer drift tube, originally connected to the GIF power supply (left), was connected to a Keithley electrometer (right) to measure the total electron beam current incident on the wall of the drift tube with pA sensitivity.

pA resolution by means of a custom-built SHV-BNC adapter. A photograph of the equipment used appears in Fig. A.1.

Electron beam currents were measured for a range of conventional TEM-mode conditions. The variables most commonly used to change the beam current are the choice of condenser lens aperture (CLA), from 1 (largest) to 3 (the smallest typically used; CLA 4 is the smallest available), and spot size (“Spot”), ranging from 1 (larger fully-converged spot) to 5 (smaller) [181]. Magnification was not expected to affect the total current, and measurements were taken at 40 kx and 200 kx to confirm that this was in fact the case.

For each condition, measurements were first taken at the drift tube by the electrometer, with the beam fully converged, after allowing a few seconds for the reading to stabilize (a precaution to minimize the influence of the drift tube capacitance [180]). The beam was then spread to about 60 % of the screen diameter, and

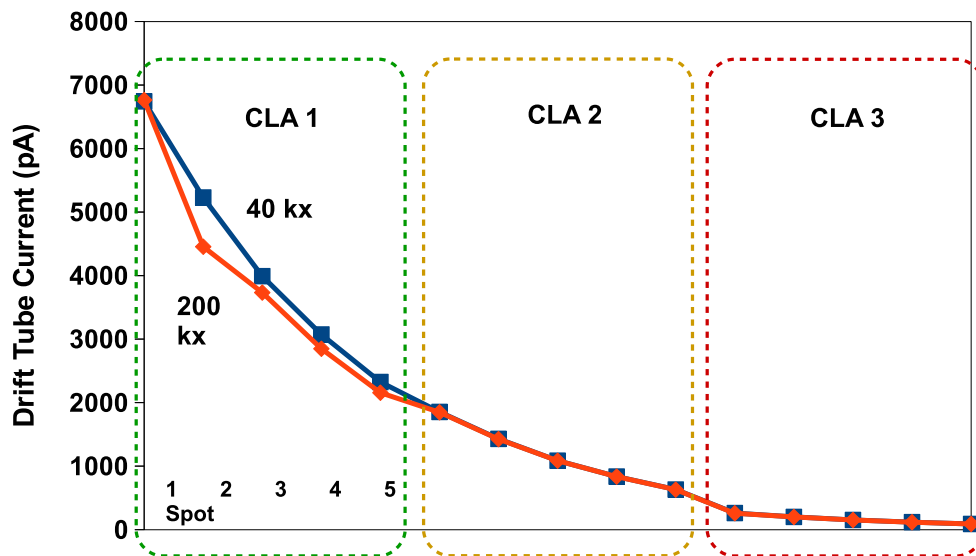


Figure A.2: Measurements of total TEM beam current collected using the EELS drift tube and picoammeter for a range of conventional TEM-mode conditions (CLA 1–3, Spot size 1–5, and Mag. 40 and 200 kx.) Systematically lower current readings using CLA 1 at 200 kx are attributed to the 5-mm GIF entrance aperture blocking part of the beam at the higher magnification. Good agreement between the 40- and 200-kx measurements using the smaller CL apertures 2 and 3 means that the magnification had no meaningful influence on the total beam current.

the screen current density was recorded from the JEOL operation software. Data from these measurements are shown in Fig. A.2 and Fig. A.3, respectively.

The 5-mm diameter of the GIF entrance aperture was a known limitation, which in certain cases led to discrepancies; notably, current readings using CLA 1 at 200 kx were systematically lower than those taken at 40 kx, a deviation which did not occur for the smaller CL apertures. It was found during the experiment that the beam would not converge to as small a physical spot at 200 kx than at 40 kx, so the 200-kx values are systematically low, probably due to some blocking of the beam by the GIF aperture. Therefore, the 40-kx measurements are considered more accurate. Using CLA 2 and 3, 40- and 200-kx measurements agreed very well, so the magnification did not appear to affect the total current, as expected.

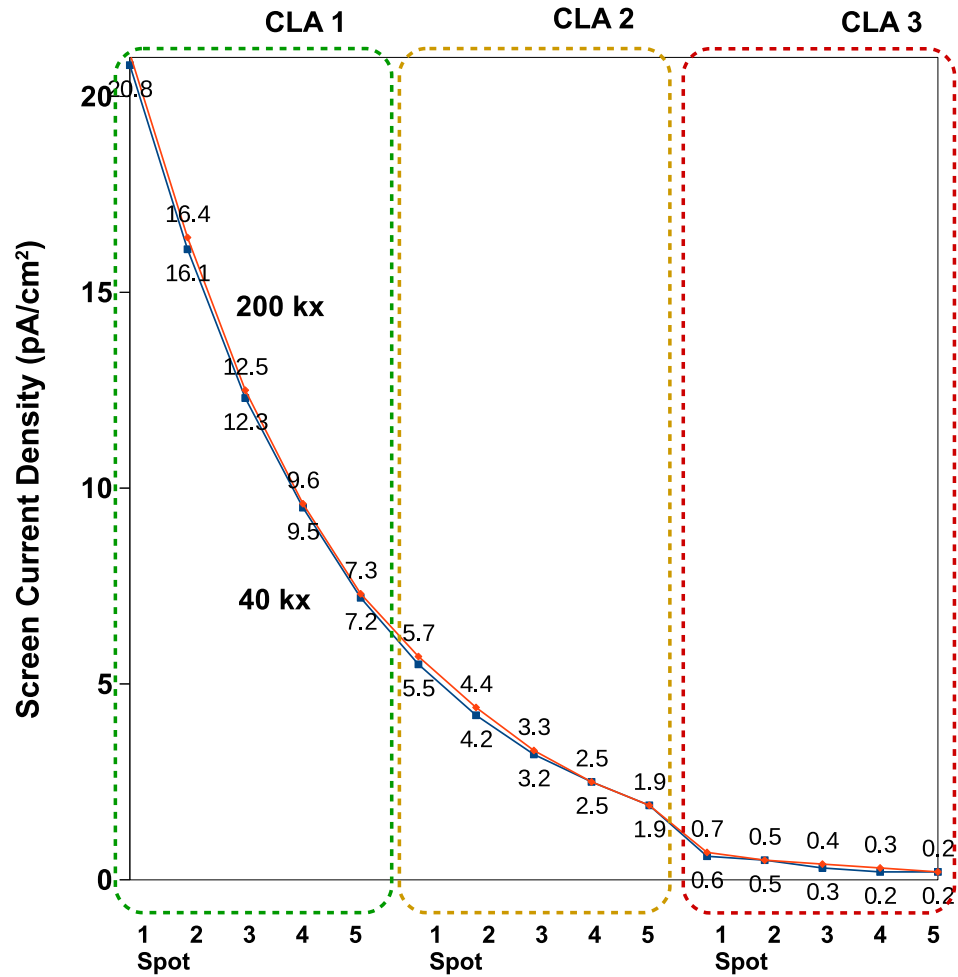


Figure A.3: Beam current densities reported by the phosphorescent large screen, when the beam was spread to about 12 cm diameter. Readings at 200 kx (upper red curve) were systematically higher than at 40 kx (lower blue curve), typically by a magnitude comparable to the precision of the measurement (i.e. the margin of error, ± 0.1 pA/cm²).

Measurements of the screen current density (Fig. A.3) showed slightly larger values at 200 kx than at 40 kx, but the magnitude of deviation was comparable to or less than the precision of the measurement (i.e. the margin of error, ± 0.1 pA/cm²).

For the purpose of the beam-induced crystallization experiments described in Sec. 3.2.2, direct measurements of the current density at the EELS drift tube were the most useful thanks to the high precision of the picoammeter, once it was confirmed that magnification did not affect the total current. These measurements were repeated for both 100 kV and 200 kV conditions.

A.2 Estimating the electron dose rate on the specimen

Total current measurements were used to estimate specimen current densities on β -Ga₂O₃/Al₂O₃ lamellas introduced in Sec. 3.2.2. This was done by relating the known width of the deposited gate oxide layer, which was consistent within each sample, to the diameter of the beam on the phosphor screen. The approach is demonstrated in Fig. A.4 for the lower-intensity 100-keV case. In general it was not possible to see the extent of the beam on TEM images, due to magnification inherent in the CCD image-capture optics (this condition is suitable for imaging in conventional TEM mode where a broad parallel beam is desired). In order to obtain the beam diameter and convert the drift-tube current measurements to an incident current density on the specimen, the beam was converged so that its diameter would match that of the large phosphor screen (Fig. A.4(b)). After optically photographing the beam on the screen—off-axis, due to the angle of the viewing window—and

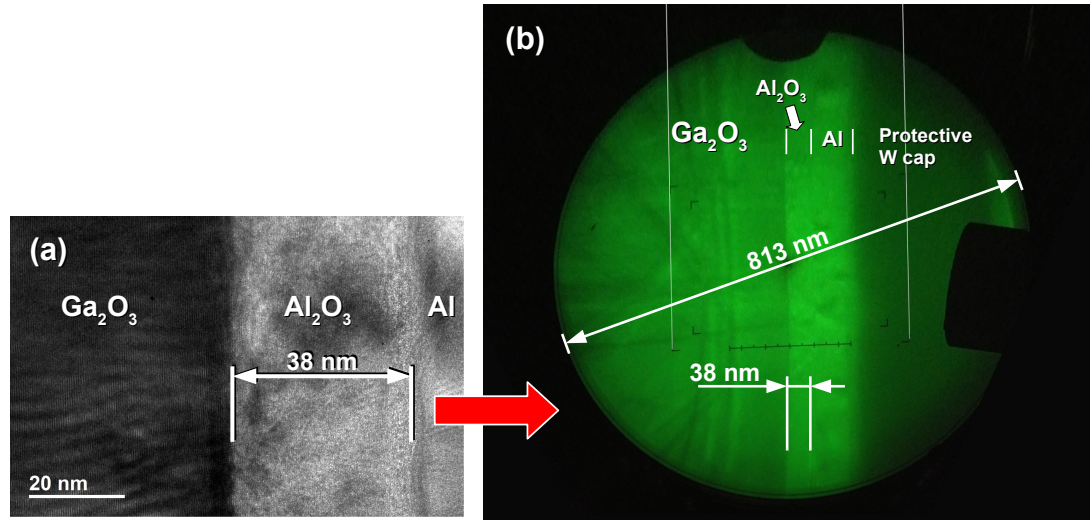


Figure A.4: (a) In the TEM image the CCD viewing range is significantly smaller than the beam diameter under typical intensities and exposures, which is normally desirable to provide uniform illumination, however the beam size is not apparent. (b) Comparison of the gate oxide width (38 ± 2 nm) in the TEM image with the image on the phosphor screen provided an estimate of the beam diameter (813 ± 43 nm) once the beam was converged to exactly fill the screen. The thin vertical white lines defining the width of the gate oxide film served as guides for the eye during image post-processing while adjusting the image perspective to be in parallel with the beam, normal to the screen.

adjusting the perspective of the image to make the beam circular via digital post-processing, it was simple to measure the beam diameter as a multiple of the width of the gate oxide (38 nm). Due to the diffusion which occurred between Ga and Al from the substrate and gate oxide, respectively, the interface had a transition width of some 3–5 nm as discussed in Sec. 3.2.1, which translated to an uncertainty in the width of the gate oxide imaged by HRTEM of about 2 nm, a relative uncertainty of 5.3 %. Therefore, a best estimate of the beam diameter in Fig. A.4 was 813 ± 43 nm.

Appendix B: Publications and presentations related to this work

Publications

1. C. Shumeyko, X. Ge, C. Klingshirn, L. Salamanca-Riba, D. Cole, “Tunable mechanical behavior of graphene nanoribbon-metal composites fabricated through an electrocharge-assisted process,” *Materials Science & Engineering A* 800, 140289 (2021) [[145](#)]
2. C. Klingshirn, A. Jayawardena, S. Dhar, R. Ramamurthy, D. Morissette, Z. Warecki, J. Cumings, T. Zheleva, A. Lelis, L. Salamanca-Riba, “Electron beam-induced crystallization of Al₂O₃ gate oxide on β -Ga₂O₃,” *Micron* 140, 102954 (2021) [[182](#)]
3. X. Ge, C. Klingshirn, M. Morales, M. Wuttig, O. Rabin, C.M. Shumeyko, D.P. Cole, S. Zhang, and L.G. Salamanca-Riba, “High Electrical Conductivity of Nano-Carbon-Aluminum Composites,” *Carbon*, Carbon 173, 115 (2021) [[140](#)]
4. C. Klingshirn, A. Jayawardena, S. Dhar, R. Ramamurthy, D. Morissette, T. Zheleva, A. Lelis, L. Salamanca-Riba, “Analytical Electron Microscopy of Ga₂O₃/SiO₂ and Ga₂O₃/Al₂O₃ Interface Structures in MOS Devices,” in preparation (2020)

5. X. Ge, C. Klingshirn, M. Wuttig, K. Gaskell, P.Y. Zavalij, Y. Liang, C.M. Shumeyko, D.P. Cole, and L.G. Salamanca-Riba, “Mechanism studies and fabrication for the incorporation of carbon into Al alloys by the electro-charging assisted process,” *Carbon* 149, 203 (2019) [156]
6. U. Balachandran, S. Dorris, B. Ma, T. Lee, D. Forrest, and C. Klingshirn. Electrodes for making nanocarbon-infused metals and alloys. Provisional US Patent No. US20200176573A1 (2018)
7. J.A. Taillon, C.J. Klingshirn, C. Jiao, Y. Zheng, S. Dhar, T.S. Zheleva, A.J. Lelis, and L.G. Salamanca-Riba, “Analysis of the electronic and chemical structure in, boron and phosphorus passivated 4H-SiC/SiO₂ interfaces using HRTEM and EELS,” *Applied Physics Letters* 113 (2018) [99]

Conference presentations

1. “Modeling the Effective Electrical Conductivity of Nanocarbon-Metal Composites Made by the Electrocharging Assisted Process, accepted to the Materials Research Society Joint Spring/Fall Meeting, Virtual, Nov. 2020
2. “Effective electrical conductivity of nanocarbon-metal composites made by the electrocharging assisted process,” accepted to the American Physical Society March Meeting, Denver, USA, Mar. 2020.

3. "TEM Investigation of Local Mechanical Behavior in Nanocarbon-Aluminum Composites Made by the Electrocharging Assisted Process," Materials Research Society Fall Meeting, Boston, USA, Dec. 2019 (Poster)
4. "Analytical TEM-EELS and Raman Spectroscopy of Nanocarbon-Al Composites Made by the Electrocharging Assisted Process," Materials Research Society Fall Meeting, Boston, USA, Nov. 2018 (Poster)
5. "TEM-EELS Analysis of $\text{Ga}_2\text{O}_3/\text{SiO}_2$ and $\text{Ga}_2\text{O}_3/\text{Al}_2\text{O}_3$ Interface Structures with Electron Beam Induced Crystallization of Al_2O_3 Gate Layer," Materials Research Society Fall Meeting, Boston, USA, Nov. 2018
6. "Analytical Electron Microscopy of Antimony Doped 4H-SiC/ SiO_2 and 4H-SiC/Boron and Phosphorus Doped SiO_2 Interface Structures in MOS Devices," American Physical Society March Meeting, Los Angeles, USA, Mar. 2018.
7. "Sub-Nanometer Mapping of Boron-Passivated 4H-SiC/ SiO_2 Interfaces by Analytical Electron Microscopy," Infineon Winter School, Villach, Austria, Feb. 2018.
8. "Analytical Electron Microscopy of $\text{Ga}_2\text{O}_3/\text{SiO}_2$ and $\text{Ga}_2\text{O}_3/\text{Al}_2\text{O}_3$ Interface Structures in MOS Devices," Materials Research Society Fall Meeting, Boston, USA, Dec. 2017.
9. "EELS Characterization of 4H-SiC/Oxide Interfaces," SiC MOS Program Review, College Park, USA, Aug. 2017.

10. "In-situ analysis of catalyst nanoparticle growth using hot-stage transmission electron microscopy," DAAD Research Internships in Science & Engineering (RISE) Scholars' Meeting, Heidelberg, Germany, Jul. 2017.
11. "TEM-EELS Investigation of Boron and Phosphorus Passivated 4H-SiC/SiO₂ Interface Structures," American Physical Society March Meeting, New Orleans, USA, Mar. 2017.
12. "Raman Spectroscopy of High-Carbon Al Covalent Alloys," Materials Research Society Fall Meeting, Boston, USA, Nov. 2016 (Poster)

Bibliography

- [1] U.S. Department of Energy. Wide Bandgap Semiconductors : Pursuing the Promise. Technical report, 2013.
- [2] J. Y. Tsao, S. Chowdhury, M. A. Hollis, D. Jena, N. M. Johnson, K. A. Jones, R. J. Kaplar, S. Rajan, C. G. Van de Walle, E. Bellotti, C. L. Chua, R. Colazzo, M. E. Coltrin, J. A. Cooper, K. R. Evans, S. Graham, T. A. Grotjohn, E. R. Heller, M. Higashiwaki, M. S. Islam, P. W. Juodawlkis, M. A. Khan, A. D. Koehler, J. H. Leach, U. K. Mishra, R. J. Nemanich, R. C. N. Pilawa-Podgurski, J. B. Shealy, Z. Sitar, M. J. Tadjer, A. F. Witulski, M. Wraback, and J. A. Simmons. Ultrawide-Bandgap Semiconductors: Research Opportunities and Challenges. *Advanced Electronic Materials*, 1600501:1600501, 2017.
- [3] J B Casady and R W Johnson. Status of silicon carbide (SiC) as a wide-bandgap semiconductor for high-temperature applications: A review. *Solid-State Electronics*, 39(96):1409–1422, 1996.
- [4] C.E. Weitzel, J.W. Palmour, C.H. Carter, K. Moore, K.K. Nordquist, S. Allen, C. Thero, and M. Bhatnagar. Silicon carbide high-power devices. *IEEE Transactions on Electron Devices*, 43(10):1732–1741, 1996.
- [5] Burak Ozpineci and Leon Tolbert. Smaller, faster, tougher. *IEEE Spectrum*, 48(10):45–66, 2011.
- [6] Gang Liu, Blair Tuttle, and Sarit Dhar. Silicon carbide: A unique platform for metal-oxide-semiconductor physics. *APPLIED PHYSICS REVIEWS*, 2(2):021307–1 – 021307–21, 2015.
- [7] Hamid Amini Moghadam, Sima Dimitrijević, Jisheng Han, and Daniel Haasmann. Active defects in MOS devices on 4H-SiC: A critical review. *Microelectronics Reliability*, 60:1–9, 2016.
- [8] Michael A. Mastro, Akito Kuramata, Jacob Calkins, Jihyun Kim, Fan Ren, and S. J. Pearton. Perspective–Opportunities and Future Directions for

Ga₂O₃. *ECS Journal of Solid State Science and Technology*, 6(5):P356–P359, apr 2017.

- [9] G. Y. Chung, C. C. Tin, J. R. Williams, K. McDonald, R. K. Chanana, Robert A. Weller, S. T. Pantelides, Leonard C. Feldman, O. W. Holland, M. K. Das, and John W. Palmour. Improved inversion channel mobility for 4H-SiC MOSFETs following high temperature anneals in nitric oxide. *IEEE Electron Device Letters*, 22(4):176–178, 2001.
- [10] Hui-Feng Li, Sima Dimitrijević, H. Barry Harrison, and Denis Sweatman. Interfacial characteristics of N₂O and NO nitrided SiO₂ grown on SiC by rapid thermal processing. *Applied Physics Letters*, 70(15):2028–2030, 1997.
- [11] Peter De, Jan M Knaup, Christoph Thill, Adam Gali, and Thomas Frauenheim. The mechanism of defect creation and passivation at the SiC / SiO₂ interface. *JOURNAL OF PHYSICS D: APPLIED PHYSICS*, 40(20):6242–6253, 2007.
- [12] Dai Okamoto, Hiroshi Yano, Tomoaki Hatayama, and Takashi Fuyuki. Removal of near-interface traps at SiO₂/4H-SiC (0001) interfaces by phosphorus incorporation. *Applied Physics Letters*, 96(20):203508, 2010.
- [13] Dai Okamoto, Mitsuru Sometani, Shinsuke Harada, Ryoji Kosugi, Yoshiyuki Yonezawa, and Hiroshi Yano. Improved Channel Mobility in 4H-SiC MOSFETs by Boron Passivation. *IEEE Electron Device Letters*, 35(12):1176–1178, 2014.
- [14] Gang Liu, Ayayi C. Ahyi, Yi Xu, Tamara Isaacs-Smith, Yogesh K. Sharma, John R. Williams, Leonard C. Feldman, and Sarit Dhar. Enhanced Inversion Mobility on 4H-SiC (11-20) Using Phosphorus and Nitrogen Interface Passivation. *IEEE Electron Device Letters*, 34(2):181–183, 2013.
- [15] Y.K. Sharma, A.C. Ahyi, T. Issacs-Smith, X. Shen, S.T. Pantelides, X. Zhu, L.C. Feldman, J. Rozen, and J.R. Williams. Phosphorous passivation of the SiO₂/4H-SiC interface. *Solid-State Electronics*, 68:103–107, 2012.
- [16] C Jiao, A C Ahyi, C Xu, D Morissette, L C Feldman, and S Dhar. Phosphosilicate glass gated 4H-SiC metal-oxide-semiconductor devices: Phosphorus concentration dependence. *Journal of Applied Physics*, 119:155705, 2016.
- [17] Aaron Modic, Gang Liu, Ayayi C Ahyi, Yuming Zhou, Pingye Xu, Michael C Hamilton, John R Williams, Leonard C Feldman, and Sarit Dhar. High channel mobility 4H-SiC MOSFETs by antimony counter-doping. *IEEE Electron Device Letters*, 35(9):894–896, 2014.
- [18] Yongju Zheng, T. Isaacs-Smith, A. C. Ahyi, and S. Dhar. 4H-SiC MOSFETs With Borosilicate Glass Gate Dielectric and Antimony Counter-Doping. *IEEE Electron Device Letters*, 38(10):1433–1436, 2017.

- [19] Maria Cabello, Victor Soler, Narcis Mestres, Josep Montserrat, José Rebollo, José Millán, and Phillippe Godignon. Improved 4H-SiC N-MOSFET Interface Passivation by Combining N₂O Oxidation with Boron Diffusion. *Materials Science Forum*, 897:352–355, 2017.
- [20] Masataka Higashiwaki, Kohei Sasaki, Hisashi Murakami, Yoshinao Kumagai, Akinori Koukitu, Kuramata Akito, Takekazu Masui, and Shigenobu Yamakoshi. Recent progress in Ga₂O₃ power devices. *Semiconductor Science and Technology*, 31(3):34001, 2016.
- [21] Andrew M. Armstrong, Mary H. Crawford, Asanka Jayawardena, Ayayi Ahyi, and Sarit Dhar. Role of self-trapped holes in the photoconductive gain of β -gallium oxide Schottky diodes. *Journal of Applied Physics*, 119(10):1–7, 2016.
- [22] S. J. Pearton, Jiancheng Yang, Patrick H. Cary, F. Ren, Jihyun Kim, Marko J. Tadjer, and Michael A. Mastro. A review of Ga₂O₃ materials, processing, and devices. *Applied Physics Reviews*, 5(1):011301, 2018.
- [23] Asanka Jayawardena, Rahul P. Ramamurthy, Ayayi C. Ahyi, Dallas Morissette, and Sarit Dhar. Interface trapping in (-201) β -Ga₂O₃ MOS capacitors with deposited dielectrics. *Applied Physics Letters*, 112(19):192108, 2018.
- [24] Cree Launches Industry’s First Commercial Silicon Carbide Power MOSFET; Destined to Replace Silicon Devices in High-Voltage Power Electronics, 2011.
- [25] Masataka Higashiwaki, Kohei Sasaki, Akito Kuramata, Takekazu Masui, and Shigenobu Yamakoshi. Gallium oxide (Ga₂O₃) metal-semiconductor field-effect transistors on single-crystal β -Ga₂O₃ (010) substrates. *Applied Physics Letters*, 100(1):013504, 2012.
- [26] Caian Qiu and Rudi Metselaar. Solubility of carbon in liquid Al and stability of Al₄C₃. *Journal of Alloys and Compounds*, 216(1):55–60, 1994.
- [27] K. S. Novoselov. Electric Field Effect in Atomically Thin Carbon Films. *Science*, 306(5696):666–669, 2004.
- [28] Sumio Iijima. Helical microtubules of graphitic carbon. *Nature*, 354(6348):56–58, 1991.
- [29] Ray H Baughman, Anvar A Zakhidov, and Walt A de Heer. Carbon nanotubes—the route toward applications. *Science*, 297(5582):787–92, 2002.
- [30] K. S. Novoselov, V. I. Fal’ko, L. Colombo, P. R. Gellert, M. G. Schwab, and K. Kim. A roadmap for graphene. *Nature*, 490(7419):192–200, 2012.
- [31] Edward P. Randviir, Dale A.C. Brownson, and Craig E. Banks. A decade of graphene research: Production, applications and outlook. *Materials Today*, 17(9):426–432, 2014.

- [32] P. R. Wallace. The Band Theory of Graphite. *Physical Review*, 71(9):622–634, 1947.
- [33] Shaffique Adam, E. H. Hwang, V. M. Galitski, and S. Das Sarma. A self-consistent theory for graphene transport. *Proceedings of the National Academy of Sciences of the United States of America*, 104(47):18392–18397, 2007.
- [34] K. I. Bolotin, K. J. Sikes, Z. Jiang, M. Klima, G. Fudenberg, J. Hone, P. Kim, and H. L. Stormer. Ultrahigh electron mobility in suspended graphene. *Solid State Communications*, 146(9-10):351–355, 2008.
- [35] A. H. Castro Neto, F. Guinea, N. M.R. Peres, K. S. Novoselov, and A. K. Geim. The electronic properties of graphene. *Reviews of Modern Physics*, 81(1):109–162, 2009.
- [36] K. S. Novoselov, A. K. Geim, S. V. Morozov, D. Jiang, M. I. Katsnelson, I. V. Grigorieva, S. V. Dubonos, and A. A. Firsov. Two-dimensional gas of massless Dirac fermions in graphene. *Nature*, 438(7065):197–200, 2005.
- [37] E. H. Hwang and S. Das Sarma. Acoustic phonon scattering limited carrier mobility in two-dimensional extrinsic graphene. *Physical Review B - Condensed Matter and Materials Physics*, 77(11):1–6, 2008.
- [38] Dmitri K. Efetov and Philip Kim. Controlling electron-phonon interactions in graphene at ultrahigh carrier densities. *Physical Review Letters*, 105(25):2–5, 2010.
- [39] N. M.R. Peres, F. Guinea, and A. H. Castro Neto. Electronic properties of disordered two-dimensional carbon. *Physical Review B - Condensed Matter and Materials Physics*, 73(12):1–23, 2006.
- [40] Jianting Ye, Monica F. Craciun, Mikito Koshino, Saverio Russo, Seiji Inoue, Hongtao Yuan, Hidekazu Shimotani, Alberto F. Morpurgo, and Yoshihiro Iwasa. Accessing the transport properties of graphene and its multilayers at high carrier density. *Proceedings of the National Academy of Sciences of the United States of America*, 108(32):13002–13006, 2011.
- [41] Hongtao Liu, Yunqi Liu, and Daoben Zhu. Chemical doping of graphene. *Journal of Materials Chemistry*, 21(10):3335–3345, 2011.
- [42] G. Giovannetti, P. A. Khomyakov, G. Brocks, V. M. Karpan, J. Van Den Brink, and P. J. Kelly. Doping graphene with metal contacts. *Physical Review Letters*, 101(2):4–7, 2008.
- [43] P. A. Khomyakov, G. Giovannetti, P. C. Rusu, G. Brocks, J. Van Den Brink, and P. J. Kelly. First-principles study of the interaction and charge transfer between graphene and metals. *Physical Review B - Condensed Matter and Materials Physics*, 79(19):1–12, 2009.

- [44] Mu Cao, Ding Bang Xiong, Li Yang, Shuaishuai Li, Yiqun Xie, Qiang Guo, Zhiqiang Li, Horst Adams, Jiajun Gu, Tongxiang Fan, Xiaohui Zhang, and Di Zhang. Ultrahigh Electrical Conductivity of Graphene Embedded in Metals. *Advanced Functional Materials*, 29(17):1–8, 2019.
- [45] Mu Cao, Yongzhi Luo, Yiqun Xie, Zhanqiu Tan, Genlian Fan, Qiang Guo, Yishi Su, Zhiqiang Li, and Ding Bang Xiong. The Influence of Interface Structure on the Electrical Conductivity of Graphene Embedded in Aluminum Matrix. *Advanced Materials Interfaces*, 1900468:1–9, 2019.
- [46] C. R. Dean, A. F. Young, I. Meric, C. Lee, L. Wang, S. Sorgenfrei, K. Watanabe, T. Taniguchi, P. Kim, K. L. Shepard, and J. Hone. Boron nitride substrates for high-quality graphene electronics. *Nature Nanotechnology*, 5(10):722–726, 2010.
- [47] S. V. Morozov, K. S. Novoselov, M. I. Katsnelson, F. Schedin, D. C. Elias, J. A. Jaszczak, and A. K. Geim. Giant intrinsic carrier mobilities in graphene and its bilayer. *Physical Review Letters*, 100(1):11–14, 2008.
- [48] R. S. Shishir and D. K. Ferry. Intrinsic mobility in graphene. *Journal of Physics: Condensed Matter*, 21(23), 2009.
- [49] Jens Baringhaus, Ming Ruan, Frederik Edler, Antonio Tejada, Muriel Sicot, Amina Taleb-Ibrahimi, An Ping Li, Zhigang Jiang, Edward H. Conrad, Claire Berger, Christoph Tegenkamp, and Walt A. De Heer. Exceptional ballistic transport in epitaxial graphene nanoribbons. *Nature*, 506(7488):349–354, 2014.
- [50] R. George, K.T. Kashyap, R. Rahul, and S. Yamdagni. Strengthening in carbon nanotube/aluminium (CNT/Al) composites. *Scripta Materialia*, 53(10):1159–1163, 2005.
- [51] C. He, N. Zhao, C. Shi, X. Du, J. Li, H. Li, and Q. Cui. An Approach to Obtaining Homogeneously Dispersed Carbon Nanotubes in Al Powders for Preparing Reinforced Al-Matrix Composites. *Advanced Materials*, 19(8):1128–1132, 2007.
- [52] Jingyue Wang, Zhiqiang Li, Genlian Fan, Huanhuan Pan, Zhixin Chen, and Di Zhang. Reinforcement with graphene nanosheets in aluminum matrix composites. *Scripta Materialia*, 66(8):594–597, 2012.
- [53] Stephen F. Bartolucci, Joseph Paras, Mohammad A. Rafiee, Javad Rafiee, Sabrina Lee, Deepak Kapoor, and Nikhil Koratkar. Graphene-aluminum nanocomposites. *Materials Science and Engineering: A*, 528(27):7933–7937, 2011.
- [54] J. V. Shugart and R. C. Scherer. METAL-CARBON COMPOSITIONS, US Patent 8349759B2, 2013.

- [55] R. A. Isaacs, H. Zhu, Colin Preston, A. Mansour, M. LeMieux, P. Y. Zavalij, H. M. Iftekhar Jaim, O. Rabin, L. Hu, and L. G. Salamanca-Riba. Nanocarbon-copper thin film as transparent electrode. *Applied Physics Letters*, 106(19):193108, 2015.
- [56] H.M. Iftekhar Jaim, Romaine A. Isaacs, Sergey N. Rashkeev, Maija Kuklja, Daniel P. Cole, Melbourne C. LeMieux, Iwona Jasiuk, Sabrina Nilufar, and Lourdes G. Salamanca-Riba. Sp2 carbon embedded in Al-6061 and Al-7075 alloys in the form of crystalline graphene nanoribbons. *Carbon*, 107:56–66, 2016.
- [57] Lloyd Brown, Peter Joyce, David Forrest, and Lourdes Salamanca-Riba. Physical and Mechanical Characterization of a Nanocarbon Infused Aluminum-Matrix Composite. *Materials Performance and Characterization*, 3(1):20130023, 2014.
- [58] Rubens Roberto Ingraci Neto and Rishi Raj. The flash effect in electronic conductors: The case of amorphous carbon fibers. *Scripta Materialia*, 179:20–24, 2020.
- [59] Amelia Barreiro, Felix Börrnert, Stanislav M. Avdoshenko, Bernd Rellinghaus, Gianarelio Cuniberti, Mark H. Rummeli, and Lieven M.K. Vander-sypen. Understanding the catalyst-free transformation of amorphous carbon into graphene by current-induced annealing. *Scientific Reports*, 3:3–8, 2013.
- [60] FEI Company. *An Introduction to Electron Microscopy*. 2010.
- [61] Gatan Inc. EELS Atlas, 2019.
- [62] R F Egerton. *Electron Energy-Loss Spectroscopy in the Electron Microscope*. Springer US, Boston, MA, 3rd ed. edition, 2011.
- [63] R. F. Egerton. Radiation damage to organic and inorganic specimens in the TEM. *Micron*, 119(November 2018):72–87, 2019.
- [64] Gatan Inc. EELS Atlas, 2019.
- [65] D R McKenzie, S D Berger, and L M Brown. Bonding in a-Si(1-x)C(x): H films studied by electron energy loss near edge structure. *Solid State Communications*, 59(5):325–329, 1986.
- [66] H. Shuman and A.P. Somlyo. Electron energy loss analysis of near-trace-element concentrations of calcium. *Ultramicroscopy*, 21:23–32, 1987.
- [67] Wolfgang Härdle and Léopold Simar. *Applied Multivariate Statistical Analysis*. Springer Berlin Heidelberg, Berlin, Heidelberg, 2007.
- [68] Pierre Trebbia and Noël Bonnet. EELS elemental mapping with unconventional methods I. Theoretical basis: Image analysis with multivariate statistics and entropy concepts. *Ultramicroscopy*, 34:165–178, 1990.

- [69] N. Bonnet, E. Simova, S. Lebonvallet, and H. Kaplan. New applications of multivariate statistical analysis in spectroscopy and microscopy. *Ultramicroscopy*, 40(1):1–11, 1992.
- [70] N Bonnet, N Brun, and C Colliex. Extracting information from sequences of spatially resolved EELS spectra using multivariate statistical analysis. *Ultramicroscopy*, 77:97–112, 1999.
- [71] Pavel Potapov. Why Principal Component Analysis of STEM spectrum-images results in “abstract”, uninterpretable loadings? *Ultramicroscopy*, 160:197–212, 2016.
- [72] Joshua A. Taillon. *Applications of Advanced Analytical Microscopy at the Nanoscale: Wide Bandgap and Solid Oxide Fuel Cell Materials*. Phd, University of Maryland, 2016.
- [73] Daniel D Lee and H Sebastian Seung. Learning the parts of objects by non-negative matrix factorization. *Nature*, 401:788–791, 1999.
- [74] Nadi Braidy and Ryan Gosselin. Unmixing noisy co-registered spectrum images of multicomponent nanostructures. *Scientific Reports*, 9(18797):1–8, 2019.
- [75] Francisco de la Peña, Tomas Ostasevicius, Vidar Tonaas Fauske, Pierre Burdet, Petras Jokubauskas, Magnus Nord, Mike Sarahan, Duncan N Johnstone, Eric Prestat, Joshua Taillon, Jan Caron, Tom Furnival, Katherine E MacArthur, Alberto Eljarrat, Stefano Mazzucco, Vadim Migunov, Thomas Aarholt, Michael Walls, Florian Winkler, Ben Martineau, Gaël Donval, Eric R Hoglund, Luiz Fernando Zagonel, Andreas Garmannslund, Christoph Gohlke, Iygr, and Huang-Wei Chang. hyperspy/hyperspy v1.2, 2017.
- [76] Nan Yao, editor. *Focused Ion Beam Systems*. Cambridge University Press, Cambridge, 2007.
- [77] J. P. McCaffrey, M. W. Phaneuf, and L. D. Madsen. Surface damage formation during ion-beam thinning of samples for transmission electron microscopy. *Ultramicroscopy*, 87(3):97–104, 2001.
- [78] University of Cambridge. Raman Spectroscopy, 2018.
- [79] F. Tuinstra and L. Koenig. Raman Spectrum of Graphite. *The Journal of Chemical Physics*, 53(1970):1126–1130, 1970.
- [80] L. M. Malard, M. A. Pimenta, G. Dresselhaus, and M. S. Dresselhaus. Raman spectroscopy in graphene. *Physics Reports*, 473(5-6):51–87, 2009.
- [81] A. Ferrari and J. Robertson. Interpretation of Raman spectra of disordered and amorphous carbon. *Physical Review B*, 61(20):14095–14107, 2000.

- [82] Tom O’Haver. *A Pragmatic Introduction to Signal Processing*, 2018.
- [83] A. C. Ferrari, J. C. Meyer, V. Scardaci, C. Casiraghi, M. Lazzeri, F. Mauri, S. Piscanec, D. Jiang, K. S. Novoselov, S. Roth, and A. K. Geim. Raman spectrum of graphene and graphene layers. *Physical Review Letters*, 97(18):1–4, 2006.
- [84] L. G. Cançado, K. Takai, T. Enoki, M. Endo, Y. A. Kim, H. Mizusaki, A. Jorio, L. N. Coelho, R. Magalhães-Paniago, and M. A. Pimenta. General equation for the determination of the crystallite size l_a of nanographite by Raman spectroscopy. *Applied Physics Letters*, 88(16):12–14, 2006.
- [85] M.A. Pimenta, G. Dresselhaus, M.S. Dresselhaus, L.G. Cançado, Ado Jorio, and R. Saito. Studying disorder in graphite-based systems by Raman spectroscopy. *Physical Chemistry Chemical Physics*, 9(11):1276–1291, 2007.
- [86] Tuck C. Choy. *Effective Medium Theory: Principles and Applications*. Oxford University Press, Oxford, 1999.
- [87] Goran Grimvall. *Thermophysical Properties of Materials*. Elsevier Science Publishers B. V., Amsterdam, 1986.
- [88] Muhammad Usama Siddiqui and Abul Fazal M. Arif. Generalized effective medium theory for particulate nanocomposite materials. *Materials*, 9(8), 2016.
- [89] Ce-wen Nan, R Birringer, David R Clarke, and H Gleiter. Effective thermal conductivity of particulate composites with interfacial thermal resistance. *Journal of Applied Physics*, 81(10):6692–6699, 1997.
- [90] Fei Deng, Quan Shui Zheng, Li Feng Wang, and Ce Wen Nan. Effects of anisotropy, aspect ratio, and nonstraightness of carbon nanotubes on thermal conductivity of carbon nanotube composites. *Applied Physics Letters*, 90(2), 2007.
- [91] Fei Deng and Quan Shui Zheng. An analytical model of effective electrical conductivity of carbon nanotube composites. *Applied Physics Letters*, 92(7):90–93, 2008.
- [92] Rolf Landauer. The Electrical Resistance of Binary Metallic Mixtures. *Journal of Applied Physics*, 23(7):779–784, 1952.
- [93] Joshua A. Taillon, Joon Hyuk Yang, Claude A. Ahyi, John Rozen, John R. Williams, Leonard C. Feldman, Tsvetanka S. Zheleva, Aivars J. Lelis, and Lourdes G. Salamanca-Riba. Systematic structural and chemical characterization of the transition layer at the interface of NO-annealed 4H-SiC/SiO₂ metal-oxide-semiconductor field-effect transistors. *Journal of Applied Physics*, 113(4), 2013.

- [94] Dai Okamoto, Hiroshi Yano, Kenji Hirata, Tomoaki Hatayama, and Takashi Fuyuki. Improved inversion channel mobility in 4H-SiC MOSFETs on Si face utilizing phosphorus-doped gate oxide. *IEEE Electron Device Letters*, 31(7):710–712, 2010.
- [95] Asanka Jayawardena, X Shen, P M Mooney, and Sarit Dhar. Mechanism of phosphorus passivation of near-interface oxide traps in 4H SiC MOS devices investigated by CCDLTS and DFT calculation. *Semiconductor Science and Technology*, 33(065005), 2018.
- [96] Victor Soler, Maria Cabello, José Millán, and Philippe Godignon. 4.5 kV SiC MOSFET with Boron Doped Gate Dielectric. *International Symposium on Power Semiconductor Devices and ICs (ISPSD)*, pages 283–286, 2016.
- [97] M. Cabello, V. Soler, J. Montserrat, J. Rebollo, J. M. Rafí, and P. Godignon. Impact of boron diffusion on oxynitrided gate oxides in 4H-SiC metal-oxide-semiconductor field-effect transistors. *Applied Physics Letters*, 111(4):042104, 2017.
- [98] Dai Okamoto, Mitsuru Sometani, Shinsuke Harada, Ryoji Kosugi, Yoshiyuki Yonezawa, and Hiroshi Yano. Effect of boron incorporation on slow interface traps in SiO₂/4H-SiC structures. *Applied Physics A*, 123(2):133, 2017.
- [99] Joshua A. Taillon, Christopher J. Klingshirn, Chunkun Jiao, Yongju Zheng, Sarit Dhar, Tsvetanka S. Zheleva, Aivars J. Lelis, and Lourdes G. Salamanca-Riba. Analysis of the electronic and chemical structure in boron and phosphorus passivated 4H -SiC/SiO₂ interfaces using HRTEM and STEM-EELS. *Applied Physics Letters*, 113(19), 2018.
- [100] Werner Kern. Evolution of silicon wafer cleaning technology. *Proceedings - The Electrochemical Society*, 90(9):3–19, 1990.
- [101] H Sauer, Rik Brydson, P N Rowley, W Engel, and J M Thomas. Determination of coordinations and coordination-specific site occupancies by electron energy-loss spectroscopy: An investigation of boron-oxygen compounds. *Ultramicroscopy*, 49:198–209, 1993.
- [102] G. Yang, G. Möbus, and R. J. Hand. Cerium and boron chemistry in doped borosilicate glasses examined by EELS. *Micron*, 37(5):433–441, 2006.
- [103] R Arenal, F de la Peña, O Stéphan, M Walls, M Tencé, a Loiseau, and C Colliex. Extending the analysis of {EELS} spectrum-imaging data, from elemental to bond mapping in complex nanostructures. *Ultramicroscopy*, 109(1):32–38, 2008.
- [104] R A Smith. Boron in glass and glass making. *Journal of Non-Crystalline Solids*, 84(1-3):421–432, 1986.

- [105] P. M. Mooney, Zenan Jiang, A. F. Basile, Yongju Zheng, and Sarit Dhar. Effects of antimony (Sb) on electron trapping near SiO₂/4H-SiC interfaces. *Journal of Applied Physics*, 120(3), 2016.
- [106] Tamura Corporation, Semiconductor Promotion Department, Hirose-dai, Sayama-shi, Saitama, 350-1328 Japan.
- [107] Chuanjin Huang, Wenxiang Mu, Hai Zhou, Yongwei Zhu, Xiaoming Xu, Zhitai Jia, Lei Zheng, and Xutang Tao. Effect of OH on chemical mechanical polishing of beta-Ga₂O₃ (100) substrate using an alkaline slurry. *RSC Advances*, 8(12):6544–6550, 2018.
- [108] Shun Ito, Kenichiro Takeda, Kengo Nagata, Hiroki Aoshima, Kosuke Takehara, Motoaki Iwaya, Tetsuya Takeuchi, Satoshi Kamiyama, Isamu Akasaki, and Hiroshi Amano. Growth of GaN and AlGaN on (100) β -Ga₂O₃ substrates. *Physica Status Solidi (C) Current Topics in Solid State Physics*, 9(3-4):519–522, 2012.
- [109] A. H. Carim and Anjan Bhattacharyya. Si/SiO₂ interface roughness: Structural observations and electrical consequences. *Applied Physics Letters*, 46(9):872–874, 1985.
- [110] M Houssa, T Nigam, P.W Mertens, and M.M Heyns. Effect of extreme surface roughness on the electrical characteristics of ultra-thin gate oxides. *Solid-State Electronics*, 43(1):159–167, 1999.
- [111] Junji Senzaki, Kazutoshi Kojima, and Kenji Fukuda. Effects of n-type 4H-SiC epitaxial wafer quality on reliability of thermal oxides. *Applied Physics Letters*, 85(25):6182–6184, 2004.
- [112] Takafumi Kamimura, Daivasigamani Krishnamurthy, Akito Kuramata, Shigenobu Yamakoshi, and Masataka Higashiwaki. Epitaxially grown crystalline Al₂O₃ interlayer on β -Ga₂O₃ (010) and its suppressed interface state density. *Japanese Journal of Applied Physics*, 55(12):1202B5, 2016.
- [113] S. Fung, Xu Xiaoliang, Zhao Youwen, Sun Wenhong, Chen Xudong, Sun Niefung, Sun Tongnian, and Jiang Chunxiang. Gallium/aluminum interdiffusion between n-GaN and sapphire. *Journal of Applied Physics*, 84(4):2355, 1998.
- [114] Anshu Goyal, Brajesh S. Yadav, O. P. Thakur, A. K. Kapoor, and R. Muralidharan. Effect of annealing on β -Ga₂O₃ film grown by pulsed laser deposition technique. *Journal of Alloys and Compounds*, 583:214–219, 2014.
- [115] K. A. Unocic, M. J. Mills, and G. S. Daehn. Effect of gallium focused ion beam milling on preparation of aluminium thin foils. *Journal of Microscopy*, 240(3):227–238, 2010.

- [116] Fabi Zhang, Katsuhiko Saito, Tooru Tanaka, Mitsuhiro Nishio, Makoto Arita, and Qixin Guo. Wide bandgap engineering of (AlGa)₂O₃ films. *Applied Physics Letters*, 105(16):162107, 2014.
- [117] Xiaofan Ma, Yuming Zhang, Linpeng Dong, and Renxu Jia. First-principles calculations of electronic and optical properties of aluminum-doped β -Ga₂O₃ with intrinsic defects. *Results in Physics*, 7:1582–1589, 2017.
- [118] Junsung Park and Sung Min Hong. First principles calculation of band offsets and defect energy levels in Al₂O₃/ β -Ga₂O₃ interface structures with point defects. *Journal of Semiconductor Technology and Science*, 19(4):413–425, 2019.
- [119] Hong Zhou, Sami Alghamdi, Mengwei Si, Gang Qiu, and Peide D. Ye. Al₂O₃/ β -Ga₂O₃(-201) Interface Improvement Through Piranha Pretreatment and Post-deposition Annealing. *IEEE Electron Device Letters*, 37(11):1411–1414, 2016.
- [120] R. Nakamura, M. Ishimaru, H. Yasuda, and H. Nakajima. Atomic rearrangements in amorphous Al₂O₃ under electron-beam irradiation. *Journal of Applied Physics*, 113(6), 2013.
- [121] Jack Murray, Kai Song, Wayne Huebner, and Matthew O’Keefe. Electron beam induced crystallization of sputter deposited amorphous alumina thin films. *Materials Letters*, 74:12–15, 2012.
- [122] R. F. Egerton, P. Li, and M. Malac. Radiation damage in the TEM and SEM. *Micron*, 35(6):399–409, 2004.
- [123] R. F. Egerton. Control of radiation damage in the TEM. *Ultramicroscopy*, 127:100–108, 2013.
- [124] Yi-Yu Wang, Hua-Jun Shen, Yun Bai, Yi-Dan Tang, Ke-An Liu, Cheng-Zhan Li, and Xin-Yu Liu. Influences of high-temperature annealing on atomic layer deposited Al₂O₃/4H-SiC. *Chinese Physics B*, 22(7):078102, jul 2013.
- [125] Martin Rudolph, Mykhaylo Motylenko, and David Rafaja. Structure model of γ -Al₂O₃ based on planar defects. *IUCrJ*, 6:116–127, 2019.
- [126] Igor Levin and David Brandon. Metastable Alumina Polymorphs: Crystal Structures and Transition Sequences. *Journal of the American Ceramic Society*, 81(8):1995–2012, 2005.
- [127] J Ahman, G Svensson, and J Albertsson. A reinvestigation of beta-gallium oxide. *Acta Crystallographica, Section C: Crystal Structure Communications*, 52:1336–1338, 1996.
- [128] Anubhav Jain, Shyue Ping Ong, Geoffroy Hautier, Wei Chen, William Davidson Richards, Stephen Dacek, Shreyas Cholia, Dan Gunter, David Skinner, Gerbrand Ceder, and Kristin a. Persson. Commentary: The Materials Project:

A materials genome approach to accelerating materials innovation. *APL Materials*, 1(1):011002, jul 2013.

- [129] Mai Hattori, Takayoshi Oshima, Ryo Wakabayashi, Kohei Yoshimatsu, Kohei Sasaki, Takekazu Masui, Akito Kuramata, Shigenobu Yamakoshi, Koji Horiba, Hiroshi Kumigashira, and Akira Ohtomo. Epitaxial growth and electric properties of γ -Al₂O₃ (110) films on β -Ga₂O₃ (010) substrates. *Japanese Journal of Applied Physics*, 55(12):1202B6, 2016.
- [130] C. Århammar, Annette Pietzsch, Nicolas Bock, Erik Holmström, C. Moyses Araujo, Johan Gråsjö, Shuxi Zhao, Sara Green, T. Peery, Franz Hennies, Shahrads Amerioun, Alexander Föhlisch, Justine Schlappa, Thorsten Schmitt, Vladimir N. Strocov, Gunnar A. Niklasson, Duane C. Wallace, Jan Erik Rubensson, Börje Johansson, and Rajeev Ahuja. Unveiling the complex electronic structure of amorphous metal oxides. *Proceedings of the National Academy of Sciences of the United States of America*, 108(16):6355–6360, 2011.
- [131] M. D. Groner, F. H. Fabreguette, J. W. Elam, and S. M. George. Low-Temperature Al₂O₃ Atomic Layer Deposition. *Chemistry of Materials*, 16(4):639–645, 2004.
- [132] Masafumi Hirose, Toshihide Nabatame, Kazuya Yuge, Erika Maeda, Akihiko Ohi, Naoki Ikeda, Yoshihiro Irokawa, Hideo Iwai, Hideyuki Yasufuku, Satoshi Kawada, Makoto Takahashi, Kazuhiro Ito, Yasuo Koide, and Hajime Kiyono. Influence of post-deposition annealing on characteristics of Pt/Al₂O₃/ β -Ga₂O₃ MOS capacitors. *Microelectronic Engineering*, 216(April):111040, 2019.
- [133] Man Hoi Wong, Akinori Takeyama, Takahiro Makino, Takeshi Ohshima, Kohei Sasaki, Akito Kuramata, Shigenobu Yamakoshi, and Masataka Higashiwaki. Radiation hardness of β -Ga₂O₃ metal-oxide-semiconductor field-effect transistors against gamma-ray irradiation. *Applied Physics Letters*, 112(2), 2018.
- [134] Xiaoxiao Ge. *Fabrication and Characterization of Aluminum Nano-Carbon Composites and Investigation of Their Electrical Conductivity*. PhD thesis, University of Maryland, 2020.
- [135] R. R. Nair, P. Blake, A. N. Grigorenko, K. S. Novoselov, T. J. Booth, T. Stauber, N. M.R. Peres, and A. K. Geim. Fine structure constant defines visual transparency of graphene. *Science*, 320(5881):1308, 2008.
- [136] D. Graf, F. Molitor, K. Ensslin, C. Stampfer, A. Jungen, C. Hierold, and L. Wirtz. Spatially resolved raman spectroscopy of single- and few-layer graphene. *Nano Letters*, 7(2):238–242, 2007.

- [137] Duhee Yoon, Hyerim Moon, Hyeonsik Cheong, Jin Sik Choi, Jung Ae Choi, and Bae Ho Park. Variations in the Raman spectrum as a function of the number of graphene layers. *Journal of the Korean Physical Society*, 55(3):1299–1303, 2009.
- [138] Aleksandar D. Rakić, Aleksandra B. Djurišić, Jovan M. Elazar, and Marian L. Majewski. Optical properties of metallic films for vertical-cavity optoelectronic devices. *Applied Optics*, 37(22):5271, 1998.
- [139] Weilie Zhou, Robert Apkarian, Zhong Lin Wang, and David Joy. *Fundamentals of Scanning Electron Microscopy (SEM)*, chapter 3, pages 76–100. Springer New York, New York, NY, 2007.
- [140] X Ge, C Klingshirn, M Morales, M Wuttig, O Rabin, S Zhang, and L.G. Salamanca-Riba. Electrical and structural characterization of nano-carbonaluminum composites fabricated by electro-charging-assisted process. *Carbon*, 173:115–125, 2021.
- [141] The Aluminium Association. International Alloy Designations and Chemical Composition Limits for Wrought Aluminum and Wrought Aluminum Alloys. Technical Report Enero 2015, 2015.
- [142] Xinyi Zhang, Reinhard Schneider, Erich Müller, and Dagmar Gerthsen. Practical aspects of the quantification of sp²-hybridized carbon atoms in diamond-like carbon by electron energy loss spectroscopy. *Carbon*, 102:198–207, 2016.
- [143] R F Egerton. Electron energy-loss spectroscopy in the TEM. *Reports on Progress in Physics*, 72:16502, 2009.
- [144] Jiayi Zhang, Mingyang Ma, Fanghua Shen, Danqing Yi, and Bin Wang. Influence of deformation and annealing on electrical conductivity, mechanical properties and texture of Al-Mg-Si alloy cables. *Materials Science and Engineering A*, 710(August 2017):27–37, 2018.
- [145] Christopher M. Shumeyko, Xiaoxiao Ge, Christopher J. Klingshirn, Lourdes Salamanca-Riba, and Daniel P. Cole. Tunable mechanical behavior of graphene nanoribbon-metal composites fabricated through an electrocharge-assisted process. *Materials Science and Engineering: A*, 800:140289, 2021.
- [146] M.J Hordon and B.L Averbach. X-ray measurements of dislocation density in deformed Copper and Aluminum single crystals. *Acta Metallurgica*, 9(3):237–246, 1961.
- [147] Mete Bakir and Iwona Jasiuk. Novel metal-carbon nanomaterials: A review on covetics. *Advanced Materials Letters*, 8(9):884–890, 2017.
- [148] A. Reuss. Berechnung der Fließgrenze von Mischkristallen auf Grund der Plastizitätsbedingung für Einkristalle. *ZAMM - Zeitschrift für Angewandte Mathematik und Mechanik*, 9(1):49–58, 1929.

- [149] W. Voigt. Ueber die Beziehung zwischen den beiden Elasticitätsconstanten isotroper Körper. *Annalen der Physik*, 274(12):573–587, 1889.
- [150] O. Hjortstam, P. Isberg, S. Söderholm, and H. Dai. Can we achieve ultra-low resistivity in carbon nanotube-based metal composites? *Applied Physics A: Materials Science and Processing*, 78(8):1175–1179, 2004.
- [151] E. J. Garboczi, K. A. Snyder, J F Douglas, and M. F. Thorpe. Geometrical percolation threshold of overlapping ellipsoids. *Physical Review E*, 52(1):819–828, 1995.
- [152] C. W. Nan, Z. Shi, and Y. Lin. A simple model for thermal conductivity of carbon nanotube-based composites. *Chemical Physics Letters*, 375(5-6):666–669, 2003.
- [153] M. J. Biercuk, M. C. Llaguno, M. Radosavljevic, J. K. Hyun, A. T. Johnson, and J. E. Fischer. Carbon nanotube composites for thermal management. *Applied Physics Letters*, 80(15):2767–2769, 2002.
- [154] Zhidong Han and Alberto Fina. Thermal conductivity of carbon nanotubes and their polymer nanocomposites: A review. *Progress in Polymer Science (Oxford)*, 36(7):914–944, 2011.
- [155] Lloyd Brown, Peter Joyce, David Forrest, and Jennifer Wolk. Physical and mechanical characterization of a nano carbon infused aluminum-matrix composite. *International SAMPE Technical Conference*, 2011.
- [156] X. Ge, C. Klingshirn, M. Wuttig, K. Gaskell, P. Y. Zavalij, Y. Liang, C. M. Shumeyko, D. P. Cole, and L. G. Salamanca-Riba. Mechanism studies and fabrication for the incorporation of carbon into Al alloys by the electro-charging assisted process. *Carbon*, 149:203–212, 2019.
- [157] Rajatendu Sengupta, Mithun Bhattacharya, S. Bandyopadhyay, and Anil K. Bhowmick. A review on the mechanical and electrical properties of graphite and modified graphite reinforced polymer composites. *Progress in Polymer Science (Oxford)*, 36(5):638–670, 2011.
- [158] W. Primak. C-axis electrical conductivity of graphite. *Physical Review*, 103(3):544–546, 1956.
- [159] Zhiyong Wei, Juekuan Yang, Weiyu Chen, Kedong Bi, Deyu Li, and Yunfei Chen. Phonon mean free path of graphite along the c -axis. *Applied Physics Letters*, 104(8), 2014.
- [160] C. Berger, Zhimin Song, Xuebin Li, Xiaosong Wu, Nate Brown, Cecile Naud, Didier Mayou, Tianbo Li, Joanna Hass, Alexei N. Marchenkov, Edward H. Conrad, Phillip N. First, and Walt A. de Heer. Electronic Confinement and Coherence in Patterned Epitaxial Graphene. *Science*, 312(5777):1191–1196, 2006.

- [161] Cheng Gong, Geunsik Lee, Bin Shan, Eric M. Vogel, Robert M. Wallace, and Kyeongjae Cho. First-principles study of metal-graphene interfaces. *Journal of Applied Physics*, 108(12), 2010.
- [162] G. Kresse and J. Furthmüller. Efficient iterative schemes for ab initio total-energy calculations using a plane-wave basis set. *Physical Review B*, 54(16):11169–11186, 1996.
- [163] G. Kresse and D. Joubert. From ultrasoft pseudopotentials to the projector augmented-wave method. *Physical Review B*, 59(3):1758–1775, 1999.
- [164] Georg K H Madsen, Jesús Carrete, and Matthieu J Verstraete. BoltzTraP2, a program for interpolating band structures and calculating semi-classical transport coefficients. *Computer Physics Communications*, 231:140–145, 2018.
- [165] Azad Naeemi and James D. Meindl. Conductance modeling for graphene nanoribbon (GNR) interconnects. *IEEE Electron Device Letters*, 28(5):428–431, 2007.
- [166] Katsunori Wakabayashi, Ken Ichi Sasaki, Takeshi Nakanishi, and Toshiaki Enoki. Electronic states of graphene nanoribbons and analytical solutions. *Science and Technology of Advanced Materials*, 11(5), 2010.
- [167] Luca Banszerus, Michael Schmitz, Stephan Engels, Matthias Goldsche, Kenji Watanabe, Takashi Taniguchi, Bernd Beschoten, and Christoph Stampfer. Ballistic Transport Exceeding 28 μm in CVD Grown Graphene. *Nano Letters*, 16(2):1387–1391, 2016.
- [168] Chi Fan Chen, Cheol Hwan Park, Bryan W. Boudouris, Jason Horng, Baisong Geng, Caglar Girit, Alex Zettl, Michael F. Crommie, Rachel A. Segalman, Steven G. Louie, and Feng Wang. Controlling inelastic light scattering quantum pathways in graphene. *Nature*, 471(7340):617–620, 2011.
- [169] P. A. Khomyakov, A. A. Starikov, G. Brocks, and P. J. Kelly. Nonlinear screening of charges induced in graphene by metal contacts. *Physical Review B - Condensed Matter and Materials Physics*, 82(11):1–6, 2010.
- [170] I. Deretzis, G. Fiori, G. Iannaccone, and A. La Magna. Atomistic quantum transport modeling of metal-graphene nanoribbon heterojunctions. *Physical Review B - Condensed Matter and Materials Physics*, 82(16):3–6, 2010.
- [171] Seung Min Song and Byung Jin Cho. Contact resistance in graphene channel transistors. *Carbon letters*, 14(3):162–170, 2013.
- [172] Xiang Ji, Jinyu Zhang, Yan Wang, He Qian, and Zhiping Yu. A theoretical model for metal-graphene contact resistance using a DFT-NEGF method. *Physical Chemistry Chemical Physics*, 15(41):17883–17886, 2013.

- [173] David J. Griffiths. *Introduction to Quantum Mechanics*. Pearson Education, Inc., Upper Saddle River, NJ, USA, 2 edition, 2005.
- [174] Seyoung Kim, Junghyo Nah, Insun Jo, Davood Shahrjerdi, Luigi Colombo, Zhen Yao, Emanuel Tutuc, and Sanjay K. Banerjee. Realization of a high mobility dual-gated graphene field-effect transistor with Al₂O₃ dielectric. *Applied Physics Letters*, 94(6):2007–2010, 2009.
- [175] Young Gon Lee, Yun Ji Kim, Chang Goo Kang, Chunhum Cho, Sangchul Lee, Hyeon Jun Hwang, Ukjin Jung, and Byoung Hun Lee. Influence of extrinsic factors on accuracy of mobility extraction in graphene metal-oxide-semiconductor field effect transistors. *Applied Physics Letters*, 102(9):1–5, 2013.
- [176] Y. Pan, G. J. Weng, S. A. Meguid, W. S. Bao, Z. H. Zhu, and A. M.S. Hamouda. Percolation threshold and electrical conductivity of a two-phase composite containing randomly oriented ellipsoidal inclusions. *Journal of Applied Physics*, 110(12), 2011.
- [177] Geoffrey H Campbell, Joseph T. McKeown, and Melissa K Santala. High-Speed Electron Microscopy. In P. W. Hawkes and J. C. H. Spence, editors, *Springer Handbook of Microscopy*, chapter 8, pages 455–486. Springer Nature Switzerland AG, 2019.
- [178] S. W. Ip, R. Sridhar, J. M. Toguri, T. F. Stephenson, and A. E.M. Warner. Wettability of nickel coated graphite by aluminum. *Materials Science and Engineering A*, 244(1):31–38, 1998.
- [179] Yu Huang, Qiubao Ouyang, Di Zhang, Jing Zhu, Ruixiang Li, and Hong Yu. Carbon Materials Reinforced Aluminum Composites: A Review. *Acta Metallurgica Sinica (English Letters)*, 27(5):775–786, 2014.
- [180] David R.G. Mitchell and Mitchell J.B. Nancarrow. Probe current determination in analytical TEM/STEM and its application to the characterization of large area EDS detectors. *Microscopy Research and Technique*, 78(10):886–893, 2015.
- [181] JEOL Ltd. JEM-2100 Electron Microscope Manual. Technical report, Tokyo, 2004.
- [182] Christopher J. Klingshirn, Asanka Jayawardena, Sarit Dhar, Rahul P. Ramamurthy, Dallas Morissette, Zoey Warecki, John Cumings, Tsvetanka Zheleva, Aivars Lelis, and Lourdes G. Salamanca-Riba. Electron beam-induced crystallization of Al₂O₃ gate layer on β -Ga₂O₃ MOS capacitors. *Micron*, page 102954, 2020.